COUPLED SUPERCONDUCTING MICROWAVE RESONATORS FOR STUDIES OF ELECTRO-MECHANICAL INTERACTION

by

Bindu Malini Gunupudi

A thesis submitted to
The University of Birmingham
for the degree of
DOCTOR OF PHILOSOPHY

Condensed Matter Group
School of Physics and Astronomy
College of Engineering and Physical Sciences
The University of Birmingham

January 2015

Abstract

The motivation behind the work described in this thesis is to study the coupling between a mechanical resonator (nanobar) and a pair of almost identical, coupled, microwave resonators, where the splitting frequency at their avoided crossing is close to the nanomechanical resonant frequency.

The first part of the project is the study of the splitting frequency as a function of the coupling between the microwave resonators. This has been thoroughly investigated by theoretical simulations in COMSOL and AIM Spice, and experimentally verified by low temperature measurements on thin film superconducting microwave resonators. Deviations of the measured splitting from the theoretical values, and reflection measurements on the samples, showed that the resonators required to be tuned in order to reach the avoided crossing.

A novel tuning mechanism that was mechanically controlled was devised and implemented in-situ in the low temperature experiments. Tuning of resonators was successfully achieved on two samples and there was excellent agreement of the measured splitting with the values predicted in AIM Spice. A wide frequency tuning range of 50 MHz was obtained, more than the required range for our experiments, without degrading the high quality factors ($\approx 10^5$) of the resonators. This enabled the measurement of the inherent splitting of the coupled resonator frequencies at the avoided crossing, and more importantly, paves the way for studies of electro-mechanical interaction.

In the absence of nanobars, an analogous experiment that varied the resonator inductance instead of its capacitance was devised. The expected output response was analysed in MATLAB for both small and large amplitude drive levels. The resonant frequency of one of the resonators was perturbed using a small amplitude magnetic field using a coil placed underneath the sample, a case that has not been previously explored. The results obtained from these preliminary experiments have shown a good agreement with the theoretical predictions.

Dedicated to my ever-loving Mother, Father, and Sister

ACKNOWLEDGEMENTS

I would like to thank my supervisors Mark Colclough and Chris Muirhead for all the guidance and support I have received during the course of my PhD. I thank them for proof-reading this manuscript and giving valuable suggestions at every stage, all of which, enabled me to deliver to the best of my capability. During the past four years, I had the opportunity to observe and learn from Mark's skillful methods of carrying out any kind of experiment, which has been a great source of motivation. I would like to thank Chris who has been an epitome of patience whilst dealing with all my questions, tutoring me on several theoretical aspects of this project, and his tireless efforts to re-program my brain!

A special mention goes to our lab technicians, Gary, who has diligently machined some of the key apparatus required to carry out this project, and Michael, for his constant supply of liquid nitrogen and helium.

I would like to thank all the members of the Condensed Matter group for making it a pleasant place to work. I enjoyed the company of all my colleagues, past and present: Georgina Klemencic, Josh Lim, Alistair Cameron, Louis Lemberger, Lingjia Shen, and Randeep Riyat.

I would also like to thank other friends in Birmingham for always being there and for having given me wonderful weekend breaks. My stay in this country has been made enjoyable by many friends across the country who at all times, had their doors open and made me feel like I had a home away from home. Many thanks to Bharathi di, Raj and Kripa in Derby: I had a fabulous time during every Easter, and needless to mention, several of my weekends were spent there, after which I always felt rejuvenated and optimistic. I would also like to thank my friends in Eastbourne, Vidyu akka, Mahesh anna, and Nuleen for all the encouragement they have given me over the last four years and not to forget, their warmth and affection, especially during the cold Christmas breaks!

Many thanks to my teachers back home, who have been a source of inspiration, and encouraged me right from my school days. A special mention goes to my uncle Prof.Kameswararao Gunupudi whose passion for physics is inspiring and aunt Padma for her motivating words. I would like to thank my friends who studied with me in school and universities back in India for being available at all times for a light-hearted

conversation.

Last, but not the least, I would like to thank immensely my family members for being pillars of moral support and encouragement: I would like to thank my younger sister who always brings a smile on my face with her delightful banter, my grandparents for their continued support, my aunt Padma, and uncle Radhakrishna for their help in beginning my journey to this country. I have no words to express my heartfelt gratitude to my Parents for their incredible efforts and sacrifices to provide me with the best education possible, for constantly boosting my spirits, and for patiently dealing with me during the write-up phase. This work would not have been completed without their gentle, reassuring and kind gestures.

CONTENTS

LIST OF FIGURES

LIST OF TABLES

CHAPTER 1

INTRODUCTION

The aim of the work described in this thesis is to experimentally study and manipulate a system of coupled, nearly identical, superconducting microwave resonators. This would ultimately be beneficial to experiments based on investigating the interaction between a mechanical resonator (nanobar) and superconducting microwave resonators. Extensive reports in the literature have involved the coupling of a mechanical resonator to a single microwave resonator. Where the motivation behind this work differs from any previously reported is that it involves the coupling of a nanobar to a system of *coupled* microwave resonators, where the microwave field can be coupled to the square of the nanobar displacement. Experiments in this field are currently of considerable interest as they provide prospects for exploring the quantum properties of macroscopic mechanical oscillators.

Prior to the investigation of microwave-nanomechanical coupling, experiments were conducted by various research groups to study the interaction of light in optical cavities with movable mirrors. A motivation behind experiments performed in this field is the need to understand and minimize noise contributions in applications such as in gravity wave detectors, and also in the fundamental study of interaction between optical photons and vibrational modes, particularly in the quantum limit where the mirror is excited with amplitudes close to the zero point motion. The main problem with using optical cavities to achieve the quantum limit is that these systems are large and have low vibrational frequencies. This means that they need to be cooled well below milli-Kelvin temperatures to access zero point motion, so that $k_B T \ll \hbar\omega_{mech}$. For example, a 1 MHz mechanical resonator needs to be cooled to a temperature of ≈ 50 μK in order to observe its zero point motion, which is hard to achieve in an object with dimensions of an optical cavity.

In recent years, there has been an increasing interest in on-chip microwave systems using sub micron nanobars which have vibrational frequencies in the range $10 - 100$ MHz and corresponding zero point temperatures of $0.6 - 6$ mK. These resonators map very closely the physics of optical systems. Also, they can be easily fabricated using well established lithographic methods and cooled by cryogenic techniques. Although measuring the zero point motion requires temperatures below the range of most dilution refrigerators (~ 20 mK), they can be further cooled by the lower sideband cooling methods. Much progress has been made in this field and, within the last four years, clear evidence of cooling a mechanical resonator to its zero point energy has been demonstrated by coupling it to a superconducting microwave resonator [3]. The goal of this project is not to achieve zero point motion, but the progress in this field is briefly reviewed because it guides the design parameters and experimental techniques to be used in this project.

1.1 Optical resonators

An optical resonator system is used to describe some of the basic physics related to our experiment as it is easier to visualize. Consider a Fabry-Perot cavity in which one of the mirrors is movable. In this case, there is a two-way interaction between light and the moving mirror : a) the cavity length changes due to the displacement of the mirror and hence there is a change in the cavity resonance frequency. b) The photons in the cavity exert a radiation pressure force on the mirror and the motion of the mirror in turn affects the photon density within the cavity. Depending on the detuning of laser light within the cavity, the mirror motion can be damped or amplified.

At temperatures well above the zero point temperature of the mirror, its motion can be considered classically as that of a damped harmonic oscillator which is driven mainly by the radiation pressure (light) force within the cavity [1,13]. Its equation of motion can then be written as:

$$m\ddot{x} + m\gamma\dot{x} + kx = F, \tag{1.1}$$

where m is the mass of the movable mirror, x is its displacement, γ and k are the damping and restoring force coefficients.

Let ω_{laser} and ω_{cavity} be the optical drive and cavity resonant frequencies respectively, and let the periodic displacement of the movable mirror be of the form $x = x_0 cos(\omega_m t)$, where ω_m is the frequency of its displacement. The light force on the mirror can have components that are in and out-of-phase with its motion. The in-phase component adds to the restoring force and causes a change in ω_m. The out-of-phase component contributes to the damping force on the mirror and this could be either positive or negative, which results in either cooling or heating of the mirror. If $\omega_{laser} < \omega_{cavity}$, for a periodic displacement of the

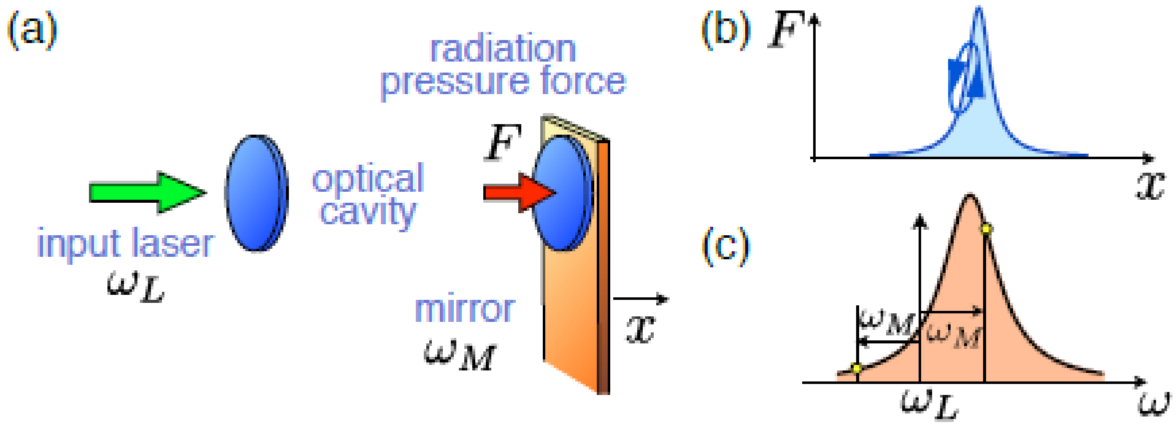

Figure 1.1: (a) A schematic of an optical cavity to study the interaction of light with mechanical vibrations. (b) The radiation pressure force as a function of the mirror position. This enables the understanding of the system in the classical limit. (c) In the quantum limit, the interaction is explained in terms of the sidebands at $\omega_{laser} \pm \omega_m$. This figure is taken from [1].

mirror as shown in fig. 1.1b, work is done *on* the light force by the movable mirror, i.e., $\oint F.dx < 0$, which results in cooling of the mirror. If on the other hand, $\omega_{laser} > \omega_{cavity}$, work is done *by* the light force on the mirror, i.e., $\oint F.dx > 0$, which causes heating of the mirror. In the good cavity limit where the bandwidth of the optical resonance $< 2\omega_m$, the cooling of the mirror is maximized when $\omega_{laser} = (\omega_{cavity} - \omega_m)$ and heating is maximized when $\omega_{laser} = (\omega_{cavity} + \omega_m)$.

In the quantum limit, excitation of the cavity with $\omega_{laser} = (\omega_{cavity} - \omega_m)$ results in a phonon of frequency ω_m being removed from the mirror and added to the laser photon of frequency $h\omega_{laser}$ so that the cavity can be excited at its resonant frequency, i.e., $\hbar\omega_{laser} + \hbar\omega_m = \hbar\omega_{cavity}$, thus cooling the mirror. The reverse process leads to heating of the mirror when the cavity is excited at $\hbar\omega_{laser} - \hbar\omega_m = \hbar\omega_{cavity}$. Further details of the analysis in both the classical and quantum limits are discussed in references [1, 13, 14].

These optical resonator systems with movable mirrors are widely used in sensitive detector applications. This idea was first implemented in a Michelson interferometer for detecting gravitational waves in 1978 [15], and continues to be used for this purpose in some of the large scale experiments such as LIGO [16]. Another example of their use as sensitive detectors is in atomic force microscopes [17], where the sharp tip is attached to a mirror coated mechanical beam. The force experienced by the tip whilst scanning the surface is measured from changes to the amplitude/phase of the light field reflected from the beam.

The cooling of mechanical oscillators by the sideband methods was inspired by early experiments that achieved laser cooling of atomic clouds [18]. In recent years, several experiments have been performed to cool mechanical objects of varying masses, with a goal to observe the quantum ground state [19–26]. For example, Arcizet et al [19] used a micromechanical resonator as one of the mirrors in a Fabry-Perot cavity. When the micro-resonator was driven, its vibration changed the optical cavity length and by using a detuned laser to drive the optical cavity, the 814 kHz microresonator was cooled from 300 K to $\approx$ 10 K. Similar work by Gigan et al [20] was performed to cool a 280 kHz micromechanical resonator from room temperature to 8 K. In a more recent work by Groblacher et al [23], a 100 μm long resonator with a frequency of 945 kHz, that formed one of the mirrors in the Fabry-Perot cavity, was cooled from 5.3 K to 1.5 mK, close to the quantum ground state of the mechanical oscillator. The motivation behind these experiments is to test the validity of quantum mechanics to macroscopic objects.

Thus studies based on cooling of macroscopic mechanical oscillators in optical cavities has been successful, and recently, cooling of a 3.68 GHz nanobeam to its ground state by the radiation pressure forces in an optical cavity at 20 K was achieved [27]. In the following section, experiments based on cooling of mechanical oscillators coupled to superconducting microwave cavities are described.

1.2 Microwave Resonators

In recent years, superconducting microwave resonators have been used in studying the interaction between nanomechanical motion and electromagnetic field [2, 3, 11, 28–36]. Large resonator quality factors of over a million can be easily achieved at low temperatures, and this aspect of the resonators enables the effects of minute mechanical displacements to be measured as changes in the microwave resonant frequency. In these experiments, there is usually a capacitive coupling between a mechanical oscillator and a microwave resonator as illustrated in fig. 1.2.

In similarity to the experiments with optical resonators in the quantum limit, the interaction of a nanobar with the microwave field can give rise to sideband cooling and heating [2, 3, 28, 30, 33]. This has been demonstrated in experiments conducted by various research groups, where the main goal was to achieve the quantum ground state and measure the zero point motion of a mechanical oscillator [3, 37]. For example, Teufel et al [11] studied the capacitive coupling of a nanobar to a thin film superconducting microwave resonator as shown in fig. 1.3.

In the good cavity limit, and with a detuned microwave drive signal heating or cooling of the nanobar is observed. This is reflected in its quality factor, i.e., for a red-detuned microwave drive, the nanobar displacement is damped and cooled (from 200 to 140 mK), which is measured as a decrease in its quality factor and for a blue-detuned microwave signal, there is amplification and heating (from 200 to 280 mK),

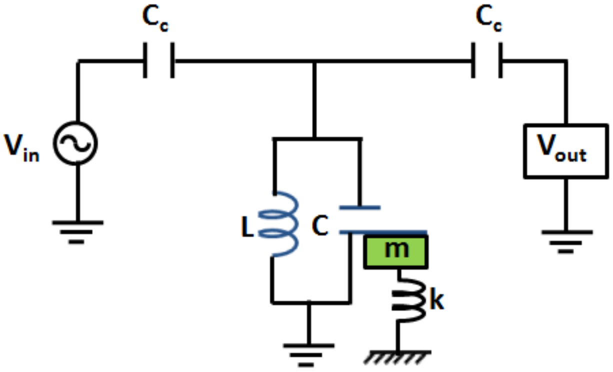

Figure 1.2: A schematic representation of the interaction of a microwave resonator with a mechanical oscillator. Here the microwave resonator is represented by an electrical (LC) oscillator circuit. The mechanical oscillator is shown as being one of the capacitor plates of the electrical circuit. Its movement causes a change in the microwave capacitance and hence in the microwave resonant frequency.

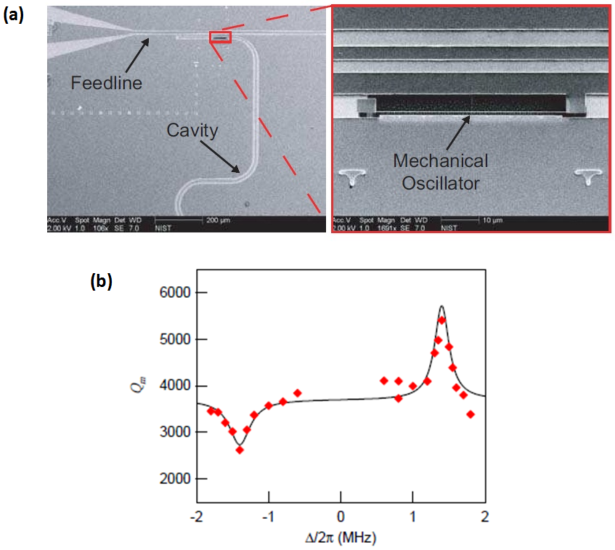

Figure 1.3: (a) Coupling of a nanobar (mechanical oscillator) to a microwave resonator. The high and low frequency drive signals are capacitively coupled to the system from the feedline. The nanobar is 50 μm long with a cross-sectional area of ≈ 100 nm^2 and has a fundamental frequency of $\omega_m = 1.41$ MHz. The microwave resonator has a fundamental frequency of 7.55 GHz. (b) The variation of the *nanobar* quality factor w.r.t detuning of the microwave drive signal. The measurements are made in a dilution refrigerator with a base temperature of 20 mK. This figure is from [2].

shown by an increase in the quality factor, as illustrated in fig. 1.3. A quantum mechanical description of this effect is provided in [2], but physically, it can be explained in terms of absorption of energy or positive damping from the nanobar when the microwave field is red detuned and hence cooling and lowering of its quality factor. The reverse effect takes place for a blue detuned microwave drive and hence there is an increase in the mechanical quality factor.

Further cooling to the ground state was limited by the coupling between the nanobar and the microwave field. Hence, another experiment was performed by Teufel et al in [3] where, instead of a nanobar, a micromechanical membrane, is coupled to a superconducting microwave resonator, as shown in fig. 1.4.

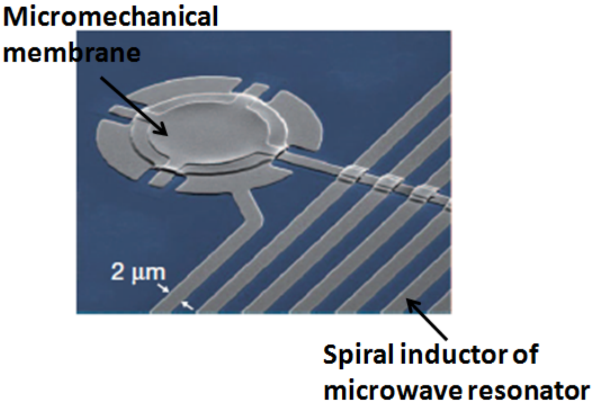

Figure 1.4: The coupling of a thin aluminium membrane to a microwave resonant circuit. The microwave resonator is fabricated on thin film aluminium (grey regions) on a sapphire substrate (blue regions). The membrane is 15 μm in diameter, 100 nm thick, is suspended 50 nm above the aluminium layer on the substrate and has its resonant frequency at 10.56 MHz. The microwave resonant circuit comprises a spiral inductor, and a capacitor formed by the membrane and ground plane underneath it. The microwave resonator has a frequency that is dependent on the membrane position, and is centred at 7.54 GHz. This figure is from [3].

In this system, there was greater coupling between the microwave field and the mechanical oscillator and hence cooling to the quantum ground state was achieved. This paves way for experiments involving quantum information processing, and more recently proposed methods of coupling microwave and optical cavities via a mechanical oscillator [1,38].

1.3 Proposed experiment

Our experiment is largely based on a theoretical model described by G.Heinrich and F.Marquardt [4] which proposes the coupling of a nanobar to a pair of weakly coupled, identical, superconducting microwave resonators at or close to the avoided crossing : In a system where the identical resonators are uncoupled, they have the same resonant frequency. This degeneracy in the frequency is lifted in the presence of a weak coupling between them, and hence, when the resonators are identical, there is a splitting between the frequencies determined by the coupling between them, also known as the avoided crossing of the frequencies, as shown in fig.1.5d. This effect is explained in more detail in sections 2.5.1 and 2.5.2 of this thesis. More importantly, the splitting in the frequencies at the crossing can be chosen to be of the order of nanobar resonant frequencies ($1 - 20$ MHz), the regime in which this theoretical model is applied.

There are two proposed ways of coupling the nanobar so that its displacement : (a) alters the resonant frequency of only one of the microwave resonators and (b) alters the resonant frequencies of both, in anti-phase. These two cases are explained in the following subsections.

1.3.1 Coupling the nanobar to one of the microwave resonators

The proposed model is illustrated in fig. 1.5, where α_L and α_R are two identical microwave resonators, that are weakly coupled along the overlap length (d_g), which is much smaller than the length of the resonators (d). In this case, a nanobar is placed between the other end of α_L and the ground plane. The nanobar displacement changes the capacitance of α_L, and hence its resonant frequency linearly, as shown by the sloping dashed line in fig. 1.5d.

As in the case of optical resonators, in the good cavity limit, vibration of the nanobar causes additional excitations of the microwave frequency spectrum at the drive frequencies $\omega_0 \pm \omega_1$ for both the branches in fig. 1.6.

A particularly interesting case is when, a) the resonant frequency of the nanobar $\omega_1 \sim$ the splitting frequency 2g, and b) when the mechanical drive level is large. Here, the microwave resonances become split as predicted in fig. 1.6b. The effect of both limiting cases of the small and large amplitude mechanical drive on the microwave resonances are discussed in detail in chapter 6 of the thesis.

1.3.2 Coupling the nanobar to both the microwave resonators

When the nanobar is placed in between both the resonators as shown in fig. 1.7, its displacement affects the resonant frequencies anti-phase to one another, i.e., for example, if there is an increase in the capacitance of α_L, then, at the same time, there is a decrease in the capacitance of α_R. Here, the microwave field is coupled to the square of the nanobar displacement, and therefore an intriguing feature of this system is that cooling the nanobar to the ground state would enable quantum non-demolition measurements of the phonon number in the nanobar [4, 22, 39, 40].

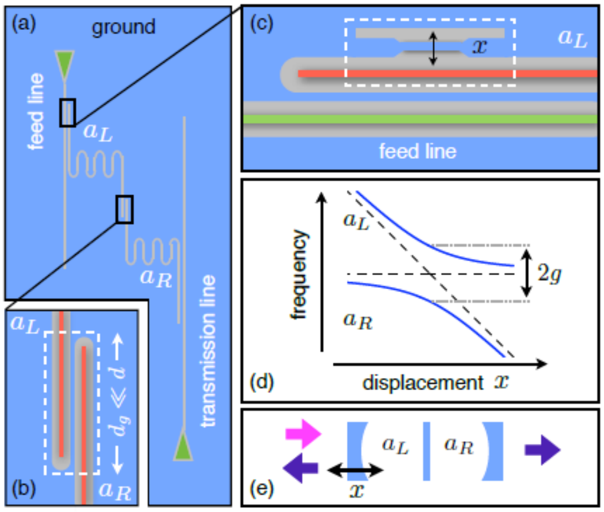

Figure 1.5: (a) The proposed geometry of a system of two identical, coupled, microwave resonators labelled as α_L and α_R. A microwave signal from a signal generator passes through the feedline and is capacitively coupled to the resonators. The transmitted signal from the resonators is measured at one of the ends of the transmission line. (b) Shows the overlap region of the two resonators which determines the magnitude of the coupling capacitance and hence the splitting in the microwave frequencies. (c) The coupling of a nanobar between one end of α_L and the ground plane is shown. (d) The displacement of the nanobar at a low frequency causes the resonant frequency of α_L to change linearly (sloping dashed line), leaving the resonant frequency of α_R unaffected. The splitting in the frequencies at the *avoided crossing* is shown as 2g. (e) A schematic of an analogous coupled optical resonator system in which one of the mirrors is movable. This figure is from [4].

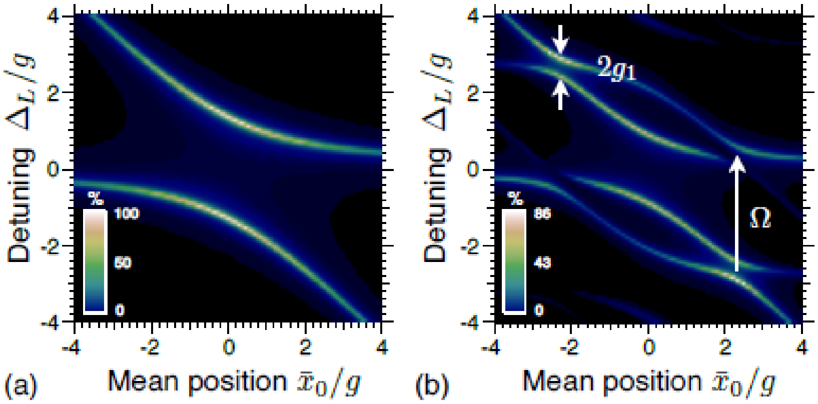

Figure 1.6: Calculated frequency detuning of α_L due to the displacement of the nanobar. The detuning is expressed by $\Delta_L = \omega_L - \omega_0$, where ω_0 is the frequency of α_L when the nanobar displacement, $x = 0$. (a) Transmission from the resonators for various positions of the nanobar in the absence of its oscillation, i.e., $x(t) = x_0$. (b) The transmission from the microwave resonators when the nanobar is driven with a large amplitude of the drive signal, i.e., $x(t) = Acos(\omega_1)t + x_0$. Additional splitting of the microwave resonances are shown. This figure is from [4].

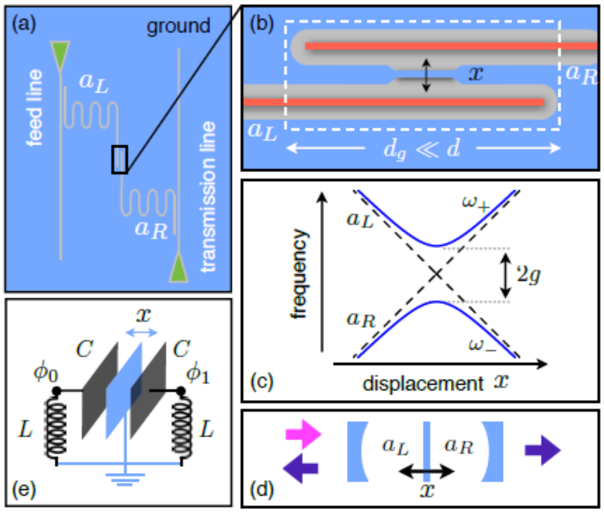

Figure 1.7: (a) A schematic to show the coupling of the nanobar to both the resonators. (b) Shows the overlap region of the resonators where the nanobar is placed. (c) The displacement of the nanobar changes the resonant frequency of both the resonators. (d) An analogous system of optical resonators. (e) An equivalent LC circuit model. This figure is from [4].

The nanobar is effectively a harmonic oscillator and, quantum mechanically, its vibrational amplitude is monotonically related to the number of phonons connected with this motion. An energy eigenstate (Fock state) is one in which there are a fixed number of quanta in the state. The nanobar displacement cannot be used to measure the energy eigenstate because of the uncertainty principle, but measurement of the displacement squared can be made, since it is a quantum non-demolition measurement (QND), i.e. we can make repeated measurements on the state and get the same result. The scheme in which the nanobar is placed between the two resonators is of particular interest because, close to the avoided crossing, the frequency of both upper and lower branches are quadratic in the nanobar displacement. Measurement of these frequencies would therefore provide (at least, in principle,) a QND measurement of the energy state of the bar and jumps between these states would be observable. As noted in [4], there are serious sensitivity issues, hence there is a need for long nanobars which give maximal change in the microwave resonators' capacitance and hence in their resonant frequencies.

This system can therefore be used for measuring quantum mechanical properties on a macroscopic object as the question of whether a macroscopic system could behave quantum mechanically has been a long standing question since Schrödinger proposed his famous cat experiment. The first demonstration that a macroscopic object could behave quantum mechanically was by Friedman et al [41], who showed that a superconducting loop containing a single superconducting weak link could be put into a superposition of two distinct quantum states. One of these corresponded to a clockwise circulating current and the other to an anticlockwise circulating current. The system is truly macroscopic, in that the circulating currents in this experiment correspond to some 10^{10} correlated electrons. A somewhat different question is the extent to which a macroscopic mechanical oscillator can display quantum properties, which is the motivation behind the present work.

1.4 Outline of the thesis

The experimental methods that were employed to study the coupled resonators system as proposed by the theoretical model of G.Heinrich and F.Marquardt [4] are described in this thesis.

- In chapter 2, the background theory required for the understanding of the experiment is explained.
- In chapter 3, the design considerations for the coupled resonator devices, the fabrication methods used, the experimental set-up, and the preliminary results from low temperature measurements on the devices are explained. It was seen that the measured frequencies and their splitting deviated from the theoretical values and hence required modifications to the resonator geometries.
- In chapter 4, the improvements achieved with the new geometries are shown. The measurements on the new devices indicated that the resonators were non-identical and therefore, one of them needed to be tuned to reach the avoided crossing.
- In chapter 5, a mechanism that was designed for in-situ tuning of one of the resonators and its successful implementation on the devices are explained.
- In the absence of nanobars, an experiment was designed to vary the microwave inductance instead of its capacitance by means of applying an RF magnetic field from current-carrying coils. In chapter 6, the effect of this perturbation is analysed theoretically for two limiting cases of small and large amplitude of current drive through the coils. Also, the experimental set-up that was designed to measure this effect, and the results from preliminary measurements are discussed.
- Finally, in chapter 7, the conclusions of this work and the prospects for future experiments are summarized.

CHAPTER 2

BACKGROUND THEORY

In this chapter, some of the basic concepts of superconductivity and microwave resonators are summarised. Since the theory of both fields is extensive, only those aspects required for the understanding of our experiments are covered. More details will be dealt with in later sections as appropriate.

2.1 Superconductivity

It is well known that that when most metals are cooled to temperatures close to 0 K, their electrical resistivity drops to a value that depends on the purity, due to a reduction in the electron-phonon scattering in the metal lattice. When a superconducting metal is cooled, the initial lowering in its electrical resistivity is similar to that of a conventional metal, however, at a certain critical temperature $\mathrm{T_C}$, its resistivity to a dc current drops to zero [42]. The defining feature of a superconductor that distinguishes it from a perfect conductor is the expulsion of an applied magnetic flux, also known as the Meissner effect [43]. A superconductor therefore behaves as a perfect diamagnetic material and the flux is expelled as long as the field strength is below a critical value, defined as H_C. The expulsion of flux occurs as a result of screening currents that flow along the surface of the material, thereby confining the magnetic field within a small depth, known as the London penetration depth, λ_L.

Based on a phenomenological theory, the two fundamental properties of zero resistance and perfect diamagnetism of a superconductor can be expressed in the form of the London equations [44]:

$$\frac{d\mathbf{J_s}}{dt} = \frac{n_s e^2}{m}\mathbf{E} \tag{2.1}$$

and

$$\nabla \times \mathbf{J_s} = -\left(\frac{\mu_0 n_s e^2}{m}\right)\mathbf{H} \tag{2.2}$$

where, J_s is the supercurrent density, n_s is the number density of superconducting electrons, m and e are the mass and charge of an electron, **E** and **H** are electric and magnetic fields respectively.

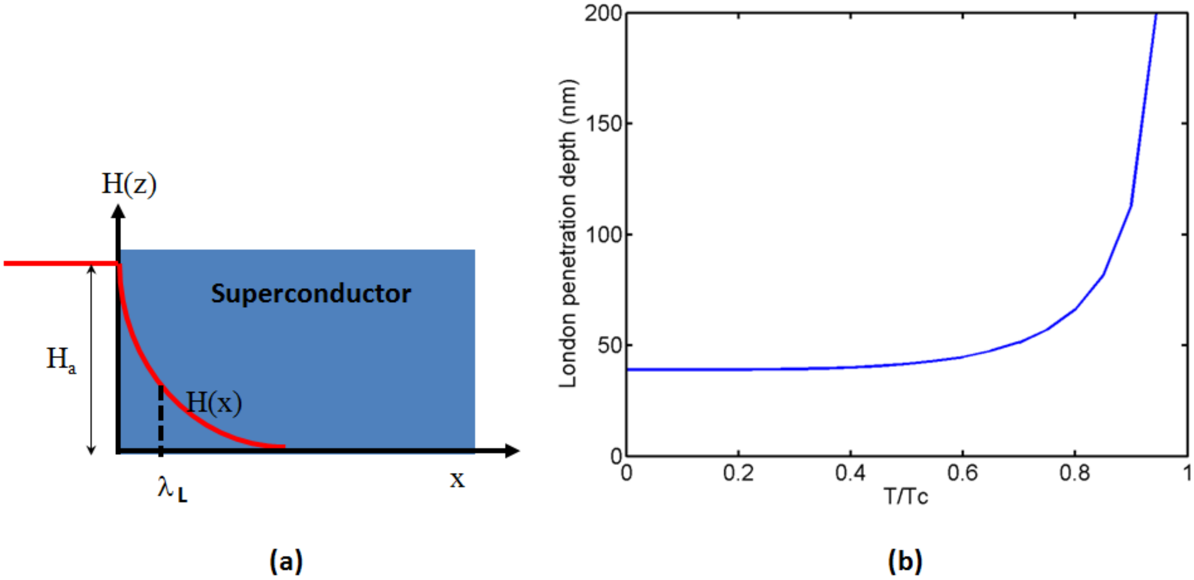

Figure 2.1: (a) The flux distribution on the surface of a superconductor. (b) The variation of λ_L with temperature for a sample with $\lambda_L(0) = 40$ nm.

Using eq. 2.2, the distribution of magnetic flux within a superconductor can be obtained as:

$$\mathbf{H}(x) = \mathbf{H}_a e^{-x/\lambda_L} \tag{2.3}$$

where, $H(x)$ is the flux at a distance x inside the superconductor, H_a is the flux applied parallel to the surface of the superconductor in the z direction and λ_L is the London penetration depth defined as:

$$\lambda_L = \left(\frac{m}{\mu_0 n_s e^2}\right)^{1/2} \tag{2.4}$$

It can be seen from eq. 2.3 that the magnetic flux decays exponentially at the surface of a superconductor within a distance λ_L. Since $\lambda_L \propto {n_s}^{-1/2}$, and n_s varies with temperature (shown in section 2.7), the penetration depth has the following temperature dependence [45]:

$$\lambda_L^2(T) = \frac{\lambda_L^2(0)}{\left[1 - \left(\frac{T}{T_C}\right)^4\right]} \tag{2.5}$$

The London theory was sufficient to describe the basic macroscopic features of a superconductor, but not its microscopic behaviour. One of the early theories that explained the microscopic behaviour was suggested by Fröhlich [46]. He postulated that in a superconductor, electron pairs were formed through an interaction with the lattice wherein, an electron emits a virtual phonon which is immediately absorbed by a second electron, which could result in a weak attractive force between two electrons.

It was then proposed by Cooper that two electrons of equal and opposite spin could couple together by an interaction with the lattice to form a Cooper pair. This result was further extended by Bardeen, Cooper, and Schrieffer (BCS) to all the electrons in a superconductor and their microscopic properties were explained [47]. The BCS theory postulated that the Cooper pairs formed the charge carriers in a superconductor and their number density could be described in terms of the superconducting order parameter,

$$\Psi_{\mathbf{P}} = \Psi e^{i(P.r)/\hbar} \tag{2.6}$$

where $|\Psi_P|^2$ is the number density of Cooper pairs and P is the momentum per pair.

The BCS theory also explained that the formation of Cooper pairs results in a lower energy (ground) state of a superconductor, which is analogous to the condensation of atoms in a gas to the lowest energy ground state when cooled to very low temperatures. A minimum energy was therefore required to break the Cooper pairs to form two, higher energy quasi-particles. The energy gap between the BCS ground state and the higher energy states was estimated by BCS to be $\mathrm{E_g} = 2\Delta \approx 3.5\mathrm{k_B T_C}$ for $\mathrm{T} \ll \mathrm{T_C}$, which showed good agreement with the experimental data of Glover and Tinkham [48].

Prior to the BCS theory, it was postulated by Ginzburg and Landau (GL) [49] that the response of a superconductor to a magnetic field mainly depends on two characteristic length scales: the London penetration depth $\lambda_L(T)$ and, the GL coherence length $\xi_{GL}(T)$, which defines the spatial extent of the Cooper pair wavefunction. The ratio of these two quantities is called the GL parameter, $\kappa = \lambda_L(T)/\xi_{GL}(T)$. Materials with $\kappa < 1/\sqrt{2}$ are known as type-I superconductors in which, a complete Meissner state is maintained below a critical field H_C; above this field, the normal state is restored.

In some metals and alloys, however, $\kappa > 1/\sqrt{2}$, and these form a different category, called the type-II

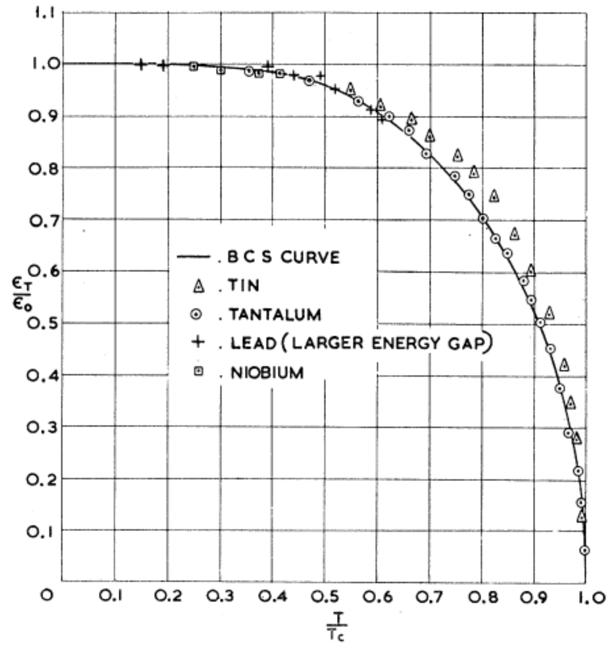

Figure 2.2: The energy gap as a function of reduced temperature. This picture is taken from [5].

superconductors. In this case, the superconducting state is characterized by lower and upper critical fields defined as H_{C1} and H_{C2}. A pure Meissner state is maintained until the applied field $H_a = H_{C1}$. When $H_{C1} < H_a < H_{C2}$, a mixed state is obtained; for $H_a > H_{C2}$, the superconducting state is completely destroyed.

In the mixed state, quantized flux lines penetrate into the bulk of the superconductor and form a flux line lattice. In the presence of a transport current, the flux lines experience a Lorentz force that causes them to move and this in turn results in an emf, opposite in direction to that applied. Therefore, the flux line motion is a resistive process and must be avoided to reduce losses within the superconductor [50].

2.2 Complex conductivity of superconductors

It was mentioned earlier that in a superconductor there is no resistance to the flow of a constant current. In the presence of alternating currents however, there is non-zero dissipation of power and the source of loss may be explained by the two-fluid model proposed by Gorter and Casimir [45]. In this model it is assumed that when $T \neq 0$, the electrons in a superconductor fall into two categories, namely the normal, and the superconducting electrons. Therefore, the total number density $n = n_s + n_n$, where n_s is the number density of superconducting electrons, and n_n, is the number density of normal electrons. The temperature dependence of the electron density is approximately of the form:

$$\frac{n_s}{n} = 1 - \left(\frac{T}{T_C}\right)^4 \tag{2.7}$$

It can be seen from London's first equation that in the presence of an alternating current J_s, there is an electric field which accelerates the superconducting electrons. Due to a finite mass of the electrons, there is inertia, which results in a phase lag in the current. Therefore, there is an inductive impedance, also known as the kinetic inductance of the superconducting electrons. The electric field also acts on the normal electrons and they undergo collisions with the lattice, resulting in dissipation of power.

In the presence of a time varying current, the total current density is given by

$$J = J_n + J_s \tag{2.8}$$

$$J = (\sigma_1 - i\sigma_2)\, E \tag{2.9}$$

where the complex conductivity σ consists of the real part σ_1 due to the normal electrons and the imaginary part, σ_2 due to the superconducting electrons.

The expressions for σ_1 and σ_2 are [50]:

$$\sigma_1 = \frac{n_n e^2 \tau_n}{m(1 + (\omega\tau_n)^2)} \tag{2.10}$$

and

$$\sigma_2 = \frac{n_n e^2 (\omega\tau_n)^2}{m\omega(1 + (\omega\tau_n)^2)} + \frac{n_s e^2}{m\omega} \tag{2.11}$$

where m is the mass of an electron, τ_n is the relaxation time of a normal electron, and ω is the frequency of the alternating current in the superconductor. In eqs. 2.10 and 2.11, it is assumed that $\omega\tau_n \ll 1$. The two fluid model is only a phenomenological description of the total conductivity of electrons at low frequencies but is not valid for $\omega > \Delta$ since it does not account for the energy gap in superconductors. A more accurate description is provided by the Mattis-Bardeen theory [51].

2.3 Kinetic Inductance

It was mentioned earlier that in the presence of an alternating current there is an inductive impedance associated with the Cooper pairs, which is also called as the kinetic inductance. Therefore, apart from the

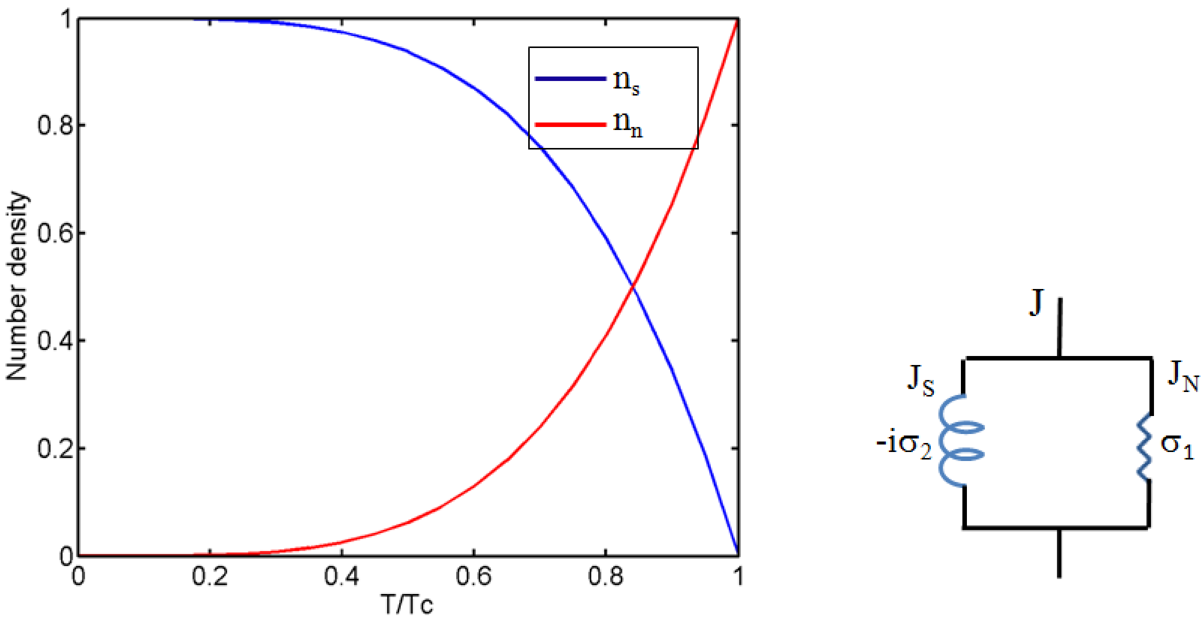

(a) (b)

Figure 2.3: (a) Shows the temperature dependence of the superconducting and normal electron densities as a function of temperature. (b) The inductive and ohmic impedances to a current in a superconductor.

magnetic energy stored due to the geometric inductance of the superconductor, there is a kinetic energy associated with the velocity, v_s of the Cooper pairs:

$$U = \frac{1}{2} n_s m v_s^2 \tag{2.12}$$

Since the current density associated with n_s is given by $J_s = n_s e v_s$, the kinetic energy can be expressed as

$$U = \frac{1}{2} L_K I^2 = \frac{1}{2} \mu_0 \lambda_L^2 J_s^2 \tag{2.13}$$

where L_K is the kinetic inductance per unit length. For the geometry of our resonators as illustrated in fig. 2.4, $L_K = \mu_0 \lambda_L$, hence $L_K \propto {n_s}^{-1/2}$. In the case when the slab is thin compared to the penetration depth, $L_K \propto \lambda_L^2$ [52].

This is an important effect as the total inductance of our resonator structures is given by $L = L_G + L_K$, where L_G is the geometric inductance and L_K is the kinetic inductance. Since the resonant frequency $f \propto L^{-1/2}$, a change in L_K alters f_0. An important application of this property is the use of superconducting

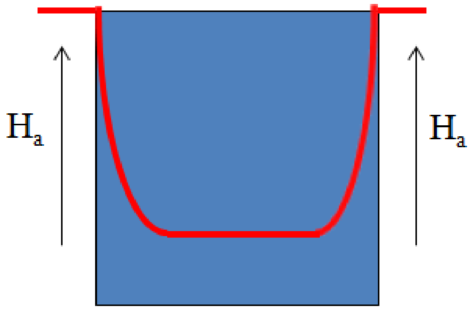

Figure 2.4: The field distribution within a flat superconducting slab with a width and thickness $\gg \lambda_L$.

resonators as kinetic inductance detectors [53, 54]. When a photon of energy greater than 2Δ is absorbed by the resonator, it results in the breaking of Cooper pairs and hence a reduction in n_s. This causes an increase in L_K, which can be measured as the lowering of its resonant frequency.

2.4 Coplanar resonators

The resonator devices used for this project were designed in the coplanar waveguide (cpw) geometry due to advantages such as its ease of fabrication and high quality factors [55–58]. This geometry is used in a wide variety of applications, for example, in surface impedance measurements of thin film superconductors [59], tunable resonators [9] and, in recent years, for qubit experiments that enable quantum information processing [58, 60]. A standard cpw resonator consists of a low loss dielectric substrate, on which narrow strips of conducting metal separated from the ground plane on either side are patterned, as illustrated in fig. 2.5a. The electrical properties of a cpw resonator are usually described using a transmission line model in which the quantities of inductance and capacitance are distributed along its length. More details of the general properties of transmission lines are provided in [6] and here only the relevant case of a terminated, lossless line is discussed as it is a close description of our real system. In this case, voltage and current standing waves are set up along its length and can be expressed as [6]:

$$V(z) = V_0^+(e^{-j\beta z} + \Gamma e^{j\beta z}) \tag{2.14}$$

$$I(z) = \frac{V_0^+}{Z_0}(e^{-j\beta z} - \Gamma e^{j\beta z}) \tag{2.15}$$

where, V_0^+ is the amplitude of the standing waves, $e^{-j\beta z}$ represents the wave propagation in the +z direction and $e^{j\beta z}$ the wave propagation in the −z direction, β is the phase constant, $Z_0 = \sqrt{\frac{L}{C}}$ is the characteristic impedance, and Γ is the voltage reflection co-efficient defined as

$$\Gamma = \frac{V_0^-}{V_0^+} = \frac{Z_L - Z_0}{Z_L + Z_0} \tag{2.16}$$

where Z_L is the impedance of the load.

In our devices, the resonator is open at both ends and therefore supports half-wavelength (n$\lambda/2$) standing wave modes. In the transmission line model, this is represented by $Z_L \to \infty$. Therefore, from eq.2.16, we obtain $\Gamma = 1$ and the standing waves are then given by:

$$\begin{aligned} V(z) &= 2V_0^+ \cos \beta z & (2.17) \\ I(z) &= \frac{-2j}{Z_0} V_0^+ \sin \beta z & (2.18) \end{aligned}$$

In order to design our devices, it is necessary to determine the distributed quantities of the resonator parameters. These quantities have already been determined for a conventional cpw resonator using conformal mapping techniques [55] and the final expressions are given by:

$$\begin{aligned} L_l &= \frac{\mu_0}{4} \frac{K\left(\sqrt{1-k^2}\right)}{K(k)} & (2.19) \\ C_l &= 4\epsilon_0 \epsilon_{eff} \frac{K(k)}{K\left(\sqrt{1-k^2}\right)} & (2.20) \\ Z_0 &= \sqrt{\frac{L_l}{C_l}} = \frac{30\pi}{\sqrt{\epsilon_{eff}}} \frac{K\left(\sqrt{1-k^2}\right)}{K(k)} & (2.21) \\ k &= \frac{s}{(s+2w)} & (2.22) \end{aligned}$$

where L_l and C_l are the inductance and capacitance per unit length of the resonator, Z_0 is its characteristic impedance, *K(k)* is the complete elliptic integral of the first kind, ϵ_{eff} is the effective permittivity defined as the average of the permittivities of the substrate and free space, s is the width of the centre track and w is the gap between the centre track and the adjacent ground planes.

Usually, the ratio $k = \frac{s}{(s+2w)} = 0.5$ is chosen while designing the resonators, for which $K(k)/K\left(\sqrt{1-k^2}\right) = 0.78$ [61]. This results in a characteristic impedance, $Z_0 \approx 50\ \Omega$. It is essential to maintain this value of Z_0 in order to match with the input and output impedances of the microwave measurement apparatus.

The frequency modes for a $\lambda/2$ cpw resonator can be calculated as:

$$f_n = \frac{n v_{ph}}{2l} = \frac{nc}{2l\sqrt{\epsilon_{eff}}} = \frac{n}{2l\sqrt{L_l C_l}} \tag{2.23}$$

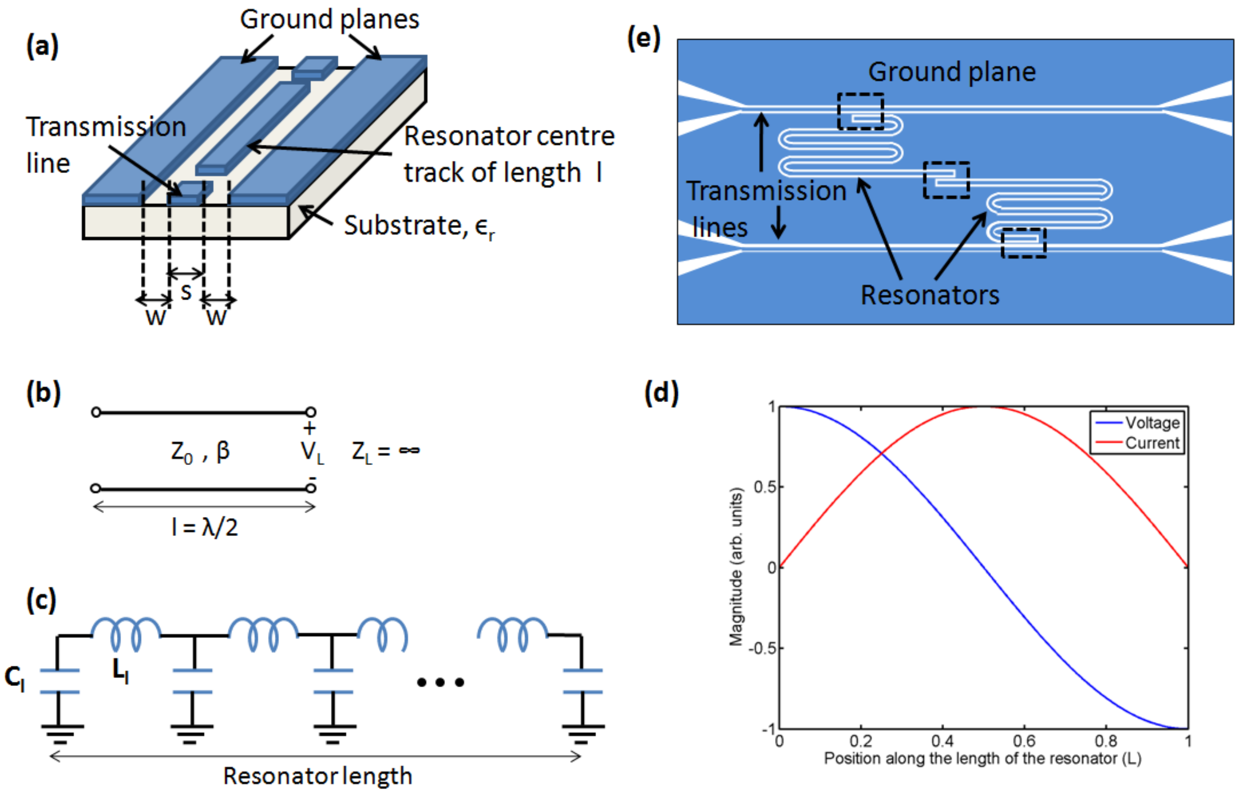

Figure 2.5: (a) Schematic of a cpw resonator. A microwave signal is coupled into and out of the resonator by a gap capacitance formed between the centre track and the corresponding transmission lines. The width of the centre tracks is denoted by s and w is the distance between the centre tracks and the lateral ground planes. (b) A transmission line model of the resonator. The line is open at both ends and supports half-wavelength ($\lambda/2$) voltage and current standing wave modes. Adapted from [6] (c) The inductance and capacitance of the resonator are distributed along its length. (d) The fundamental voltage and current standing waves in a $\lambda/2$ cpw resonator. (e) A schematic of our coupled resonators system adapted from [4]. The resonators are surrounded by lateral ground planes as in a cpw geometry. However, the microwave signal is coupled into and out of the resonators by a capacitance that is formed in the overlap regions (dashed boxes) of the resonator and transmission line centre tracks.

where v_{ph} is the phase velocity of the wave, l is the length of the resonator and $n = 1, 2, 3....$

The resonators parameters used for designing our devices were calculated using $K(k)/\sqrt{1-k^2} = 0.78$ for $k = 0.5$ and are listed in table 2.1.

Parameter	Value
L_l	4×10^{-7} H/m
C_l	1.7×10^{-10} F/m
l	1.1×10^{-2} m
ϵ_r	11.7

Table 2.1: The resonator parameters used for designing our resonators. The dielectric constant of the silicon substrate is assumed as $\epsilon_r = 11.7$

2.4.1 The Quality factor of a resonator

In general, the quality factor of a resonator is defined as

$$Q = 2\pi \frac{\text{Energy stored}}{\text{Energy lost per cycle}} \tag{2.24}$$

The measured quality factor of a microwave resonator is determined by losses that are both intrinsic and extrinsic to it. The losses that are intrinsic to the resonator determine its internal quality factor, Q_{int} defined as

$$\frac{1}{Q_{int}} = \frac{1}{Q_r} + \frac{1}{Q_c} + \frac{1}{Q_d} \tag{2.25}$$

where, $1/Q_r$, $1/Q_c$ and $1/Q_d$ account for losses due to radiation, conduction and the dielectric substrate [56]. In superconducting resonators, these losses are minimised resulting in large quality factors ($\sim 10^6$) [9,62].

In practical applications, a resonator is connected to an external load to enable measurements. This contributes to losses that are extrinsic to the resonator. The loaded quality factor, Q_L is given by

$$\frac{1}{Q_L} = \frac{1}{Q_{int}} + \frac{1}{Q_{ext}} \tag{2.26}$$

where Q_{ext} is the external quality factor, and in our devices, depends on the magnitude of capacitive coupling of the microwave signal into and out of the resonators. This is explained in more detail in section 3.1.2.

2.4.2 Factors affecting the resonant frequency

The resonant frequency of a superconducting microwave resonator is influenced by factors such as the operating temperature, the magnitude of the signal used to drive the resonator, and the application of an external magnetic field.

All the measurements on our devices are made at $T = 1.3 - 1.4$ K, well below the T_C of niobium, where n_s is nearly independent of temperature. It was shown in section 2.3 that the kinetic inductance $L_K \propto n_s^{-1/2}$ and therefore, during the course of an experiment, the instabilities in L_K are very small. Hence, the total inductance of the resonator which is $L_T = L_G + L_K$ remains nearly constant and changes to the resonant frequency are negligible.

It was reported by Pippard [63] in 1950 that the penetration depth λ_L has a quadratic dependence on an applied magnetic field such that for H $\ll$ H$_C$, $\delta\lambda_L(T,H) \propto \frac{H^2}{H_C^2}$ which leads to a quadratic dependence of the resonant frequency on H. A microscopic theory proposed by Bardeen [64] showed the following dependence:

$$f(T,H) = f(T,0)\left[1 - \frac{L_K(T,0)}{L_T}\beta(T)\frac{H^2}{H_C^2}\right] \tag{2.27}$$

This equation is taken from [9]. It will be seen in section 6.2.1 that this effect could be used to tune the resonant frequencies of our devices.

The magnitude of the drive signal can also affect the frequency of a superconducting microwave resonator via the field induced by the drive current. Increasing the drive level results in an increase in the kinetic inductance, thereby lowering its resonant frequency. A non-linearity in the resonant peaks arises at high drive levels which causes a drop in the quality factor of the resonator. Hence, all our measurements are confined to low drive levels in the linear regime.

2.5 Coupled resonators

As stated in section 1.3, our intended experimental system comprises coupled microwave resonators in which, the coupling of a nanobar to one of the resonators alters its capacitance. Prior to a discussion on the microwave resonators, a system of coupled mechanical oscillators is considered as it is conceptually easier to understand.

2.5.1 Mechanical model

Consider a system of two spring-mass oscillators that are weakly coupled as shown in fig. 2.6. Let mass m_1 be displaced by a force Fcos(ωt). Then, the equations of motion for both the masses are given by:

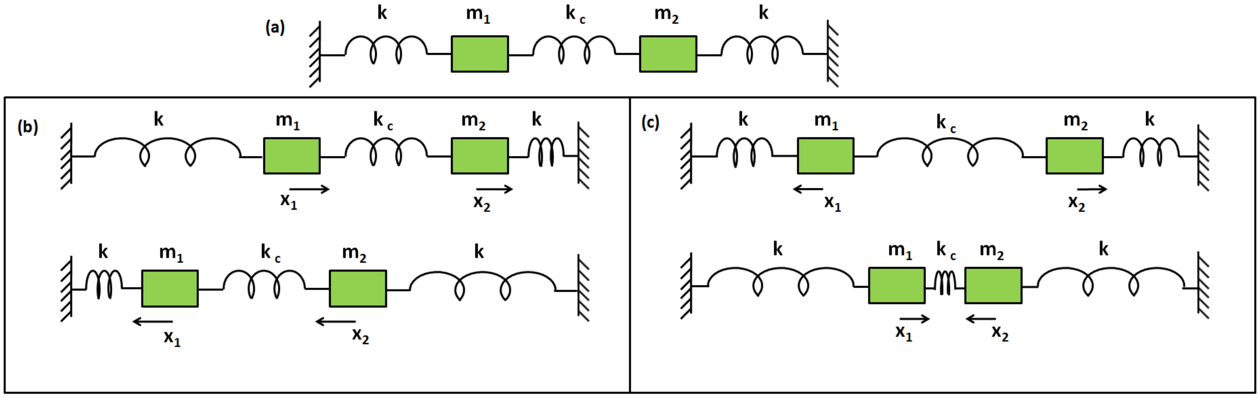

Figure 2.6: (a) A system of coupled mechanical oscillators. Masses m_1 and m_2 are attached by springs of stiffness, k to their respective supports. There is a weak coupling between m_1 and m_2 due to k_c, where $k_c \ll k$. (b) The symmetric normal modes of oscillation. The displacement of the masses from their equilibrium position is denoted by x_1 and x_2. (c) The anti-symmetric normal modes of oscillation.

$$m_1 x_1^{''} = Fcos(\omega t) - kx_1 - k_d x_1^{'} + (x_2 - x_1)k_c \tag{2.28}$$

$$m_2 x_2^{''} = -kx_2 - k_d x_2^{'} + (x_1 - x_2)k_c \tag{2.29}$$

The solutions to eqs. 2.28 and 2.29 are provided in appendix A.1. The normal modes of oscillation in this system are given by

$$\omega^2 = \frac{(k+k_c)(m_1+m_2) \pm \sqrt{(k+k_c)^2(m_1+m_2)^2 - 4m_1m_2[(k+k_c)^2 - k_c^2]}}{2m_1m_2} \tag{2.30}$$

Further simplification results in a lower frequency symmetric mode, and a higher frequency anti-symmetric mode of oscillation. In the symmetric mode, the displacement of the masses are in phase with each other, and the coupling spring does not alter the frequency of oscillation. In the anti-symmetric mode, the masses are displaced out of phase and, the coupling spring, k_c is either compressed or stretched resulting in higher frequency of oscillation of the masses.

An important feature of this system is that as the mass of one of the resonators is varied, an avoided crossing of the frequencies is obtained as shown in fig. 2.7.

2.5.2 Microwave model

It was explained in section 2.4 that a cpw resonator can be represented by a transmission line model which has distributed quantities of inductance and capacitance along its length. In the work reported in the literature, many authors have represented their cpw resonators as lumped element LCR circuits for a simplified analysis and hence a similar approach is taken for the work presented in this thesis. In this section, a system of two identical, coupled, parallel LCR circuits is briefly described.

Applying Kirchoff's laws for the circuit shown in fig. 2.8 the equations for voltages across the current loops can be written as:

$$C_1V_1^{''} = \omega I cos(\omega t) - \frac{V_1^{'}}{R_1} - \frac{V_1}{L_1} + C_c(V_2 - V_1)^{''} \tag{2.31}$$

$$C_2V_2^{''} = -\frac{V_2^{'}}{R_2} - \frac{V_2}{L_2} + C_c(V_1 - V_2)^{''} \tag{2.32}$$

In analogy to the mechanical model, the coupled LCR resonator circuit has two normal modes of oscillation of charge, i.e., symmetric and anti-symmetric modes. In the lower frequency symmetric mode, the oscillation

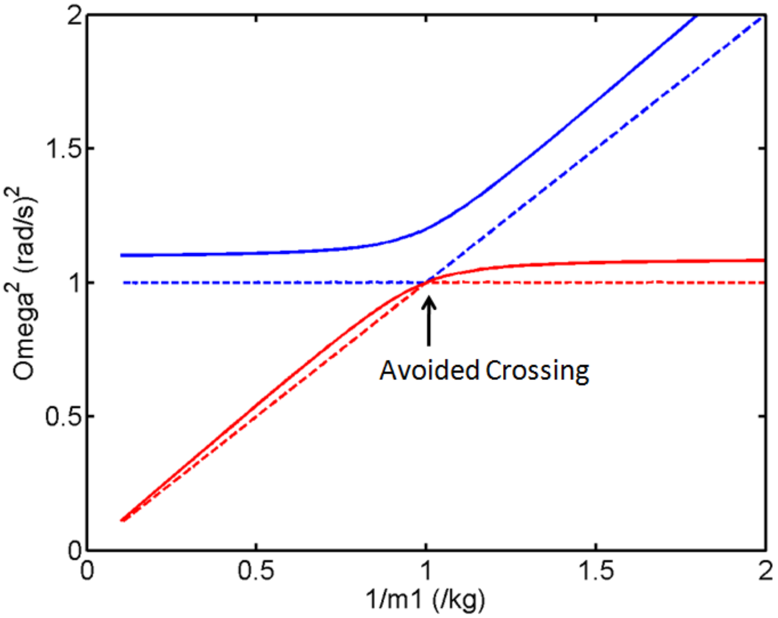

Figure 2.7: The normal modes of a coupled mechanical oscillator as a function of a tunable mass m_1. The dashed lines show the lower and higher frequency modes in the absence of coupling between the masses, and in which case they behave as two independent oscillators. The solid lines are the frequency modes in the presence of a weak coupling between the masses which results in an avoided crossing of the frequencies when both the oscillators are identical.

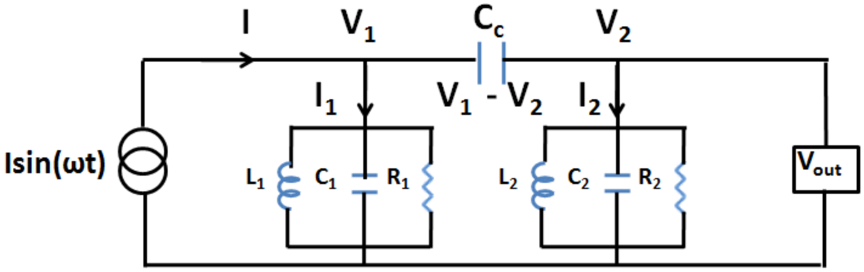

Figure 2.8: A lumped element model: Two identical LCR resonant circuits coupled by a capacitance C_c.

of charge in both resonant circuits are in phase with each other. Hence, they behave like two independent oscillators and the coupling capacitance does not alter the resonant frequency.

In the higher frequency anti-symmetric mode, the oscillation of charge in one of the resonators is out of phase w.r.t that in the other. In this case, charge builds on the plates of the coupling capacitor, thereby altering the resonant frequency. From eqns. 2.28, 2.29, 2.31 and 2.32, an equivalence of the mechanical and electrical models can be seen as shown in table 2.2.

Electrical		Mechanical
V	$\equiv$	x
1/L	$\equiv$	k
C	$\equiv$	m
R	$\equiv$	$1/k_d$
ωI	$\equiv$	F

Table 2.2: Shows the equivalence of the lumped element electrical and mechanical oscillator components.

It should be noted that the mechanical analogue for our experiment differs from the lumped element LCR model in that coupling by a spring is proportional to $(x_1 - x_2)$, whereas that via a capacitor is proportional to $(V_1 - V_2)''$ which introduces a factor of ω^2. However, since we are always dealing with cases where the perturbation frequency, $\omega_1 \ll \omega$, which is set to be unity in our computations, the error is small. Therefore the mechanical model will be still be used for further analysis of our experimental system as detailed in section 6.3.

The frequency of one of the LCR oscillators can be changed relative to that of the other by varying either its capacitance ($\equiv$ m) or its inductance ($\equiv$ 1/k). In a range of experiments involving nanobars, the capacitance of one of the microwave resonators is varied when the nanobar vibrates at a frequency $\omega_1 \ll \omega$. In the mechanical model, this is equivalent to perturbing the mass of one of the resonators. Since the microwave resonant frequency $\omega = 1/\sqrt{LC}$, an time-varying mass can be used to simulate the effect of perturbing the inductance *or* the capacitance and it is dealt with in more detail in section 6.3 and appendix A.1.

The theoretical model by G.Heinrich and F.Marquardt in [4] provides a quantum mechanical description of the coupled resonators and their interaction with a nanobar. However, for the work presented in this thesis, the classical regime is considered and it will be shown in section 6.3 that this analysis provides broadly the same predictions described in [4] and is sufficient for the understanding of the proposed experiment.

2.6 Vibrational modes of nanobars

In order to study a system that involved the coupling of a nanobar to the microwave resonators as described in [4], a basic understanding of the vibrational modes of nanobars is needed and is briefly described in this section.

For a given material, the dimensions of the nanobar determine whether its vibrational motion is controlled by the tension, or by the bending forces, which can cause it to behave like a stretched string, or a thick metal bar clamped at its ends, respectively. When the tension dominates, the vibrational modes of a nanobar are given by [65]:

$$\omega_k = \frac{k\pi}{l}\sqrt{\frac{T}{\rho A}} \tag{2.33}$$

where l is its length, T is the tension, ρ is its density, A is the cross-sectional area and $k = 1, 2, 3...$

When the bending forces, rather than the tension are dominant, its vibrational modes are of the form [66]:

$$\omega_k = \left(\frac{k}{l}\right)^2 \sqrt{\frac{EI}{\rho A}} \tag{2.34}$$

where E is the Young's modulus, I is the bending moment of inertia, ρ is the density, A is the cross-sectional area and $k = 4.73, 7.85, 10.99, 14.14...$

In our proposed experiments with nanobars, the string limit rather than the bending limit was assumed because it has been found to give good agreement with experiments. However, the bending of nanobars at their ends has been found to be a major source of vibrational damping [66, 67].

CHAPTER 3

COUPLED RESONATORS I : DESIGN, FABRICATION AND MEASUREMENTS

In this chapter, the design of coupled resonator circuits, methods to fabricate them on the given substrates, the experimental methods to measure them at low temperatures and the results from measurements on the first set of devices are described.

3.1 Design considerations

Since the resonator devices would be fabricated using conventional photo-lithographic methods, the resonator circuits needed to be designed and patterned on a photo-mask, which would enable their fabrication on the niobium on oxidised silicon substrates. A range of coupled resonator circuits were designed using KIC [68], an integrated circuit layout editor, and sent to Toppan [69] in a compatible format, to be incorporated on a photo-mask. The reason for having several design variations was to utilize maximum space on a $4''$ mask as the cost of manufacturing was independent of the number of circuit designs on it.

The proposed geometry of the coupled resonators device to be used for the initial experiments was adapted from [4], as shown in fig. 3.7. The important design considerations for this geometry were

- The coupling capacitance C_c that determines the amplitudes and quality factors of the resonances,
- The coupling capacitance C_k that determines the splitting in the coupled resonator frequencies,
- The resonator length which determines its fundamental frequency.

The methods used to calculate each of the above parameters and the design variations in the resonator geometries are explained in detail in the following sections.

Simulations of the theoretical models to guide the resonator design were carried out in AIM Spice [70], a commercial circuit analysis programme which performs small signal analysis of resistors, inductors, capacitors and, most importantly transmission lines. Prior to modelling the coupled resonator circuits, simulations were performed to study the effect of C_c on a *single* resonator circuit and compared with similar theoretical analysis in the literature. It was then decided that AIM Spice would be a suitable software to carry out further simulations on coupled resonator circuits, modelled as coupled transmission lines with specified parameters as explained in section 3.1.3.

3.1.1 Calculation of coupling capacitance per unit length

As indicated in fig. 3.7, the magnitudes of the various coupling capacitances were determined by the overlap lengths of the corresponding centre tracks. Hence, it was necessary to first calculate the coupling capacitance per unit length. Simulations were performed in COMSOL [71] and the value was computed as 1.36×10^{-12} F/m in vacuum , for the 2-dimensional geometry shown in fig. 3.1a. It should be noted here that this value of coupling capacitance per unit length was used to calculate both C_c and C_k. The variation of coupling capacitance with overlap length is shown in fig. 3.2.

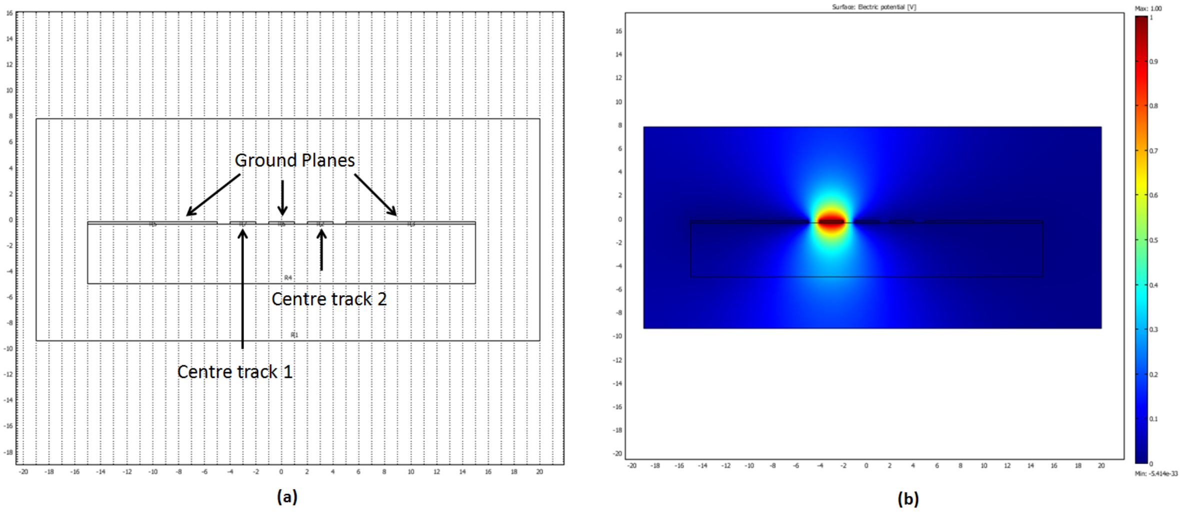

Figure 3.1: (a) End-on view of the geometry used for calculating the coupling capacitance per unit length. A voltage of 1 V is applied to one of the tracks and the charge that accumulates on the other is determined. (b) Shows the electric potential developed in the vicinity of the centre track.

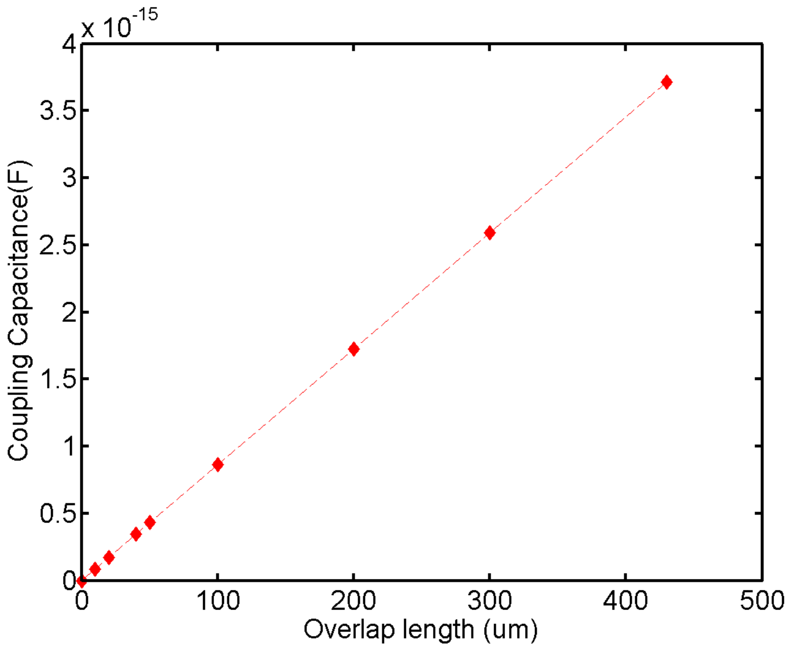

Figure 3.2: The calculated coupling capacitance for various overlap length of the centre tracks.

3.1.2 Simulation of a single microwave resonator

The circuit in fig. 3.3 was simulated in AIM Spice to study the effect of C_c on the loaded quality factor of a single microwave resonator. The resonator with a half wavelength fundamental frequency of 6 GHz was simulated as a transmission line, with specified parameters of length (l), inductance per unit length (L/l) and capacitance per unit length (C/l). The resistance per unit length, R/l of the resonator was included as a variable parameter. In fig. 3.3, the microwave drive signal, denoted by V_{in} is generated by a high frequency oscillator (for example, a network analyser). Z_{out} is the 50 Ω impedance at its output port. The signal is carried by a transmission line of 50 Ω impedance, matched to Z_{out} to prevent reflections of the microwave signal. There is symmetric coupling of the microwave signal into and out of the resonator through a coupling capacitance C_c. The transmitted signal V_{out} is then carried by a 50 Ω transmission line to the input port of the measurement device (for example, again a network analyser), which has an impedance, $Z_{in} = 50\ \Omega$.

The circuit was simulated for a range of C_c values which were calculated for overlap lengths of the resonator and transmission line ranging from $0 - 500\ \mu$m. The values of C_c were determined from the coupling capacitance per unit length described in section 3.1.1.

The values of the resonator parameters that were incorporated into the simulation are listed in table 3.1. The data obtained from this analysis is plotted in fig. 3.4, which shows the effect of C_c on the loaded quality

Simulation Parameter	Value
Resonator length, l	1×10^{-2} m
L/l of resonator	4×10^{-7} H/m
C/l of resonator	1.7×10^{-10} F/m

Table 3.1: The input parameters of a single resonator in AIM Spice

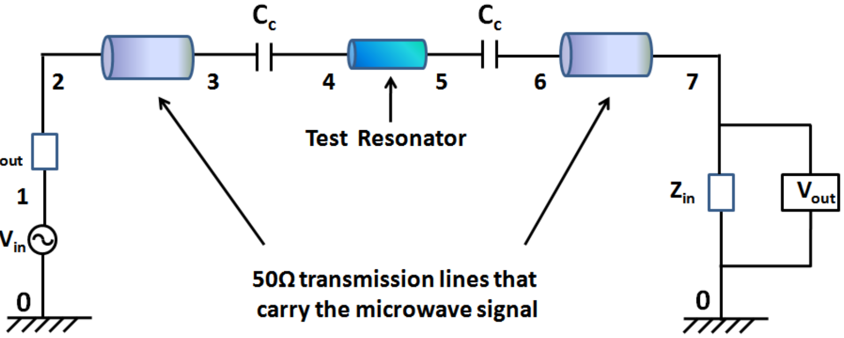

Figure 3.3: Circuit of a single resonator simulated in AIM Spice

factor of resonance for different values of damping in the resonator.

From fig. 3.4, it was inferred that in the over-coupled regime, the capacitive impedance was very small, which caused losses through the 50 Ω transmission line, and hence, $Q_{ext} \ll Q_{int}$. The loaded quality factor Q_L was therefore dominated by Q_{ext} and $Q_L \propto \frac{1}{C_c^2}$.

In the under-coupled regime, the capacitive impedance was large, which limited the measurement of the actual quality factor of the resonance. Here, $Q_{ext} \gg Q_{int}$ and the loaded quality factor, Q_L saturated at Q_{int}, which was determined by the intrinsic damping of the resonator.

The effect of C_c on the loaded quality factor of a single resonator was thus analysed in AIM Spice and the theoretical data in fig. 3.4 followed a pattern similar to reported work in the literature [72]. Subsequently, a coupled resonator circuit was simulated and the effect of C_k on the splitting frequencies was studied, as described in section 3.1.3.

3.1.3 Simulation of coupled microwave resonators

The study of splitting in the coupled resonator frequencies as a function of C_k was an important aspect of this project and hence a theoretical analysis was carried out prior to designing the devices. The circuit in fig. 3.5 was used in AIM Spice to study the effect of C_k in the coupled resonator geometry shown in fig. 3.7.

The measurement apparatus used for the experiments in this project (shown in figs. 3.11 and 3.14) was incorporated into the simulation and measured values of attenuation in the 50 Ω coaxial cables and

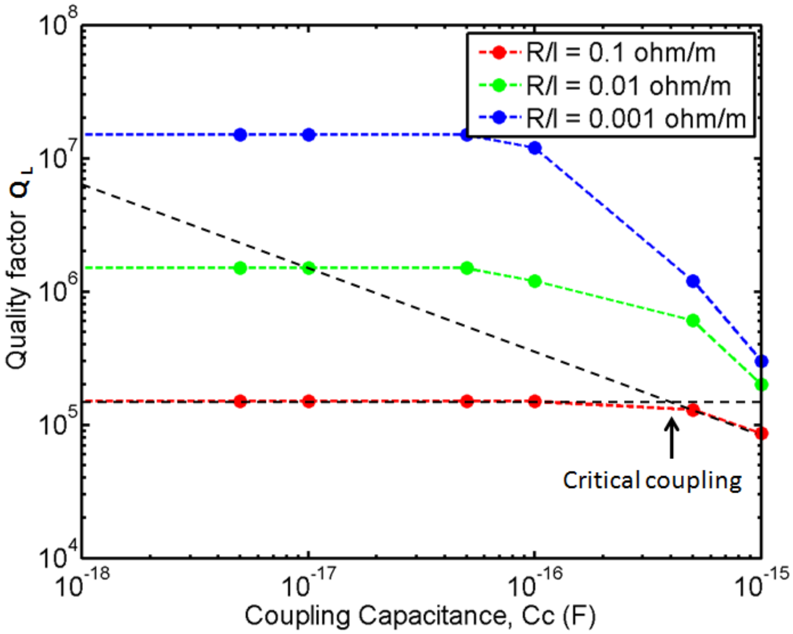

Figure 3.4: The effect of C_c on the loaded quality factor, Q_L of a single resonator. The black dashed lines show the limiting cases of over- and under-coupling. At a critical value of C_c (for example, $\sim 4 \times 10^{-16}$ F for R/l= 0.1 Ω/m) there is optimum coupling of signal between the resonator and the transmission line.

transmission lines were used. As in section 3.1.2, the resonators were simulated as two transmission lines with identical parameters listed in table 3.1 The microwave drive signal generated by the network analyser (NA) is denoted as V_{in} and Z_{out} is the 50 Ω impedance at its output port. The signal is carried by 50 Ω transmission lines and coaxial cables and to the resonators. There is symmetric coupling of the microwave signal into and out of the resonators through a coupling capacitance C_c. The resonators themselves are coupled by a weak coupling capacitance, C_k. The transmitted signal is then carried by 50 Ω transmission lines and coaxial cables to the input port of the NA, which has an input impedance, $Z_{in} = 50$ Ω. The transmitted signal, V_{out} is measured across Z_{in}.

The C_k was calculated for a range of overlap lengths as described in section 3.1.1 and its effect on the coupled resonator frequencies was studied. The splitting in the coupled resonator frequencies as a function of C_k is shown in fig. 3.6.

The values of coupling capacitances obtained from the simulations were used as a guide to design a range of coupled resonator circuits as explained in section 3.1.4.

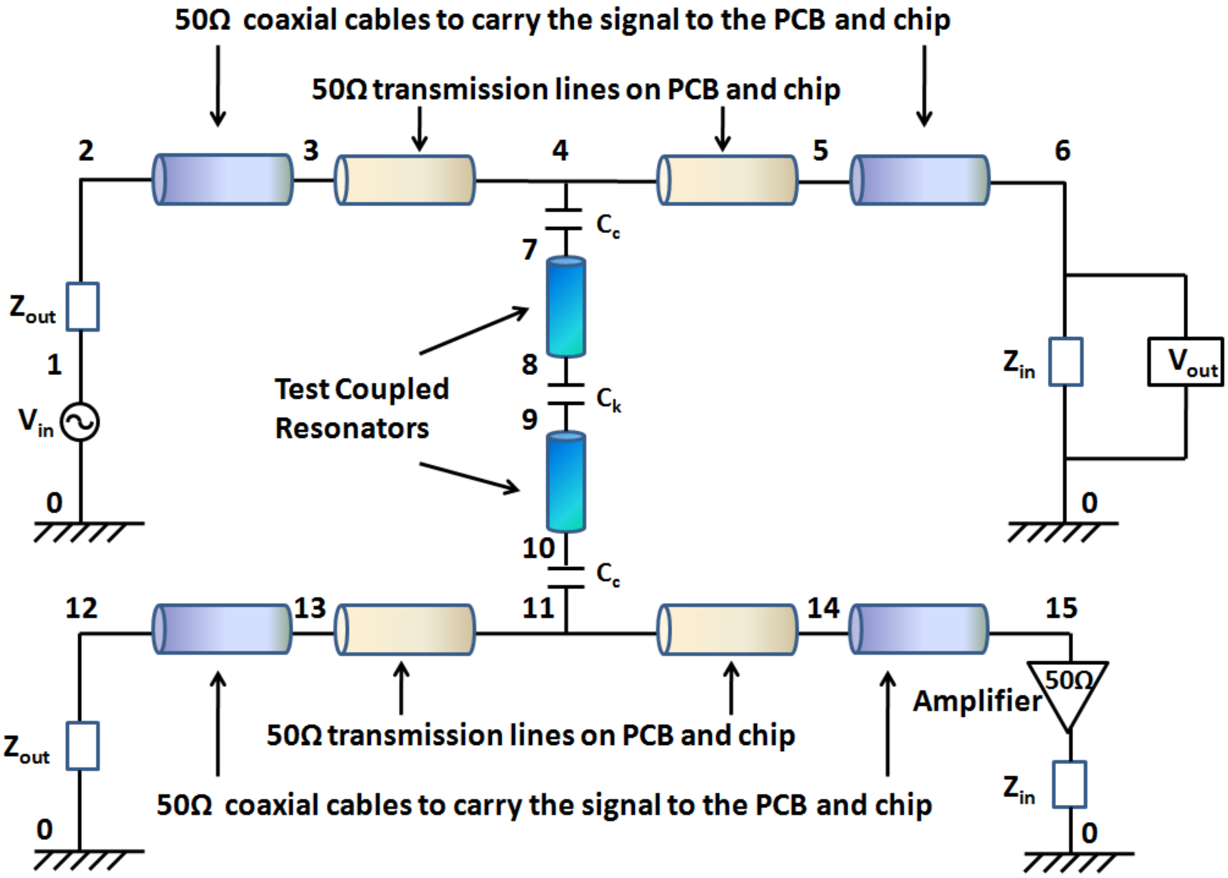

Figure 3.5: Coupled resonators circuit that was simulated in AIM Spice.

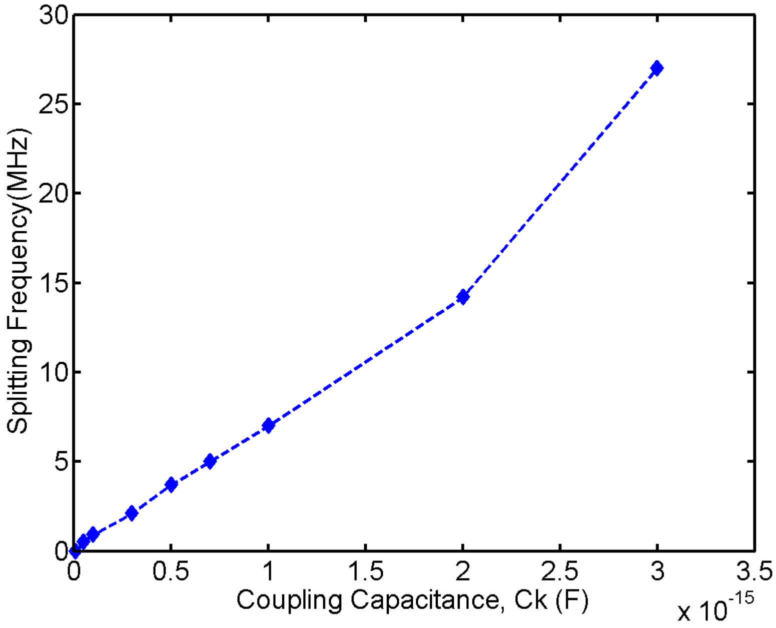

Figure 3.6: Simulated data: variation of splitting in the coupled resonator frequencies with C_k. The splitting $\rightarrow 0$ as $C_k \rightarrow 0$. This data was computed for a fixed value of $C_c \approx 4 \times 10^{-16}$ F.

3.1.4 Design variations of coupled resonator circuits

The geometry of a coupled resonators device, adapted from [4] and used in the experiments, is shown in fig. 3.7. The whole geometry covers an area of 9×4 mm^2 so that it can be patterned on the 10×5 mm^2 chip. Each resonator occupies an area of 1.6×1.1 mm^2. There is a symmetric coupling of the input and output signals from the resonators to the transmission lines by a capacitance C_c, formed by the overlap of centre tracks of the resonators and the transmission lines. The resonators are weakly coupled by a capacitance, $C_k \ll C_c$, and once again determined by the overlap length of their corresponding centre tracks.

Each resonator is ≈ 10 mm long, which results in a half wavelength fundamental frequency of 6 GHz. The meander in the resonators is to accommodate their lengths within the available space on the chip and this has negligible effect the resonant frequencies [57]. In our designs, the distance between adjacent meanders is designed to be 100 μm. The centre tracks of the resonators as well as the transmission lines are 10 μm wide with a separation of 5 μm from the adjacent ground planes, thereby maintaining a 50 Ω impedance along their lengths to prevent reflections of the microwave signal from the measurement electronics.

A series of coupled resonator circuits were designed in the geometry shown in fig. 3.7 with variations in C_c and C_k, which enabled measurement of a wide range of splitting in the coupled resonator frequencies. The resonator parameters for circuits that were patterned and measured in this geometry are listed in table 3.2.

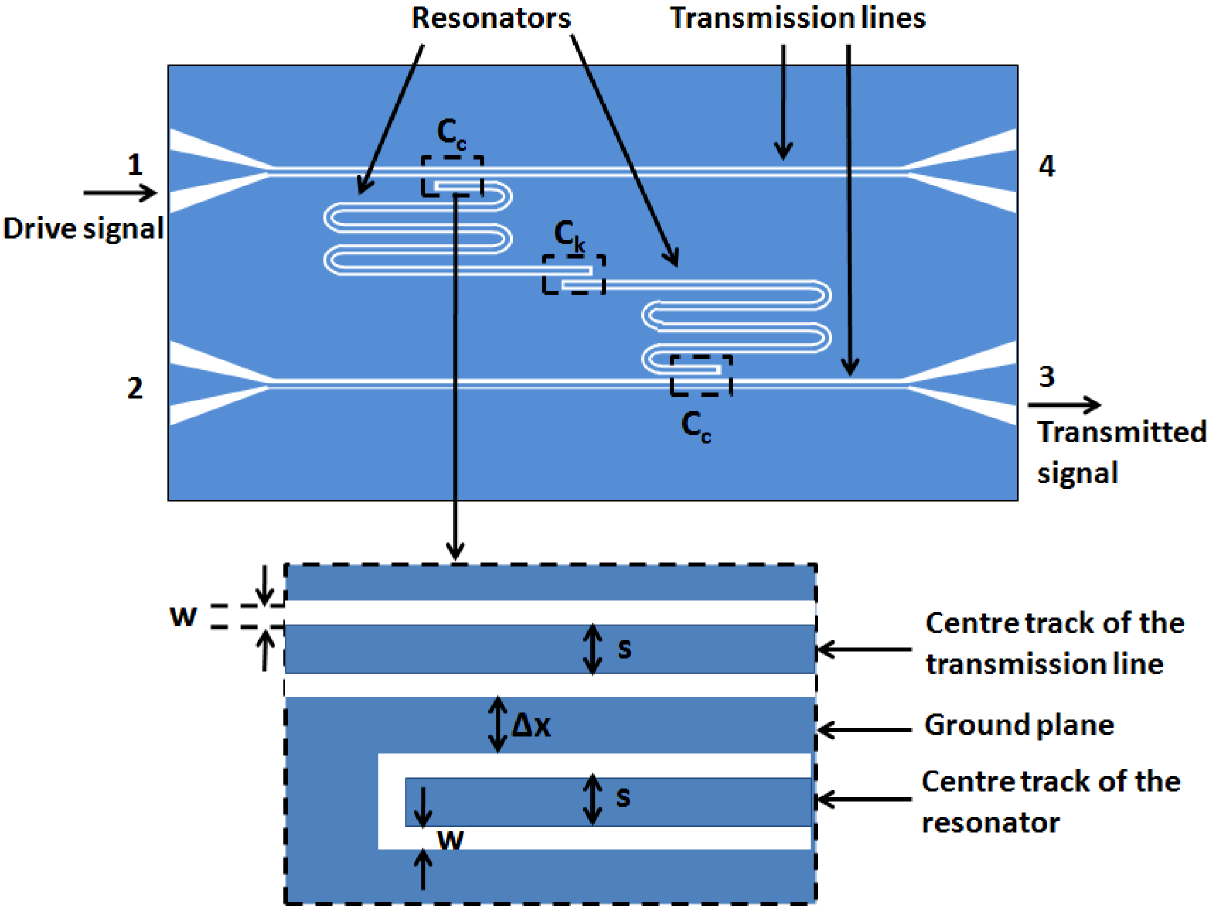

Figure 3.7: Geometry A: Design of a system of two identical coupled resonators. Blue regions in the figure represent the metal layer(niobium) and white regions represent the bare dielectric substrate. The microwave drive and transmitted signals are coupled into and out of the resonators by coupling capacitances C_c formed by the overlap of the resonator and transmission line centre tracks. The resonators are coupled to each other by a coupling capacitance C_k, in the overlap region of the centre tracks of the resonators. In all the designs, the width of the centre tracks, $s = 10\ \mu$m and the distance from the adjacent ground planes, $w = 5\ \mu$m. The width of the ground plane between the overlapping centre tracks is Δx, and was made 10 μm wide in all the designs.

It is fairly clear for overlap geometries in fig. 3.7 that the values of C_c and C_k determined from the 2d simulations in COMSOL are not accurate, but do suffice for the initial measurements.

Geometry	$L_c(\mu\text{m})$	$C_c(\text{F})$	$\Delta x\ (C_k)(\mu\text{m})$	$L_k(\mu\text{m})$	$C_k(\text{F})$	Sample Label
A	57	4×10^{-16}	10	430	3×10^{-15}	1
				143	1×10^{-15}	2
				14	1×10^{-16}	3
				1	1×10^{-17}	4

Table 3.2: This table lists the first set of coupled resonator devices that were patterned and measured at low temperatures. All the resonators were designed to be ≈ 11mm long.

3.1.5 Mask designs to enable fabrication of nanobars

To implement the proposed theoretical models in [4], coupled resonator circuits were designed to enable the fabrication of nanobars, which could be coupled to the microwave resonators in two ways as shown in figs. 3.8 and 3.9. In the first case, the nanobar is directly coupled to only one of the resonators. The second case involves coupling it simultaneously to both the resonators by siting it in the centre of the structure. To implement the second case, an additional centre track was incorporated to enable possible coupling of the low frequency drive signal to the nanobar as shown in fig. 3.9. In fig. 3.8, the nanobar is driven by coupling a low frequency signal from the same transmission line that is used to drive the microwave resonators, as implemented by Lehnert *et al* in [11].

To achieve maximum changes in the resonant frequencies, the nanobar is placed near the voltage anti-node of the microwave cavity [11]. Also, greater coupling could be achieved by having longer nanobars which have the advantage of bigger oscillations within their elastic limits. Although, the disadvantages of long nanobars are that they tend to buckle easily as well as have the risk of causing short circuits to the ground plane. Hence, for the initial experiments, the length of the nanobar was chosen as $\approx 20\ \mu$m, which would result in a fundamental frequency of ≈ 7.5 MHz.

The resonator circuits in geometry A with C_k that resulted in a splitting of < 10 MHz in the coupled resonator frequencies were modified to allow for the fabrication of nanobars in the geometries illustrated in figs. 3.8 and 3.9.

3.2 Sample Preparation

All the resonator samples were fabricated on 200 nm thin film niobium deposited on oxidized, high resistivity, silicon substrates. A niobium on silicon wafer, diced into $5 \times 10\ \text{mm}^2$ chips was purchased from a commercial

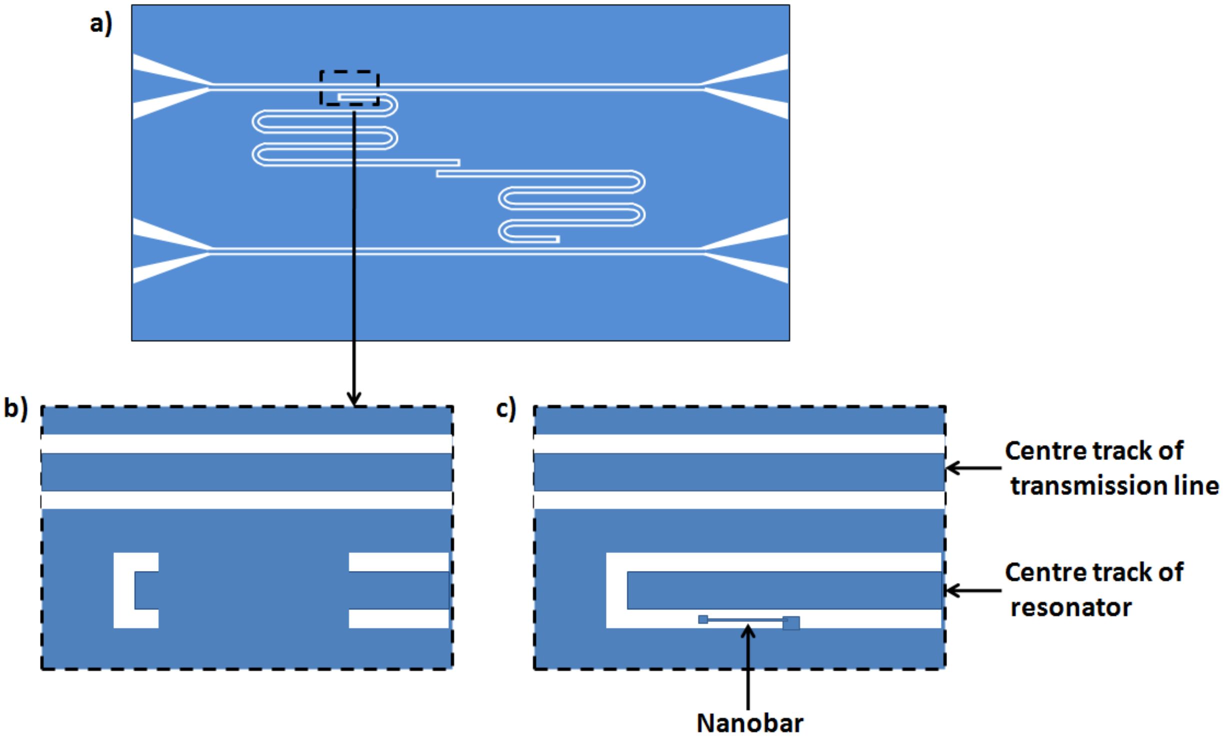

Figure 3.8: (a) is the repetition of the coupled resonator geometry shown in fig. 3.7. (b) Geometry B: Modified version of (a) that enables the fabrication of a nanobar as shown in (c). Here, the nanobar is directly coupled to only one of the microwave resonators.

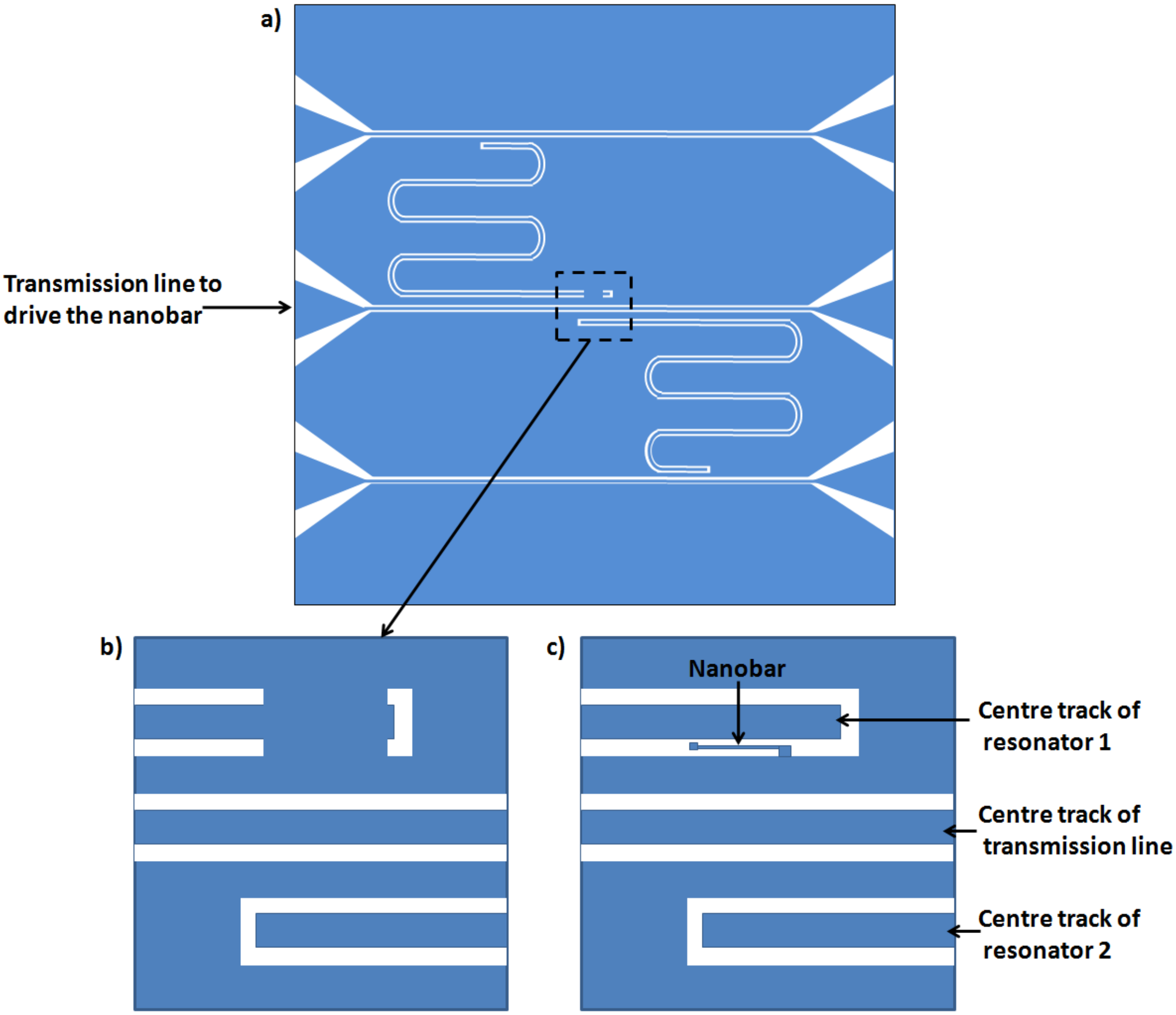

Figure 3.9: (a) Geometry C: Coupling of a nanobar directly to both the resonators. This geometry was meant to be patterned on a 10×10 mm^2 chip. An additional transmission line was included in the circuit to drive the nanobar. (b) Shows the region within the dashed rectangle in (a) which results in a structure (c) where the nanobar is to be fabricated.

organization Star Cryo, Ltd. The resonator patterns were fabricated on the chips using photo-lithographic methods. As described in the previous section, a chrome mask consisting of various resonator designs was manufactured for this purpose. The procedure used for the fabrication of resonator circuits on the niobium chips will be described in this section.

Initially, the samples needed to be cleaned thoroughly. This was done in an ultrasonic bath using acetone as one of the cleansers. This step ensured that any large particles that adhered to the metal surface were removed. The samples were further cleaned with iso-propyl alcohol in an ultrasonic bath, which eliminated any remaining impurities. The samples were then dried by gently blowing with a nitrogen gun and examined under an optical microscope. When the metal surfaces were devoid of impurities, conventional lithographic methods were used to fabricate resonator devices on them. The steps involved in this process are illustrated in figure 3.10.

Once a sample was cleaned with acetone and iso-propyl alcohol, it was pre-baked on a hot plate at 110° C for 300 s to remove any moisture on the metal surface. This step improved the adhesion of photoresist to the metal surface : poor adhesion could cause small resonator features to lift off from the surface in the process of developing the sample. The next step was to deposit photoresist on the sample surface. This was done with a spin coater, which spun the resist on the sample for ~ 45 s at a rate of 5500 rpm. The sample was then post-baked on a hot plate at 110° C for 60 s so that any excess solvent from the photoresist would vapourize prior to UV light exposure. A positive photoresist, AZ 5214E was used, for which the exposed regions of resist was easily washed away with the developer.

The process of spinning photoresist on the sample resulted in a thicker layer along its edges, thus forming an edge-bead. The excess resist along the edges prevented good contact of the photomask with the sample during UV exposure, which resulted in poorly defined edge profiles of resonator structures. Hence, prior to exposure of the resonator patterns, the excess resist from the sample edges was removed with an edge-bead mask.

A mask aligner (Karl Suss MJB3) was used in the contact mode to align the mask with the sample, such that there was good contact between the two. The sample was exposed to UV light and then developed, after which, the photoresist remained on unexposed regions of the sample. The exposure time used to remove the edge bead was 60 s and the developing time was 90 s. In order to pattern a resonator circuit, an exposure time of 7s and a developing time of ~ 30 s were used on all samples. The photoresist was developed using AZ726 MIF developer, followed by a rinse in de-ionised water. The samples were closely examined under an optical microscope to check the edge quality of the resonator structures as well as for short circuits before

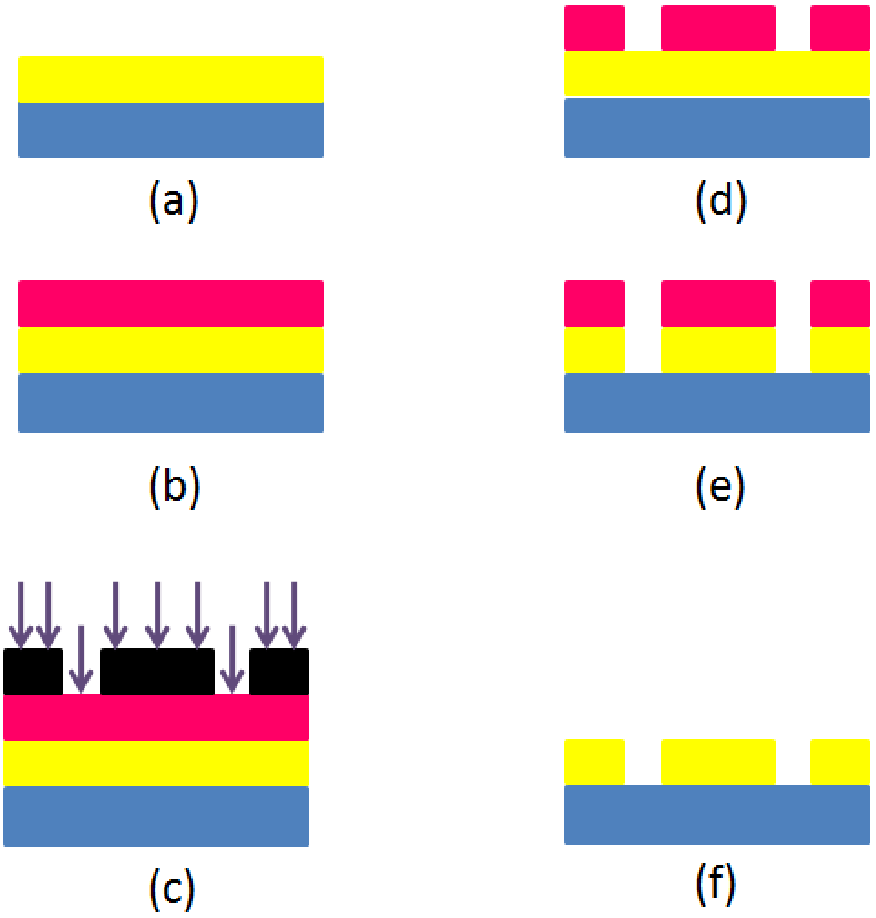

Figure 3.10: These were the steps involved in photo lithography. (a)A clean sample of niobium(yellow) on silicon(blue). (b)Photoresist(pink) deposited on Niobium. (c)A resonator pattern on the mask(black) brought in contact with the sample and exposed to UV light. (d)Exposed regions of photo-resist washed away in the developer. (e)Etching of unwanted metal. (f)The desired resonator circuit patterned on niobium.

they were etched.

The unwanted metal from the samples was then etched away using an Oxford Applied Research IM150 argon ion beam miller. To achieve uniform etching, the sample stage in the vacuum chamber was set at an angle of 45° and rotated during the process [73]. A milling time of 35 minutes was sufficient for the metal to be etched. The photoresist was then removed from the samples using acetone.

Thus, all the resonator circuits used for this project were patterned by following the above procedure. In the next section, the method used to mount the resonator samples on the cryostat will be described.

3.3 Sample Mounting

Measurement of the resonator properties was achieved by first gluing the sample with OptiClean (a camera lens cleaner), to a commercial dielectric PCB clad on both sides with 17.5 μm thick copper foil and patterned as shown in fig. 3.11 with six coplanar transmission lines, to enable measurement of resonator devices in all the geometries shown in figs. 3.7, 3.8 and 3.9. The transmission lines have the same ratio of centre track to gap width as those on the resonator chip and provide a 50 Ω impedance.

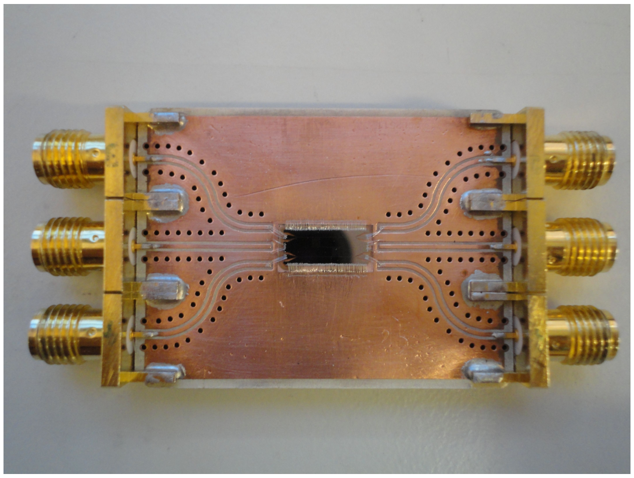

Figure 3.11: The picture shows a resonator sample glued and wirebonded to the PCB. The PCB was patterned on an RT Duroid 6010LM board with dimensions of 40 mm×30 mm×2.54 mm.

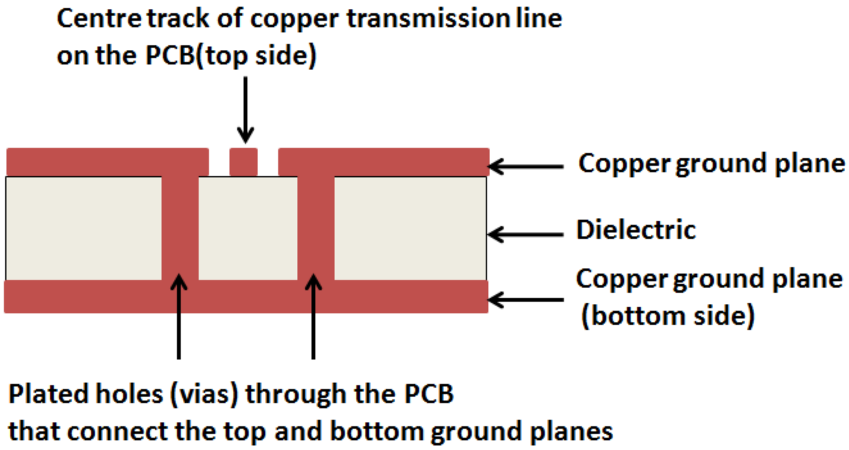

Figure 3.12: A schematic representation of the vias near the centre track of the transmission line

The centre tracks and ground plane of the PCB are connected to the respective parts of the chip with multiple aluminium wire bonds and to the SMA connectors with solder. SMA connectors were used to connect the measurement circuitry to the PCB. To reduce parasitic coupling within the chip, the length of the wirebonds were made as short as possible and the bond spacing, uniform and minimal [74, 75]. Copper plated vias along the length of the transmission lines were drilled to make electrical contact between the top and the bottom ground planes, as well as to inhibit propagation of microwaves within the PCB, thus minimizing parasitic capacitive coupling on the PCB.

The PCB was enclosed in a closely fitting copper cavity and mounted on the cryostat as shown in fig. 3.13. The copper cavity prevents microwave radiation losses and provides mechanical support.

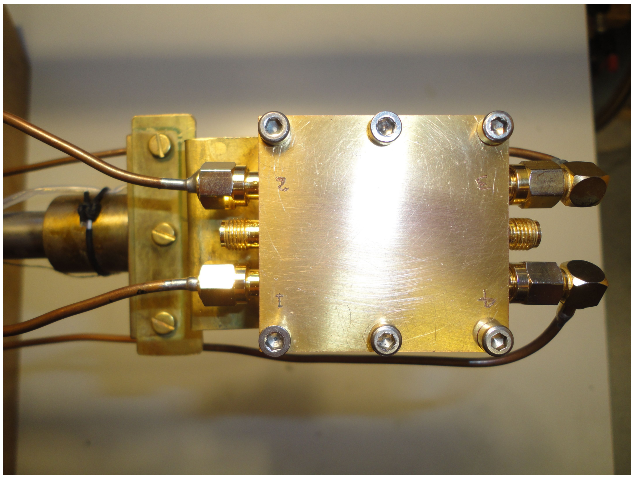

Figure 3.13: The PCB and sample system placed in a gold coated copper cavity and then mounted on the cryostat

3.3.1 Schematic representation of the measurement system

The copper cavity was connected to the bottom of a conventional metal cryostat as shown schematically in fig. 3.14. The experimental set-up consisted of a cryostat which was cooled to ~ 1.4 K by pumping on the liquid Helium bath, thus reaching well below the superconducting critical temperature of the niobium film. The temperature inside the cryostat was determined from a pressure gauge that was fitted to it.

A microwave signal from the network analyser was sent through a semi-flexible coaxial cable connected to the top plate SMA connector on the cryostat. From this point, the signal was sent down the cryostat by a low thermal conductivity coaxial cable and fed to the copper cavity via the SMA connectors shown in fig. 3.13. The signal from the resonator sample was sent up the cryostat through another low thermal conductivity coaxial cable, was then amplified and sent back to the network analyser. Further details on the modes of measurement on the network analyser are described in section 3.3.2.

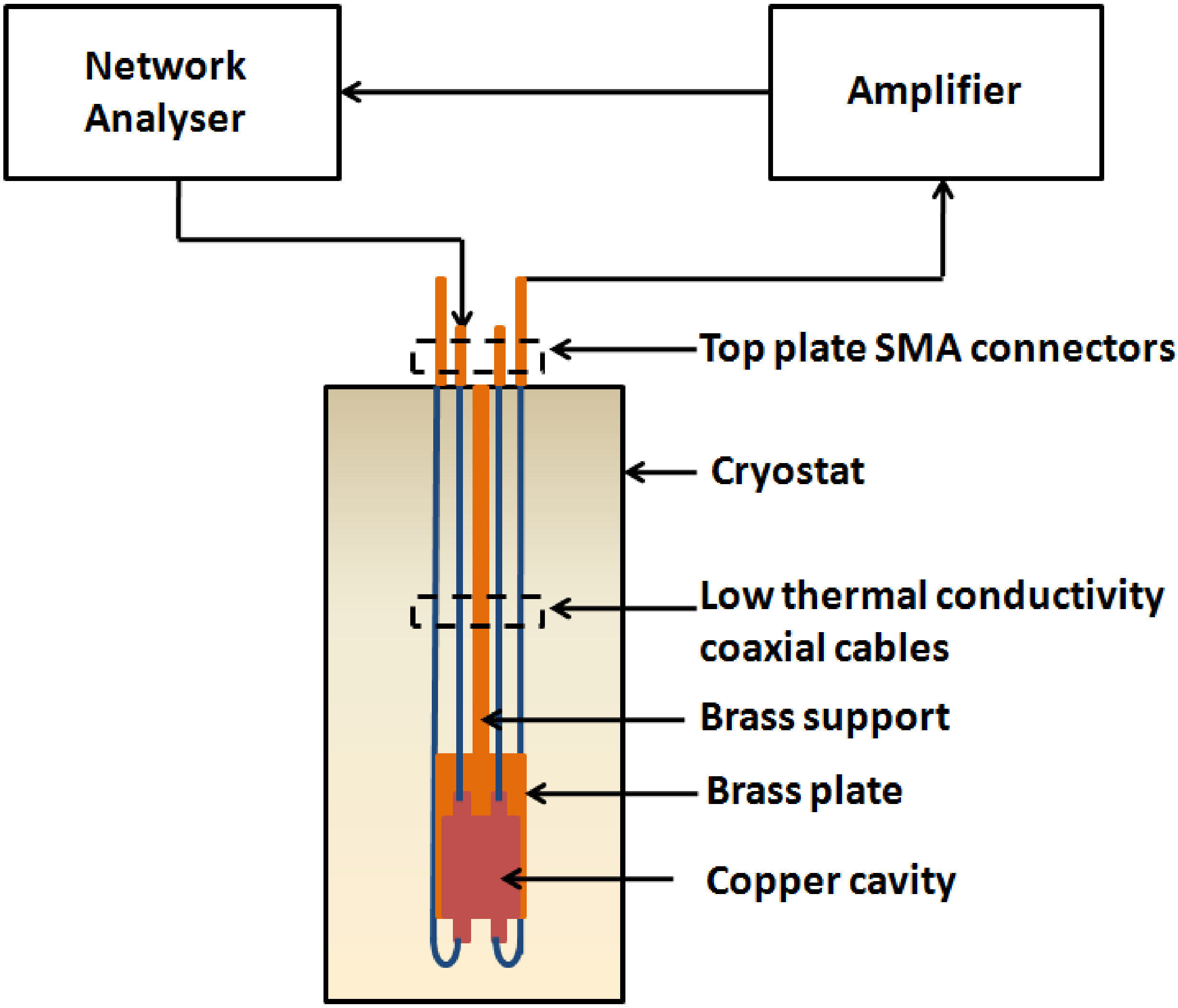

Figure 3.14: Schematic of the low temperature microwave apparatus

3.3.2 Microwave measurements on the network analyser

The HP 8720D is a commercial 2-port device which can be operated in either transmission or reflection mode. It generates a microwave signal at one port and, in transmission mode, detects and processes the signal at the other port. Alternatively, in reflection mode, it detects and processes the signal at the same port. The measurement S parameters are defined in table 3.3. The S parameters can be displayed on the network analyser in a variety of formats. The ones used in this thesis were as a magnitude or, more frequently, as log (magnitude).

Signal Source Port	Signal Detection Port	S-Parameter
1	1	S11
2	2	S22
1	2	S21
2	1	S12

Table 3.3: Data was recorded in terms of the above defined S-parameters for a 2-port measurement system.

It should be noted that the experimental system described in this chapter is a 6 port one as shown in fig. 3.11 and the nomenclature S43, for example, implies that the signal source from the NA is connected to port 3 and the detected signal is from port 4.

3.4 Results and discussion of measurements on coupled resonator devices

The experimental methods described in sections 3.2, 3.3 and 3.3.1 were employed to fabricate and measure samples $1-4$ (details listed in table 3.2) at 1.4 K. All the samples were of the geometry illustrated in fig. 3.7. The measured transmission(S24) and reflection (S23) data for sample 1 are shown in figs. 3.15 and 3.16 respectively.

Peaks at both the fundamental frequencies with a separation of $\approx$ 53 MHz were observed in the S24 data, although the symmetric (lower frequency) and antisymmetric (upper frequency) peaks were not of the same magnitude. The peak shapes deviated from the expected Lorentzian and simple analysis of the data showed that this distortion was due to crosstalk or additional transmission between the input and output measurement ports on the chip and PCB. Depending on the magnitude and phase of the crosstalk, the resulting signal could be dominantly a peak, or a dip, or, as seen in fig. 3.15, a combination of the two. To determine the resonant frequencies and the quality factors accurately, the data was fitted by a combination of a Lorentzian and a crosstalk signal. Details of the fitting method are given in appendix B.1.

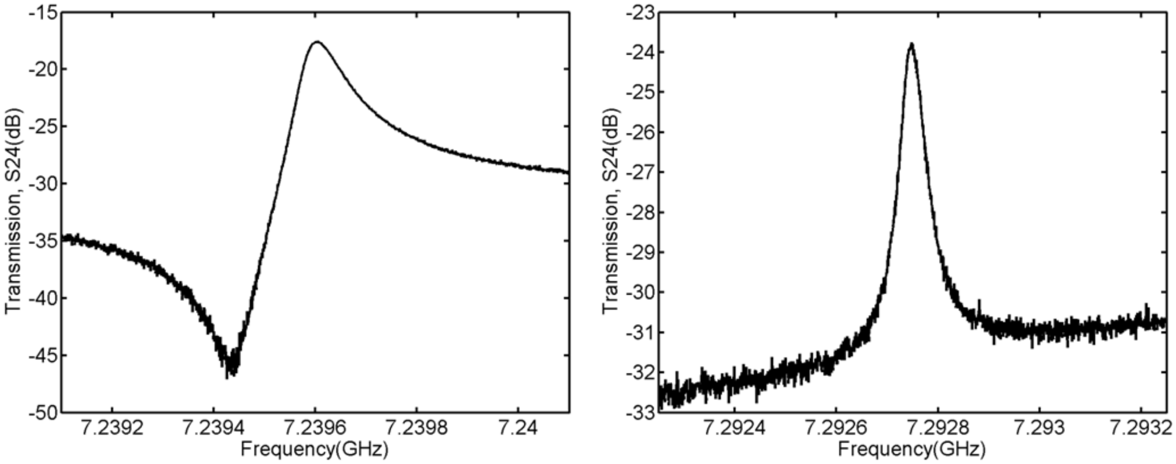

(a) Lower frequency **(b) Higher frequency**

Figure 3.15: Measured data: Peaks in the transmission spectrum at the lower and higher fundamental frequencies ((a) and (b) respectively) in sample 1. The quality factors for the lower and higher frequency peaks were 1×10^5 and 1.5×10^5 respectively.

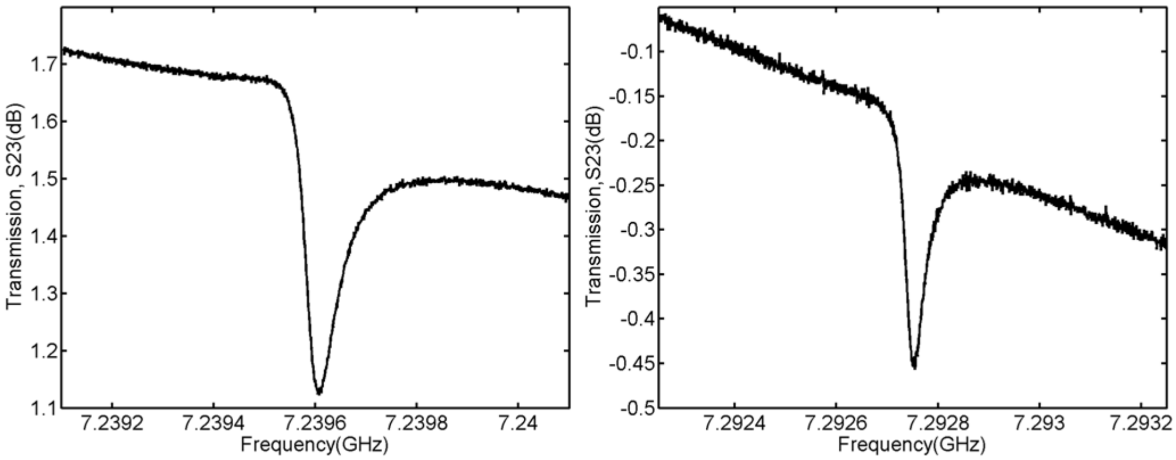

(a) Lower frequency **(b) Higher frequency**

Figure 3.16: Measured data: Dips in the reflection spectrum at the lower and higher fundamental frequencies ((a) and (b) respectively) in sample 1.

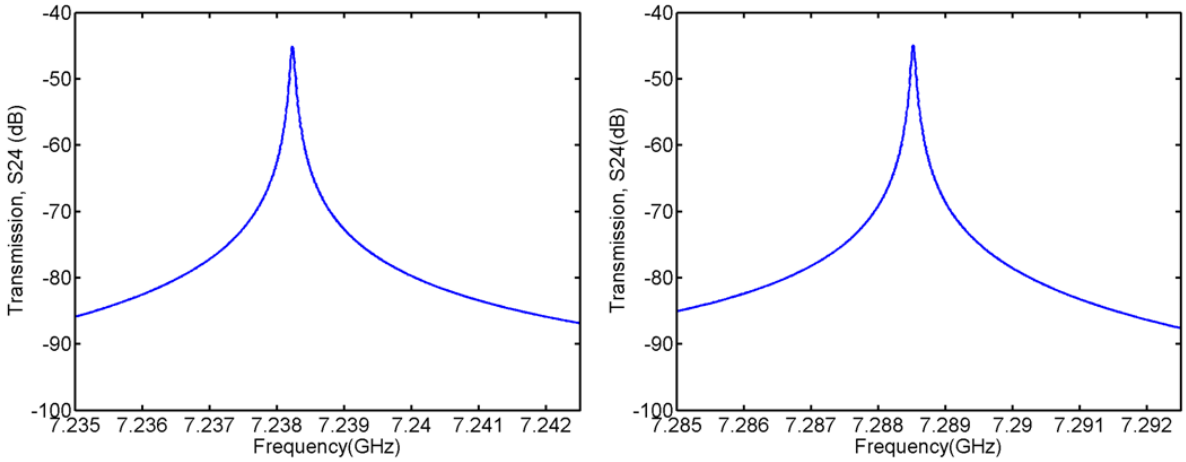

(a) Lower frequency

(b) Higher frequency

Figure 3.17: Simulated transmission data for sample 1 obtained by incorporating the values listed in table 3.4 into the AIM Spice circuit in fig. 3.5. (a) and (b) show the peaks at the lower and higher frequencies respectively.

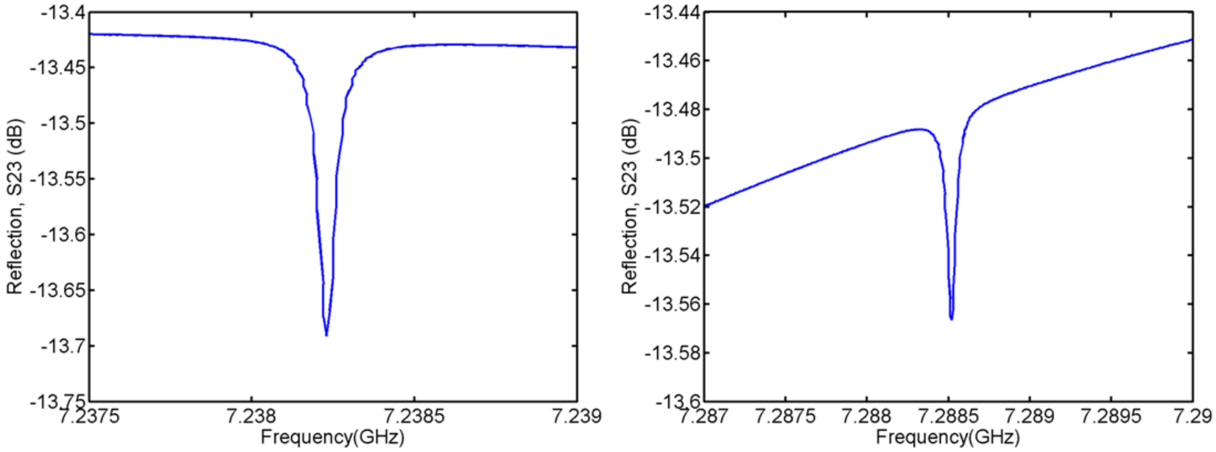

(a) Lower frequency

(b) Higher frequency

Figure 3.18: Simulated reflection data for sample 1 obtained by incorporating the values listed in table 3.4 into the AIM Spice circuit in fig. 3.5. (a) and (b) show the dips at the lower and higher frequencies respectively.

To predict the behaviour of the resonators on this sample (1), simulations were performed in AIM Spice using the circuit in fig. 3.5. The key parameters used for the simulation are listed in table 3.4 and the theoretical S24 and S23 data is shown in figs. 3.17 and 3.18 respectively. In the simulations, the measured values of attenuation in the coaxial cables and the transmission lines, together with coupling capacitances calculated in COMSOL were used. The resonator lengths were decreased by $\approx$ 16% from the originally designed values to match with the measured frequencies at 7.2395 GHz and 7.2927 GHz and the resistance per unit length was varied to match with the measured quality factors. The resonators were designed to have identical lengths, but the simulations required a difference in their lengths to be ≈ 30 μm to match with the measured splitting in the frequencies and the asymmetric peaks/dips. The overlap length of the resonator centre tracks was designed to obtain $C_k = 3 \times 10^{-15}$ F and therefore a splitting of $\approx$ 22 MHz in the frequencies. But to match with the measured splitting of $\approx$ 53 MHz, C_k was increased by 40%. The value of C_c was increased by 40%, but the absolute magnitudes of the peaks, dips and the background level could not be matched to the measured values. The originally designed values and the adjusted values incorporated into the simulations to match with the measured frequencies and splitting are provided in table 3.4.

Simulation Parameter	Fitted Value	Designed value
Length of resonator 1, l_1	0.8335×10^{-2} m	1×10^{-2} m
Length of resonator 2, l_2	0.8305×10^{-2} m	1×10^{-2} m
R/l of resonator 1	0.18 Ω/m	Variable parameter
R/l of resonator 2	0.10 Ω/m	Variable parameter
L/l of both resonators	4×10^{-7} H/m	4×10^{-7} H/m
C/l of both resonators	1.7×10^{-10} F/m	1.7×10^{-10} F/m
C_c	5.6×10^{-16} F	4×10^{-16} F
C_k	4.2×10^{-15} F	3×10^{-15} F

Table 3.4: Simulation parameters in AIM Spice for sample 1.

It was seen that although the broad features of the coupled resonator behaviour were reproduced, the details were not, and in particular, the absolute values of frequencies and their separation, the absolute peak/dip magnitudes and the high background levels which could be ascribed to the presence of cross talk between multiple ports on the chip and PCB [74, 76–78]. Attempts were made to include leaky capacitive paths within the simulation circuit in fig. 3.5 which might have caused shifts in the resonant frequencies but large variations could not be accounted for in the AIM Spice simulations.

It was clear that the experimental system was far from the avoided crossing, implying that the two resonators were of substantially different frequencies. This could, in principle, arise from different resonator lengths, but the observed splitting would require a length difference of 30 μm (as shown by the Spice simulations), compared with the patterning accuracy which is ± 2 μm. Simulations in COMSOL [71] showed that a high dielectric constant (≈ 3) layer of impurities on the sample surface could cause this effect (of shift in frequencies, as shown in fig. 3.19), but only if it were 10 μm thicker on one resonator than the other.

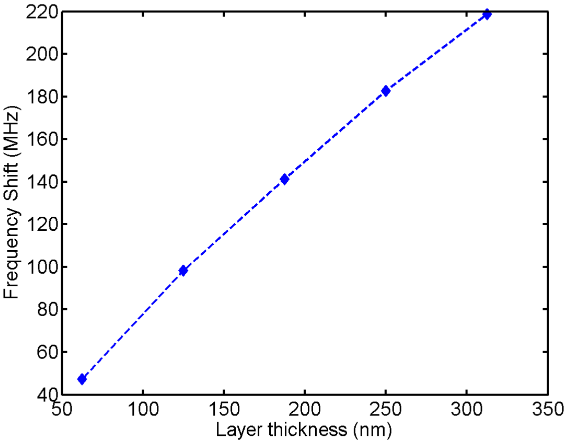

Figure 3.19: Simulated frequency shift as a result of a thin dielectric layer ($\epsilon_r = 3$) deposited on one of the resonators.

COMSOL simulations of the inter-track capacitance of the coplanar transmission lines on the PCB showed them to be an order of magnitude higher than C_c, which indicated that the potential for crosstalk effects was substantial.

The samples $1 - 4$ listed in table 3.2 were all measured at 1.4 K and the observed and predicted values of the frequencies and their splitting are listed in table 3.5. The simulated splitting in the frequencies listed in this table were obtained by incorporating the originally designed values of lengths and coupling capacitances provided in table 3.2 into the simulation circuit in fig. 3.5. The measured frequencies were determined by fitting the measured S24 data to a complex Lorentzian function described in appendix B.1.

Sample Label	f_{lower}(GHz)	f_{higher}(GHz)	$\Delta f_{measured}$(MHz)	$\Delta f_{simulated}$(MHz)
1	7.2396	7.2927	53	22
2	7.0514	7.0794	28	7
3	6.9987	7.0015	2.8	2
4	7.0928	7.1122	19	0

Table 3.5: List of resonant frequencies, their simulated and measured splitting for decreasing values of C_k. For the listed samples, $C_c = 4 \times 10^{-16}$ F.

The purpose of the initial measurements on these samples was to study the splitting in the frequencies as a function of C_k and compare the measured values with the theoretical predictions in Spice. The large deviations from the predicted values implied that the resonators on all the samples were far from the avoided crossing and were largely influenced by cross talk on the chip and PCB. The differences between the measured and predicted values were much greater than could be accounted for by computational accuracy, apart from other reasons stated earlier (such as a dielectric layer deposited on the resonators, a tilt in the sample due to uneven thickness of the glue, etc). Hence it was decided that the resonator circuits, the copper PCB and the cavity would be re-designed in order to reduce crosstalk. The presence of crosstalk and its high background level is undesirable because it prevents the observation of small peaks/dips. In the next chapter, an improvement in the measurements achieved with the new resonator designs, PCB and the copper cavity are described.

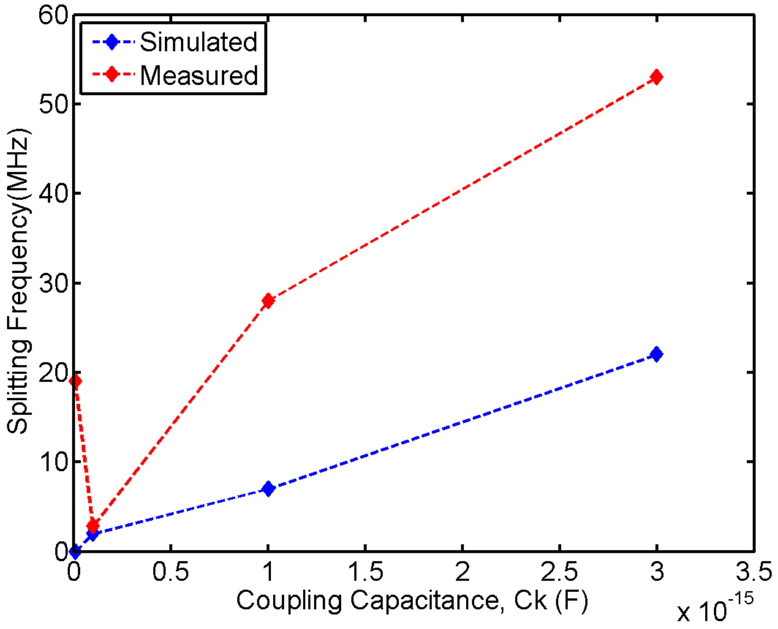

Figure 3.20: A comparison of the measured and predicted splitting as a function of C_k for samples $1 - 4$.

CHAPTER 4

COUPLED RESONATORS II : DESIGN AND MEASUREMENTS

The possible reasons for large deviations in resonant frequencies of the first set of coupled resonator devices were explained in chapter 3. Modifications were made in the resonator structures to minimize stray capacitive coupling between multiple, on-chip transmission lines. The sample housing that comprised the copper PCB and cavity was redesigned so that the coupling of microwaves between the input and output measurement ports (crosstalk) was reduced.

In this chapter, the simulations in AIM Spice that guided the design of new coupled resonator circuits are described. Then, the variations incorporated in the geometries of coupled resonator circuits to enable measurements on a wide range of devices are illustrated. An improvement in the microwave background level with the new sample housing is shown. Finally, the results from low temperature measurements on new coupled resonator devices are presented and discussed.

4.1 Design considerations

The new coupled resonator geometry to be used for the experiments is shown in fig. 4.3 and it differs from the old geometry in fig. 3.7 in that multiple input and output ports on the resonator chip are absent. The resonator parameters such as its length (l), inductance per unit length (L/l) and capacitance per unit length (C/l) were the same as used in the previous designs in chapter 3. Since it was seen in section 3.4 that the values of coupling capacitances were increased by $\approx 40\%$ to match with the measured splitting in the frequencies, it was decided that the accuracy of their computation may have to be improved. Hence, the coupling capacitance per unit length was re-calculated in COMSOL [71] using a 3d geometry of the overlapping centre tracks. The C_c and C_k values were determined for various overlap lengths and used for further analysis of the resonator circuits. A comparison of the 2d and 3d calculations of coupling capacitances are shown in fig. 4.1. It can be seen from fig.4.1b that for small overlap lengths (< 15 μm), the 2d calculations underestimate the coupling between the overlapping centre tracks and the simulations in 3d give a more accurate estimate of the capacitance.

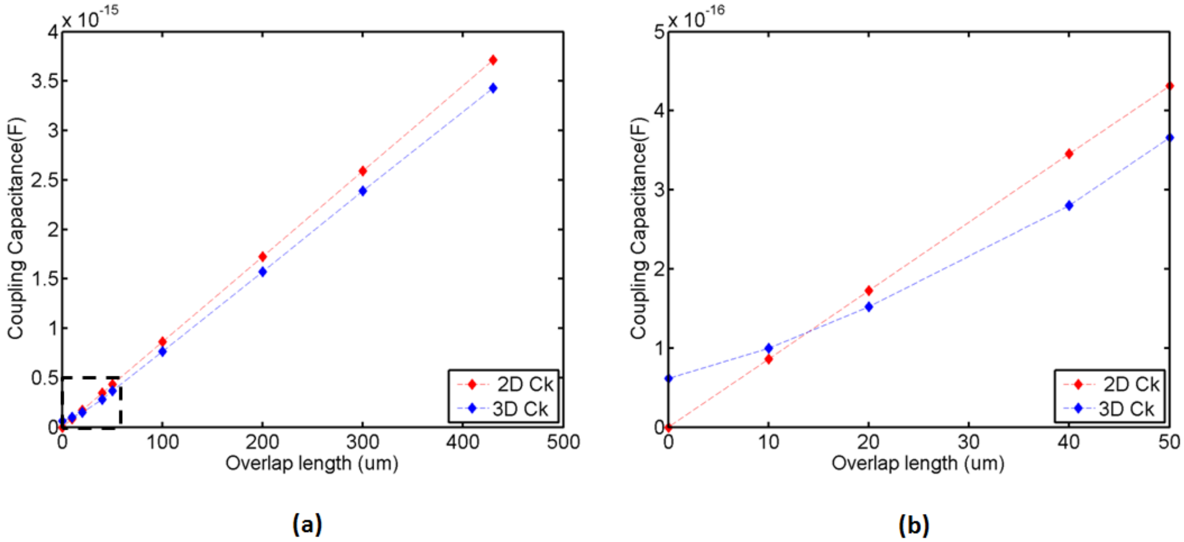

Figure 4.1: Comparison of the coupling capacitances calculated in two and three dimensional geometries of the overlap lengths. The data points within the dashed rectangle in (a) are expanded in (b).

Once again, simulations in AIM Spice guided the design and analysis of the new set of coupled resonator devices. Fig. 4.2 shows the circuit that was used to simulate the new resonator geometry and predict the splitting in the frequencies as a function of C_k. As in sections 3.1.2 and 3.1.3, the resonators were represented as transmission lines with specified parameters of l(m), L/l(H/m) and C/l(F/m). In the simulation circuit, the microwave signal V_{in} is generated by the network analyser (NA) and carried by 50 Ω coaxial cables and transmission lines matched to the output impedance, Z_{out} of the NA. The capacitance C_c between the transmission lines on the chip and the resonators enables coupling of the signal into and out of the resonators. The resonators are coupled to each other by a capacitance C_k. The transmitted signal is again carried by 50 Ω transmission lines and coaxial cables to the input port of the NA and is measured across the 50 Ω input impedance of the NA (Z_{in}).

Further details of the input parameters used in the simulations are explained in section 4.4, wherein the measured values from low temperature experiments on the resonator devices are compared with the predicted values from simulations.

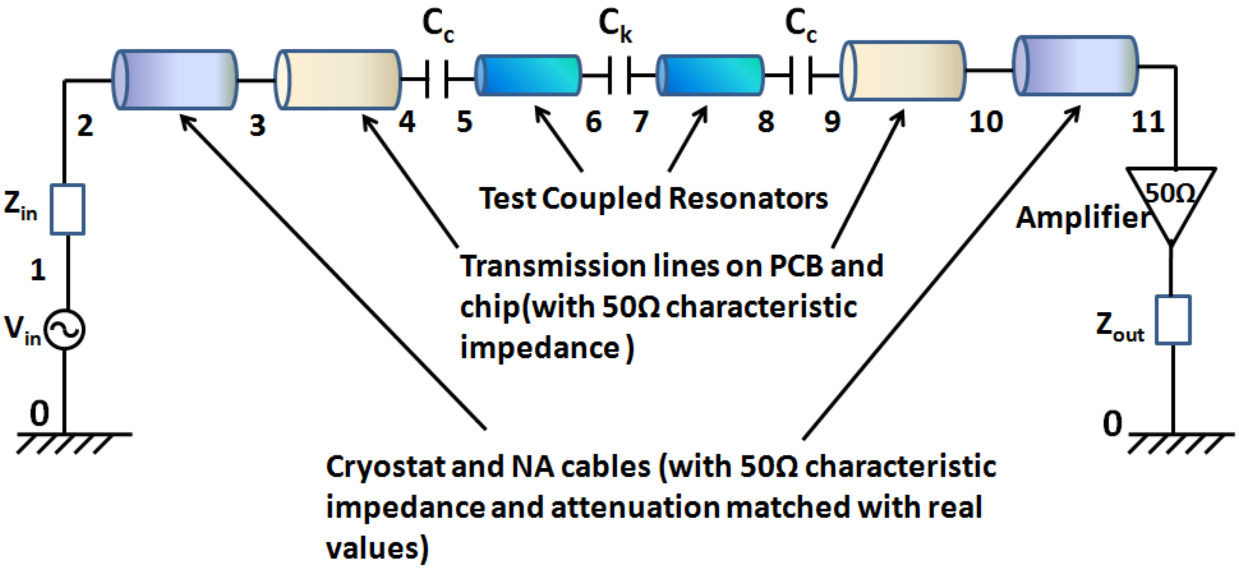

Figure 4.2: Simulation circuit to study a system of two identical, coupled, microwave resonators. Various nodes across which the voltage can be measured in the simulation process are labelled. Transmission and reflection of the signal from the resonators for example, is measured at ports 11 and 4 respectively.

4.2 Design of new coupled resonator circuits

In the following sections, the variations incorporated into coupled resonator circuit designs that would enable the measurement of a wide range of devices are described. Although a series of resonator circuits were designed to utilize optimum space on a 4″ photomask, subsequently, only a few of them were patterned and measured as listed in table 4.1.

4.2.1 Basic coupled resonators system

Figure 4.3 illustrates the design of two coplanar microwave resonators that are coupled by a weak capacitance. The whole geometry covers an area of 9×4 mm^2 so that it can be patterned on the 10×5 mm^2 chip. Each resonator occupies an area of 1.6×2 mm^2. There is symmetric coupling of the input and output microwave signals from the resonators to the transmission lines by a capacitance C_c, formed by the overlap of centre tracks of the resonators and the transmission lines. The resonators are weakly coupled by a capacitance, $C_k \ll C_c$, once again determined by the overlap length of their corresponding centre tracks.

Each resonator is ≈ 10 mm long, which results in a half wavelength fundamental frequency of 6 GHz. The meander in the resonators is to accommodate their lengths within the available space on the chip. It was reported in [74] that a minimum distance of 180 μm between adjacent meanders is required to inhibit parasitic coupling between them, hence in the new resonator designs, this distance was chosen to be 200 μm. The centre tracks of the resonators as well as the transmission lines are 10 μm wide with a separation of 5 μm from the adjacent ground planes, thereby maintaining a 50 Ω impedance along their lengths.

Based on simulations in AIM Spice, a series of coupled resonator circuits with varying C_k were designed so that the splitting between the two resonant frequencies as a function of C_k could be measured on the samples. Since one of the main goals of this project was to observe separations of the order of nanomechanical frequencies (< 10 MHz), circuits with small C_k were designed by either having short overlap lengths of the two resonators or by increasing the width of ground plane, Δx between the overlapping centre tracks of the resonators. Table 4.1 lists the resonator devices of the geometry in fig. 4.3 that were patterned and measured at low temperatures.

4.2.2 Coupled resonators geometry to allow for magnetic field tuning

The purpose of initial measurements on coupled resonator devices was to observe an avoided crossing of the frequencies when both the resonators have exactly the same resonant frequency. The frequencies are very sensitive to the resonator lengths and due to limitations in the fabrication process, there could be a variation of ± 2 μm in their lengths which could cause a frequency shift of the order of a MHz. This could result in the system being slightly away from the avoided crossing. For the values of C_k used in these designs, it was not possible to predict the frequency separation (Δf) very accurately prior to low temperature measurements on the samples, and therefore a method was devised to enable *in situ* tuning of the frequency of one of the resonators to be the same as that of the other. In references [62, 79], experimental work on magnetic field tuning of superconducting (niobium) resonators showed that a 0.1 mT dc field, applied perpendicular to the plane of a coplanar resonator lowered its resonance frequency by 1 MHz without introducing non-linearities in the resonant peaks.

Therefore, if the two resonant frequencies of any of our devices were less than 1 MHz apart, magnetic field tuning could be used to attain the crossing position in the frequencies. In the devices where the separation of the frequencies was greater than 1 MHz, another tuning mechanism with a wider frequency tuning range would have to be used (as described in chapter 5).

In the geometry illustrated in fig. 4.3, it is not possible for significant magnetic flux to penetrate into the resonators due to the shielding effect of the superconducting ground plane. Hence the resonator structures in geometry D were modified to enable flux penetration as shown in fig. 4.4. Narrow passages, that could be opened to the edge of the ground plane and let the magnetic flux in were made in the ground planes close to

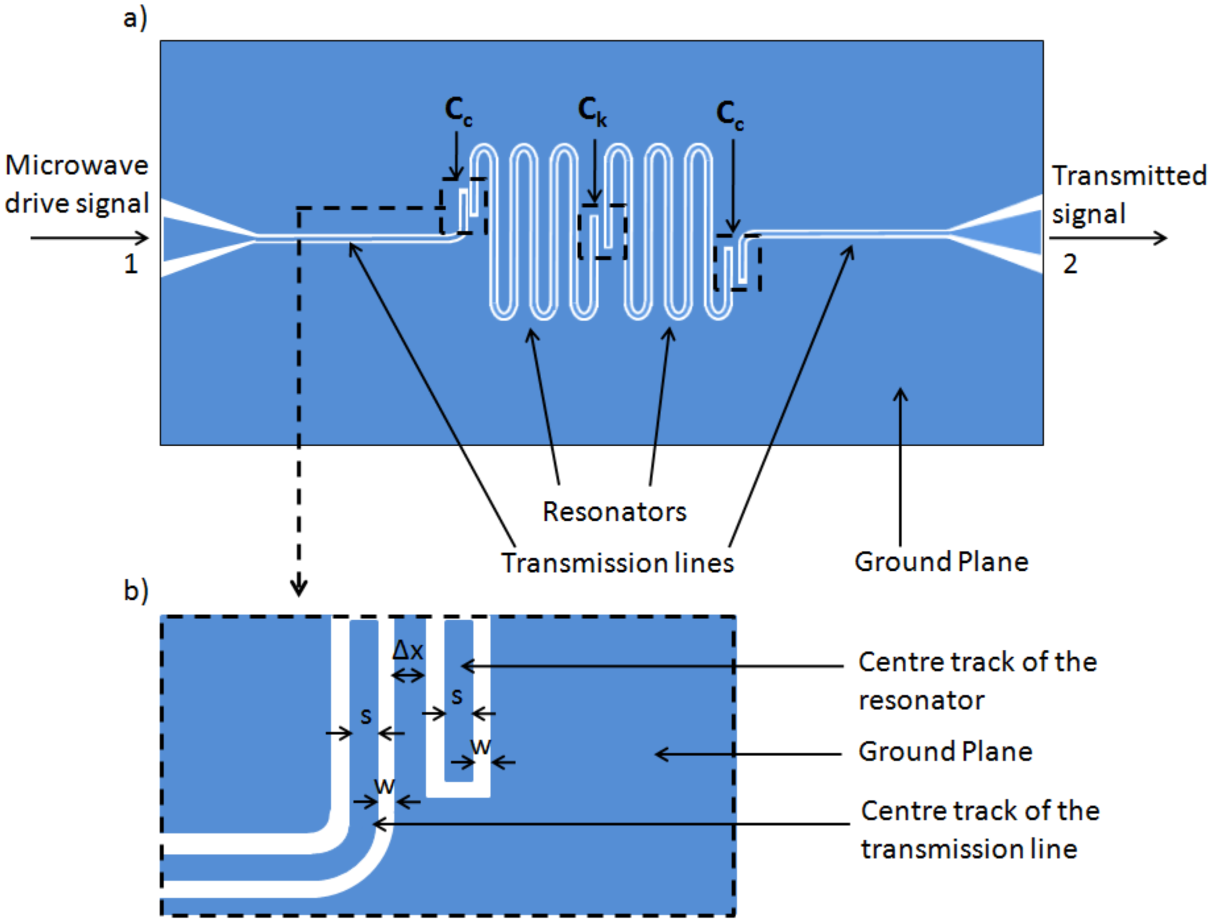

Figure 4.3: **Geometry D** : Design of a system of two identical coupled microwave resonators in the coplanar geometry. Blue regions in the figure represent the metal layer (niobium), and white regions represent the bare substrate (oxidized silicon).**(a)** The resonators are driven by a microwave signal that is fed via capacitive coupling between the transmission line and the resonator. The resonators are coupled to each other by a weak coupling capacitance in the overlap region of their centre tracks. The transmitted signal from the resonators is coupled via C_c to another transmission line which is then fed to the measurement circuitry. **(b)** The region enclosed in the dashed rectangle in **(a)** is enlarged in (b). The width of the centre tracks of the transmission lines and the resonators is represented by s, which was designed to be 10 μm. The gap, w, between the centre tracks and surrounding ground plane was chosen to be 5 μm. The width of the ground plane between the overlapping centre tracks (of the transmission line and the resonator, and of the two resonators) is represented by Δx. Δx between the resonators is either s (10 μm), $2s$ (20 μm) or $3s$ (30 μm) in all our designs.

the ends of both the resonators. There are two advantages of the modified geometry: a) A selected resonator on the chip could be magnetically tuned, independent of the other resonator. b) The resonant frequency could be perturbed by a low frequency (∼ MHz) alternating magnetic field generated from a small coil placed underneath the chip as explained in chapter 6.

To magnetically tune a resonator, the one with a higher resonant frequency needs to be identified by making low temperature measurements on the device. Then, a region in the ground plane close to the edge of the resonator chip is scraped off as shown in fig. 4.4 so that the selected resonator is tunable.

The details of the resonator circuit that was fabricated and measured in this geometry are listed in table 4.1.

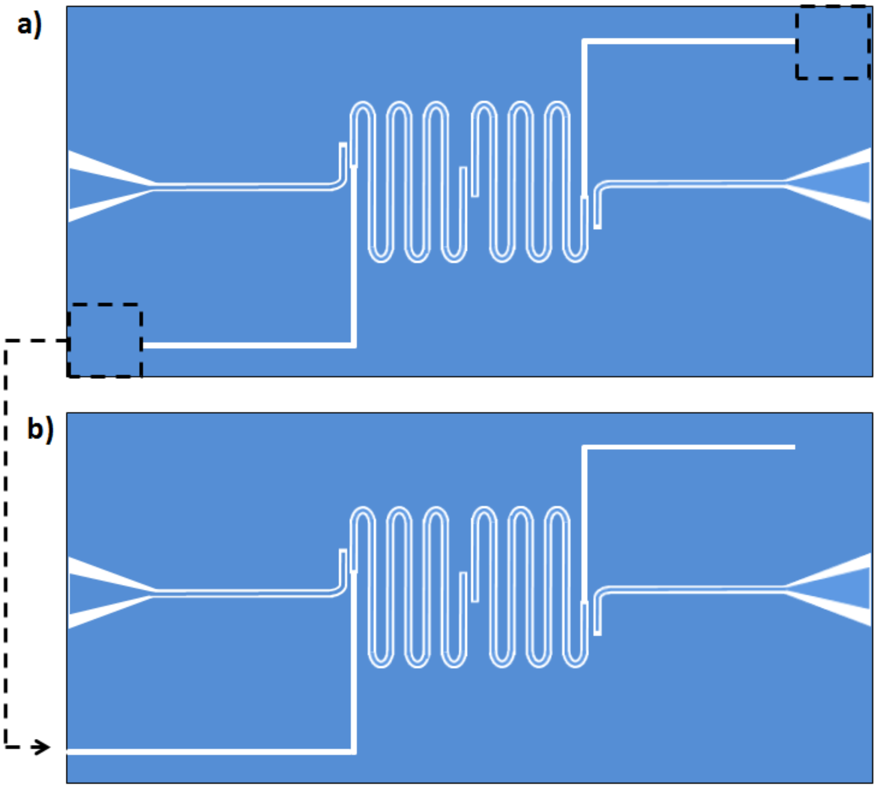

Figure 4.4: **Geometry E** : In comparison with geometry D, it can be seen that the centre track of the resonators close to the transmission lines are not completely shielded by the ground planes. Narrow slits in the ground plane were made to allow for flux penetration into the resonators. Depending on which of the two resonators had a higher resonant frequency, the metal layer within the dashed square in (a) is eliminated to result in structure (b). As an example, in this figure the metal layer is removed from the left side of the structure, so that the resonator on the left could be tuned with a magnetic field, leaving the other resonator largely unaffected.

4.2.3 Design variations to allow for the fabrication of nanomechanical resonators

The ultimate goal of this thesis is to study the interaction of a nanomechanical resonator with a system of identical coupled microwave resonators as proposed by the theoretical model in [4]. Hence, it was decided that initially the case of coupling a nanobar directly to only one of the resonators would be investigated and the observations compared with similar experimental work in [11]. Therefore resonator circuits were designed which enabled the fabrication of a nanobar close to the voltage anti-node of one of the resonators as shown in fig. 4.5. The nanobar length and position were chosen for the same reasons discussed in detail in section 3.1.5.

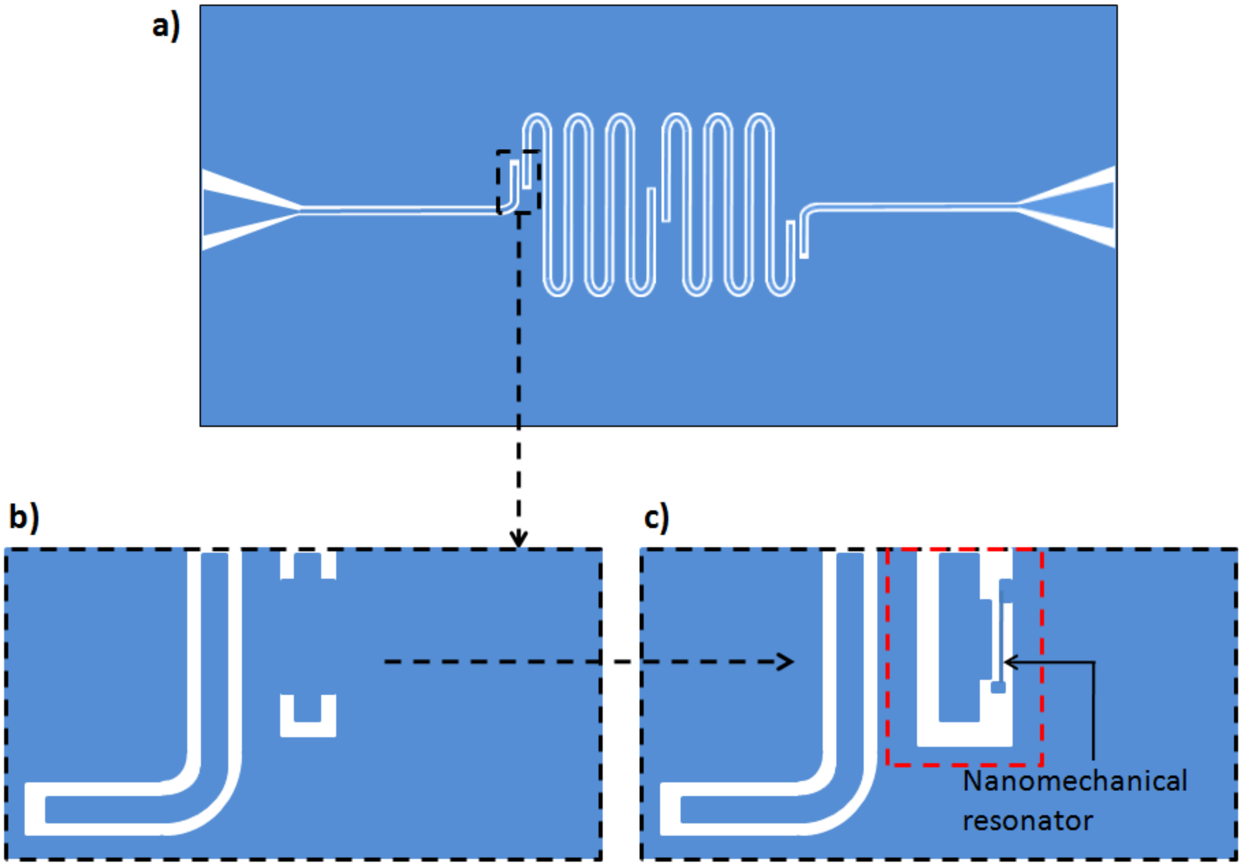

Figure 4.5: **Geometry F**: Design for coupling a nanobar to a microwave resonator. (a) is the repetition of geometry D. To enable the fabrication of a nanobar close to the voltage anti-node of the resonator, geometry D was modified as shown in (b), which results in structure (c) after the nanobar is fabricated. The region enclosed in the dashed rectangle in (c) is enlarged in fig. 4.6.

Several variations of the coupled resonator devices in geometries D, E and F were designed using KIC [68], an integrated circuit layout editor and the design file was sent to Compugraphics, Ltd, where the designs

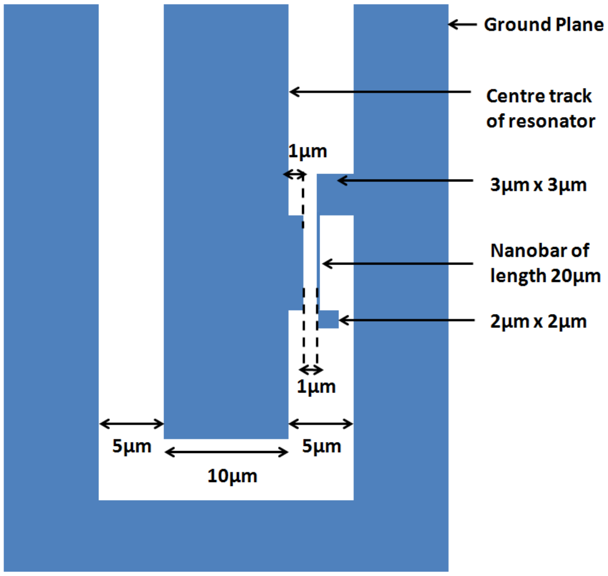

Figure 4.6: Shows details of the nanobar structure enclosed in the red-dashed rectangle in fig. 4.5c.

Geometry	$L_c(\mu\text{m})$	$C_c(\text{F})$	Δx $(C_k)(\mu\text{m})$	$L_k(\mu\text{m})$	$C_k(\text{F})$	Sample Label
D	100	7.65×10^{-16}	10	200	1.57×10^{-15}	5
				100	7.65×10^{-16}	6
				50	3.66×10^{-16}	7
			20	40	1.48×10^{-16}	8
E	100	7.65×10^{-16}	30	50	1.09×10^{-16}	9

Table 4.1: List of new coupled resonator devices that were patterned and measured at low temperatures.

were patterned on a photomask.

The devices listed in table 4.1 were fabricated on thin film niobium on oxidized silicon substrates using photo-lithographic methods explained in section 3.2. To enable measurements to be made on the samples, they were enclosed in a sample housing, which is described in section 4.3.

4.3 Sample Housing

As described in section 3.3, measurement of the resonator properties was achieved by first gluing the sample to a commercial dielectric PCB clad on both sides with 17.5 μm thick copper foil and patterned as shown in fig. 4.7. The new design of the sample housing that comprised the PCB and the copper cavity, was adapted from the experimental work of Hornibrook et al [74].

The differences between the sample housing in this section and in section 3.3 were the following:

- The PCB and box dimensions were made smaller in order to restrict background microwave resonances to higher frequencies, outside the operating range of $5.5 - 6.5$ GHz.
- The total number of transmission lines on the PCB were lowered from six to two, so that parasitic coupling between adjacent lines was absent.
- The width of the transmission lines was decreased from 500 μm to 200 μm to prevent microwave radiation losses.
- The diameter and length of the SMA centre pins were reduced to prevent radiative coupling of microwaves between the two measurement ports on the PCB.
- The number of vias on the PCB were increased so that there was minimal propagation of microwaves within the PCB. The diameter of the vias on the new PCB was 500 μm, with a spacing of 1200 μm between their centres.
- Finally, the PCB was soldered to the base of the copper cavity and the vias acted as a means to ground the entire top surface of the PCB.

Electrical connections were made between the corresponding transmission lines and ground planes on the PCB and sample with aluminium wire bonds. The centre pins of microwave SMA connectors were soldered to the other ends of the transmission lines and outer portions are fitted to the base of the copper cavity. The sample housing was then mounted on the cryostat. The coaxial cables on the cryostat were connected to the

SMA connectors on the PCB, thus enabling low temperature microwave measurements to be made on the resonator sample.

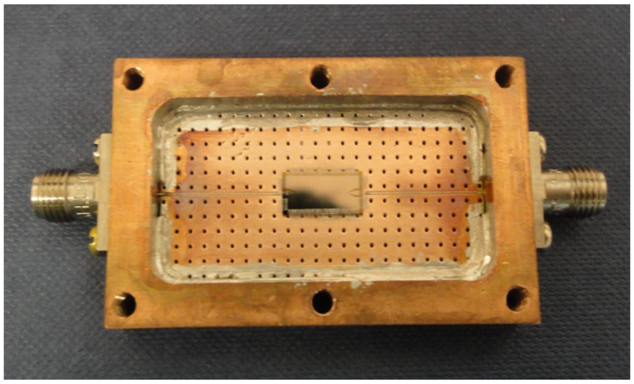

Figure 4.7: A resonator device in geometry D is wirebonded to the new copper PCB. Both the back and the front (only along the edges) of the PCB are soldered to the base of the copper cavity.

The background level in the new design of the sample housing in fig. 4.7 showed an improvement of ≈ 30 dB from the previous design in fig. 3.11. It can be seen in fig. 4.8 that a low microwave background level that would not interfere with the superconducting resonances was obtained in the new design. It was necessary to maintain this level as low as possible to prevent distortion of the Lorentzian resonance peaks as well as to inhibit a degradation of their quality factors [74, 75, 77]. The reason for the peaks at 7, 8.5 and 9 GHz, (in fig. 4.8) in the new cavity and PCB background level was not known. Since the peaks were outside the operating frequency range, they were not of great concern and measurements on the resonator samples were expected to be unaffected. As mentioned earlier, the design of the new PCB and copper cavity were adapted from Hornibrook et al [74] and exceptional peaks were observed at 8 and 10.5 GHz in the transmission spectrum of their sample housing, and no explanation for the peaks was provided.

The coupled resonator devices were measured using the new sample housing. The experimental set up was the same as that illustrated in fig. 3.14. In the following section results from low temperature microwave measurements on the these samples are discussed.

4.4 Results and discussion of measurements on new coupled resonator devices

In this section, the results from measurements on samples $5-8$ (details listed in table 4.1) are discussed in detail. The data was recorded in both transmission and reflection modes using the network analyser as

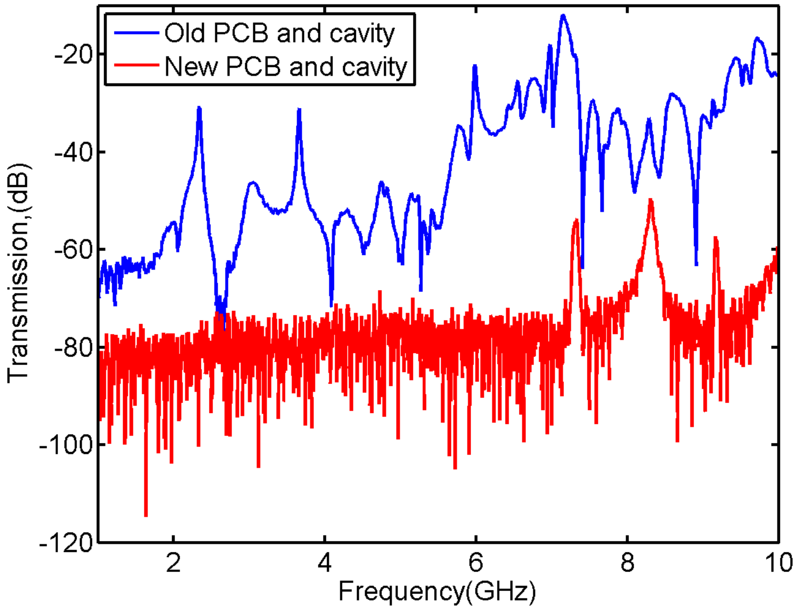

Figure 4.8: This figure compares the transmission of microwaves at room temperature in the two designs of the sample housing without a resonator sample on the PCB. An improvement of ≈ 30 dB in the background level was measured in the new design.

described in section 3.3.2. The notation listed in table 3.3 was used to define the various measurement modes for the geometry of sample 6, i.e., S21 represents transmission measurements on the resonators and S11 and S22 represent reflection measurements. All the samples were measured at 1.4 K.

The measured S21, S11 and S22 data for sample 6 is shown in figs. 4.9, 4.10 and 4.11 respectively. Two peaks at the fundamental frequencies, with a separation of ≈ 9.7 MHz were observed in the transmission (S21) data. The peak shapes were not completely Lorentzian, which indicated that crosstalk was still present within the chip and PCB. The asymmetry in the magnitude of dips in the reflection data(S11 and S22) is discussed later in the text.

Simulations were performed in AIM Spice using the coupled resonator circuit in fig. 4.2 and the input parameters listed in table 4.2 to obtain the theoretical data shown in figs. 4.9, 4.12 and 4.13 (for sample 6).

The absolute values of the measured resonant frequencies deviated from the originally designed values of 6 GHz. Hence, in the simulations, both the resonator lengths were increased by ≈ 5% from the original values (as indicated in table 4.2), to match with the measured frequencies, and their resistance per unit length was varied to obtain measured values of quality factors. Although the resonators were designed to be identical, the simulations required the difference in their lengths to be ≈ 13 μm to obtain the measured frequencies

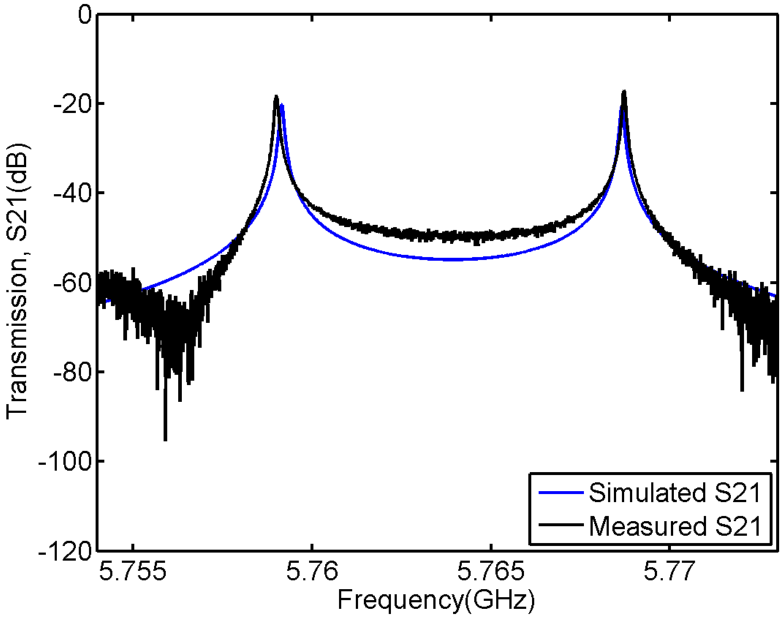

Figure 4.9: Measured and theoretical data for sample 6. The measured fundamental resonant frequencies were at 5.7590 GHz and 5.7687 GHz with quality factors of 6.4×10^4 and 7.7×10^4 respectively. The theoretical data was obtained from simulations in AIM Spice, as described in the text, and the input parameters used in the simulation are listed in table 4.2.

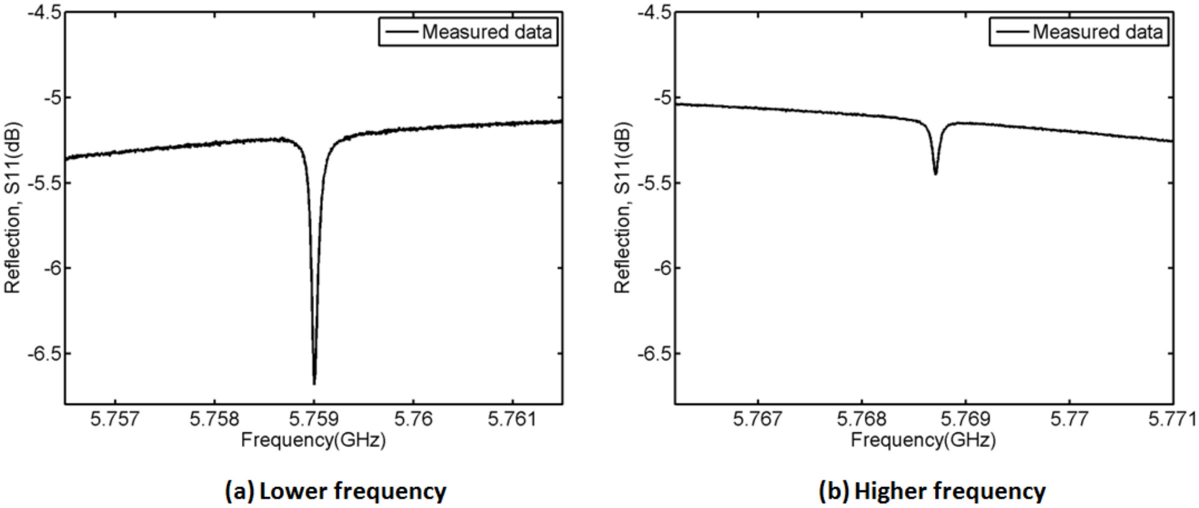

(a) Lower frequency

(b) Higher frequency

Figure 4.10: Measured S11 data in (a) and (b) show dips at the lower and higher frequencies respectively.

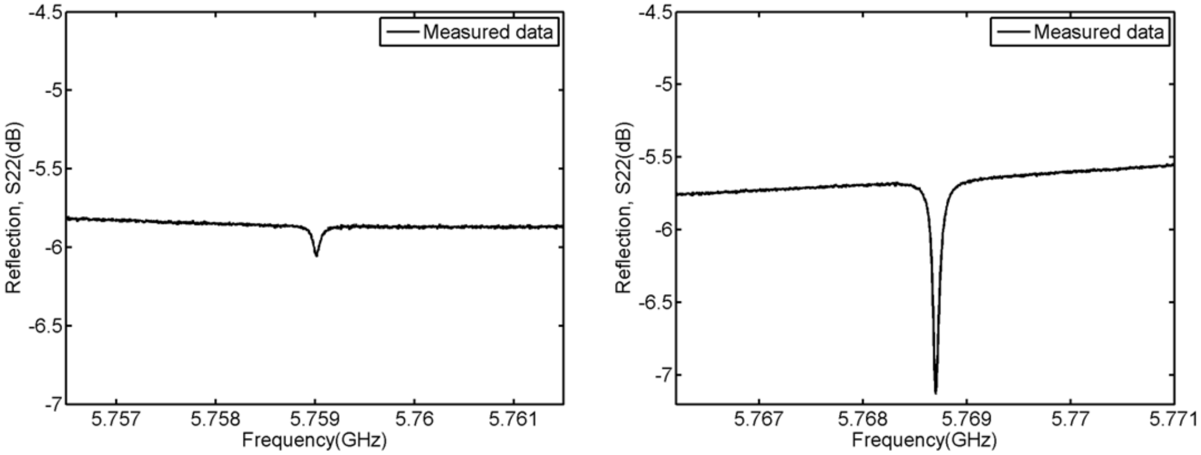

(a) Lower frequency **(b) Higher frequency**

Figure 4.11: Measured S22 data in (a) and (b) show dips at the lower and higher frequencies respectively.

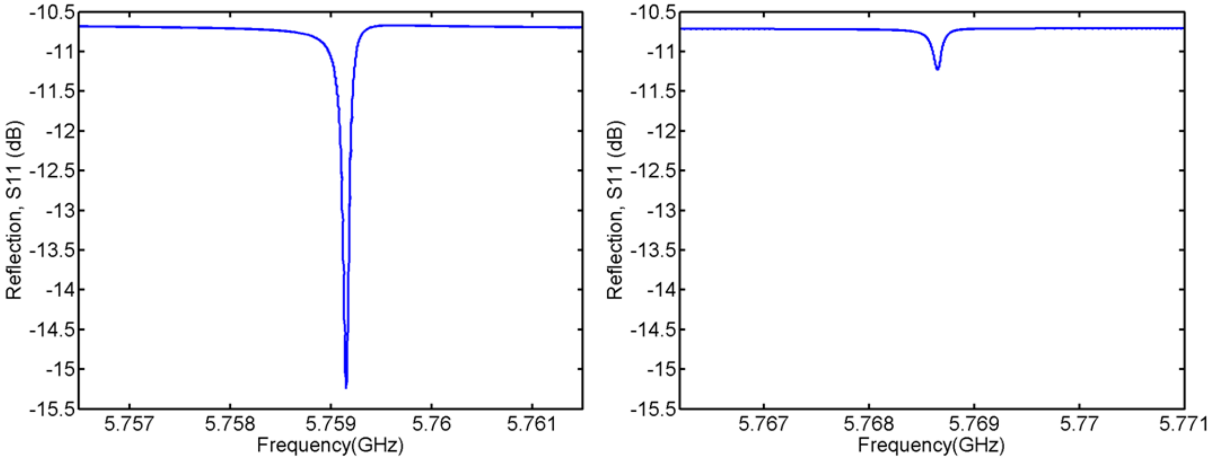

(a) Lower frequency **(b) Higher frequency**

Figure 4.12: Simulated S11 data in (a) and (b) show dips at the lower and higher frequencies respectively. The simulated data was computed with the input parameters listed in table 4.2.

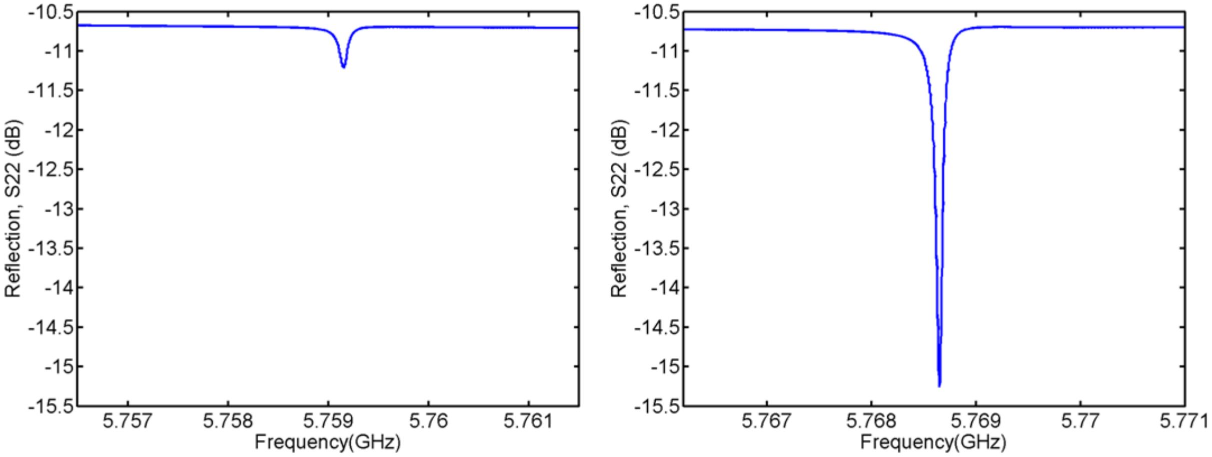

(a) Lower frequency **(b) Higher frequency**

Figure 4.13: Simulated S22 data in (a) and (b) show dips at the lower and higher frequencies respectively. The data was computed with the following input parameters listed in table 4.2.

and unequal peak/dip magnitudes. In the original design, the overlap length of the resonator centre tracks was chosen to result in $C_k = 7.65 \times 10^{-16}$ F, hence a splitting of 6.1 MHz in the frequencies. But, to match with the measured splitting of $\approx$ 9.7 MHz, C_k was increased by $\approx$ 30%. The value of C_c was increased to obtain a close agreement with the observed peak/dip magnitudes.

Simulation Parameter	Fitted Value	Original Value
Length of resonator 1	1.0495×10^{-2} m	1×10^{-2} m
Length of resonator 2	1.050×10^{-2} m	Variable Parameter
R/l of resonator 2	0.12 Ω/m	Variable Parameter
L/l of both resonators	4×10^{-7} H/m	4×10^{-7} H/m
C/l of both resonators	1.7×10^{-10} F/m	1.7×10^{-10} F/m
C_c	2.1×10^{-15} F	7.65×10^{-16} F
C_k	9.945×10^{-16} F	7.65×10^{-16} F

Table 4.2: The AIM Spice circuit parameters required to predict the behaviour of the resonators on sample 6.

A comparison of the theoretical and measured data showed that the resonators on sample 6 were non identical and hence away from the avoided crossing. Further insight was obtained from reflection measurements on the sample shown in figs. 4.10 and 4.11. The dips in S11 and S22 indicate the power absorbed at the resonant frequencies. In each of the reflection measurements, there was an obvious asymmetry in the dips at the two resonant frequencies. In the S11 data, the magnitude of the dip at the lower frequency was bigger in comparison with that at the higher frequency. The magnitude of the dips in S22 measurements showed a pattern opposite to that in S11.

Simulations in AIM Spice were used to assess the reason for unequal magnitudes of the dips. It was discerned that a small difference in resonator lengths (shown in table 4.2) caused large asymmetries in the reflected signal. This meant that, away from the avoided crossing, where the resonators were of different lengths, they no longer behaved as a coupled resonator system, but as two individual resonators with different resonant frequencies. It was evident from the simulated reflection data in figs. 4.12 and 4.13 that the resonator which was closer to the measurement port always had a bigger dip because it was directly driven by the microwave signal. An advantage of this asymmetry was that it helped us to identify which of the two resonators on the chip had a lower resonant frequency, and therefore enabled selective tuning of an individual resonator to reach the avoided crossing (See chapter 5 for more details).

Thus far, only the results from measurements on sample 6 were discussed in detail. The other samples (5, 7 & 8) exhibited similar behaviour, i.e., the absolute values of the frequencies deviated from the designed values of 6 GHz, the frequency separation in each sample was much bigger than the predicted values, and the reflection measurements showed asymmetric dips. The values of measured frequencies were determined by fitting the S21 data to a complex Lorentzian function as described in appendix B.1. The simulated values were obtained by incorporating the originally designed values of resonator lengths and coupling capacitances listed in table 4.1 into the AIM Spice simulation circuit in fig. 4.2.

Sample Label	f_{lower}(GHz)	f_{higher}(GHz)	Δf_{meas}(MHz)	Δf_{sim}(MHz)
5	5.9024	5.9312	29.0	12.0
6	5.7590	5.7687	9.7	6.1
7	5.8533	5.8705	17.0	3.0
8	6.0069	6.0094	2.5	1.5

Table 4.3: List of measured resonant frequencies, their measured and simulated splitting. All the samples have the same value of C_c, and are labelled according to decreasing order of C_k, i.e., sample 8 has the smallest C_k (refer to table 4.1 for C_c and C_k values).

As indicated in table 4.3, simulations in AIM Spice showed that the splitting in the frequencies (Δf_{sim}) decreased with coupling between the resonators. But, Δf_{meas} in sample 7 was greater than that of sample 6, and this anomaly could not be accounted for. A more sophisticated microwave circuit simulation software is required to compute sources of leaky capacitive paths within the resonator circuit, such as parasitic coupling between the meanders of the resonator structures, etc.

The absolute values of the frequencies in samples 5, 6 and 7 deviated largely from the designed value of 6 GHz. From the detailed theoretical analysis for sample 6, it was seen that the difference between the designed and measured values of lengths was well outside the accuracy expected from photo-lithography. Simulations in COMSOL [71] indicated that external factors such as dielectric layers on the sample surface caused by long periods of exposure to the atmosphere, a small tilt of even 100 nm of the sample if not glued parallel to the PCB surface, etc., could produce large shifts ($\sim$ a few hundreds of MHz) in the resonant frequencies.

Whatever the cause, the asymmetric dips in reflection measurements, along with large Δf_{meas}, confirmed that the coupled resonators were away from the avoided crossing. Since significant variation in the resonator lengths were required by the simulations to match with the measured frequencies and their splitting, this implied that other factors that were not accounted into the simulations might affect these parameters. Hence, it was decided that a tuning mechanism with a wide frequency tuning range was required in order to tune one of the resonators and measure the inherent splitting at the avoided crossing. (See chapter 5 for details).

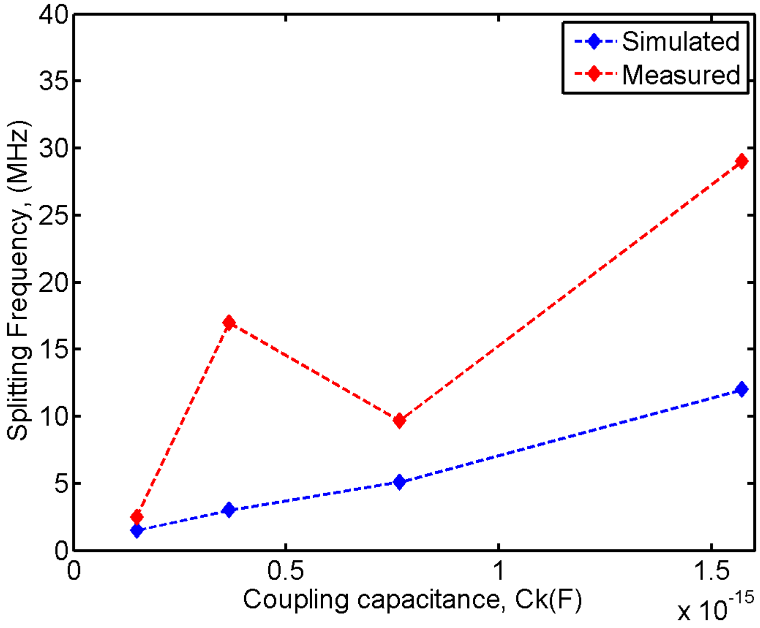

Figure 4.14: A graph showing the simulated and measured splitting in the frequencies versus C_k for samples $5-8$.

CHAPTER 5

TUNING OF MICROWAVE RESONATORS

The studies on microwave-nanomechanical interaction proposed in [4] required the coupling of a nanobar to a system of coupled microwave resonators in which the splitting in the frequencies at the avoided crossing was matched to the resonant frequency of the nanobar. It was ascertained in the previous chapter that the coupled resonator samples measured thus far, were away from the avoided crossing, and it was necessary to tune their resonant frequencies so that the inherent minimum splitting could be measured. In this chapter, the methods employed by other research groups to tune the frequency of superconducting microwave resonators are reviewed. The methods considered for our resonator system are then explained. It was decided that varying the resonator inductance by lowering a superconducting substrate over it with a mechanically controlled probe would be a suitable method. The tuning mechanism that was designed and successfully implemented for our resonator samples is then described. Finally, the results obtained from tuning the coupled resonators through the avoided crossing are presented and discussed.

5.1 Experiments based on tuning of superconducting microwave resonators

Extensive work on tuning of microwave resonators at low temperatures is reported in the literature [7–10, 80–87]. In this section, some of the methods adopted by various research groups that are relevant to our experiments will be briefly reviewed.

Z.Kim *et al* [7], have coarse tuned their thin film niobium on sapphire microwave resonator by electron-beam lithography, but the frequency could only be changed to a fixed value. To observe a continuous fine tuning of the frequency, a superconducting aluminium pin that varied the inductance of the resonator was moved over the resonator using a PZT actuator. A maximum shift of $\sim$ 18 MHz, i.e., from 6.8278 GHz to 6.8454 GHz was achieved when the pin moved from a distance of 600 μm to 40 μm respectively, for an applied step voltage of 36 V to the PZT actuator.

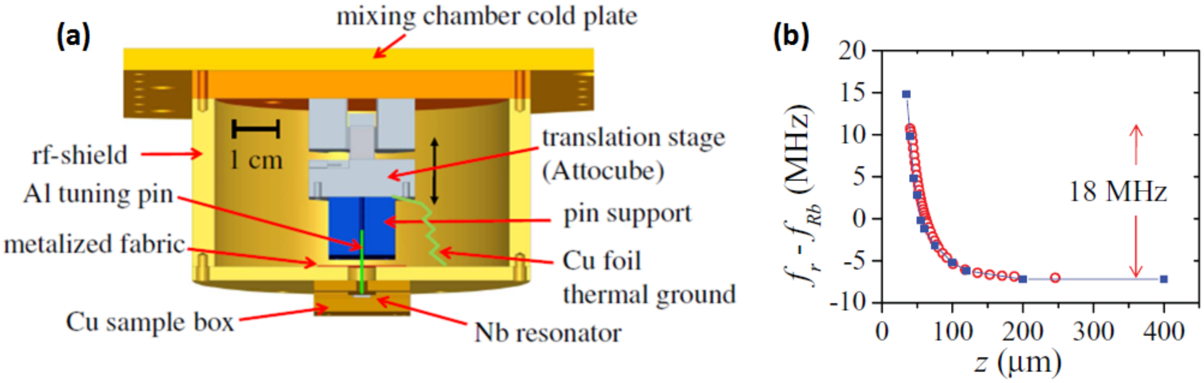

Figure 5.1: (a) Schematic representation of the tuning mechanism developed by Kim et al. The frequency of a thin film niobium resonator was tuned with a superconducting aluminium pin lowered over it by piezoelectric actuation. (b) A maximum detuning of 18 MHz was obtained for a bias voltage of 36 V and a pin height of 40 μm above the resonator. This figure is taken from [7].

Although, fine tuning (maximum of 8.7 kHz per 60 nm) of the piezoelectric step was achieved with this method, there was a large degradation in the quality factor of the microwave resonance as the pin approached the resonator. The mechanical vibrations in the aluminium pin caused oscillations in the resonant frequency, and hence a broadening of the resonance peak, and an apparent reduction in the quality factor. As the aluminium pin approached the resonator, vibrations of $\sim$ 0.7 μm caused frequency shifts of $\sim$ kHz, thereby broadening the resonance and reducing the efficiency of this tuning mechanism.

Lancaster *et al* [8], demonstrated a method to tune a YBCO microwave resonator with a dielectric (silicon) tuning probe that could be moved vertically over the resonator. The vertical movement of the tuning probe was controlled by applying a voltage bias to a silicon actuator that was fabricated and bonded to the resonator chip. The capacitance of the microwave resonator increases as the silicon approaches the resonator, thus decreasing its resonant frequency. The resonant frequency was lowered from 6.30 GHz to 5.54 GHz as the tuning probe moved from a distance of 15 μm to 1 μm above the resonator surface. Although a tuning range of 12% for a bias voltage of 40 V was achieved, the quality factor of the resonator dropped from 1078 to 104 as the tuning probe approached the resonator. This large drop in quality factor was associated with dielectric losses in the silicon substrate and was expected to be lower in higher resistivity dielectric materials such as sapphire.

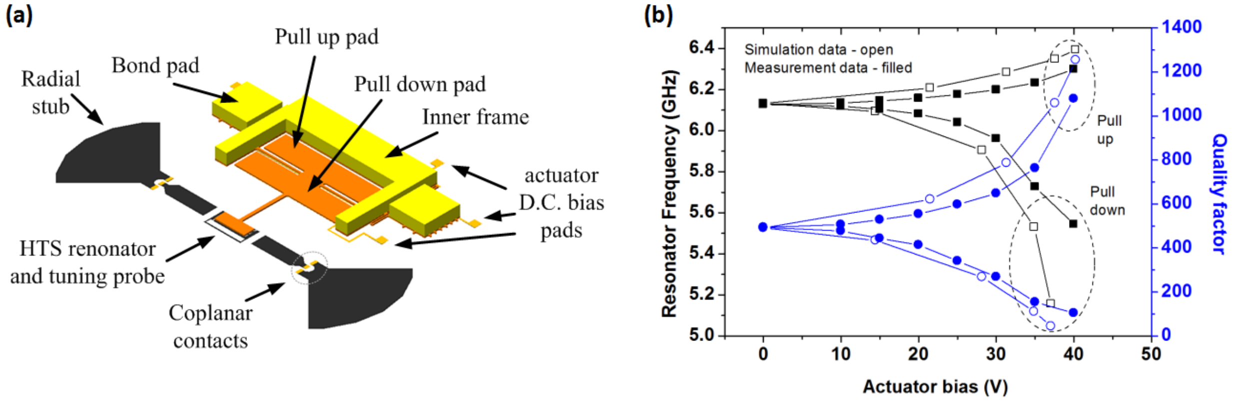

Figure 5.2: (a) Schematic representation of the tuning mechanism with a silicon actuator. (b) Detuning and the variation in quality factor of the YBCO resonator as a function of voltage bias to the silicon actuator. This figure is taken from [8].

The tuning of a superconducting cpw microwave resonator at 4.2 K was achieved by Healey *et al* [9], by applying a uniform external magnetic field perpendicular to the plane of the resonator. A maximum shift of 2 MHz in the resonant frequency for a dc field of 0.1 mT was observed. When an external magnetic field is applied, the number density of Cooper pairs decreases in the superconductor. This results in an increase in kinetic inductance of the superconducting resonator, and hence, a decrease in its resonant frequency. The main advantages of this method are, the ease of implementation as no additional fabrication is required; the decrease in the resonant frequency is monotonic below the critical field of the superconductor; and, the quality factor of the microwave resonance remains constant throughout the tuning range. Thus, it is a very suitable method for in-situ tuning of microwave resonators at low temperatures when only small shifts in the resonant frequencies are required.

A wider tuning range in a $\lambda/4$ superconducting cpw microwave resonator was reported by Sandberg *et al* [10], whereby the voltage node of the resonator was coupled to a superconducting quantum interference device (SQUID). The SQUID can be considered as an additional inductance in series with the distributed inductance of the microwave resonator. The inductance of the SQUID can be varied by applying an external magnetic field, hence enabling the microwave resonant frequency to be varied. A lowering in the resonant frequency of a 4.8 GHz resonator by 740 MHz was observed, when an external magnetic field was applied. Although a wide tuning range was achieved, the degradation in the quality factor of the resonator from $10,000$ to 2000 due to an additional resistance in the Josephson junctions does not make it a feasible method

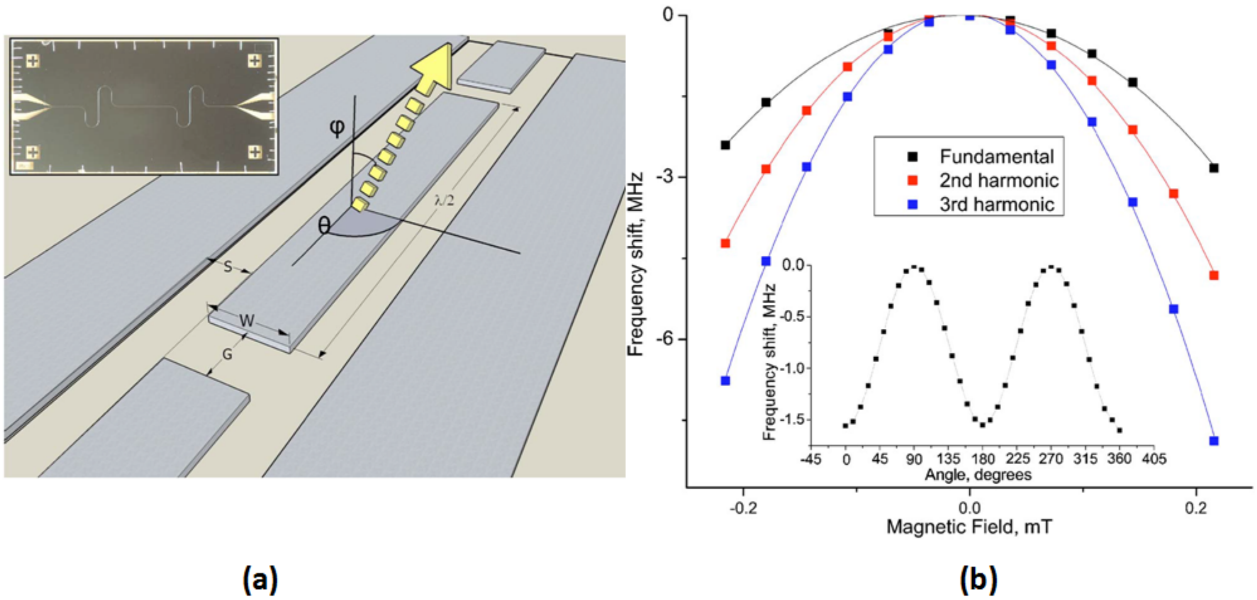

Figure 5.3: (a) Tuning of a cpw microwave resonator with an external magnetic field applied perpendicular to the plane of the resonator surface. (b) Frequency shift as a function of applied field. This figure is taken from [9].

to be implemented in our experiments. Therefore, this method could not be employed to tune our system of microwave resonators.

5.2 Tuning the resonators with a dielectric substrate

For in-situ tuning of our microwave resonators at low temperatures, it was decided that the capacitance of a resonator could be altered by moving a dielectric (sapphire) substrate above it with piezoelectric (PZT) actuation. A sapphire substrate of thickness 0.5 mm was machined to cover the area occupied by a single resonator on the chip and then glued to the end of a PZT bending actuator as shown in fig. 5.5. Thereafter, the tuning probe, formed by the sapphire substrate and the PZT actuator would be clamped to the sample enclosure and electrical connections to coaxial cables on the cryostat would be made. This method was considered due to the following advantages:

- Since the movement of the PZT actuator is voltage controlled, small steps in its motion are possible. This enables fine tuning of the resonant frequency.

- There is a monotonic relation between the applied voltage and the crystal motion, which eases the process of adjusting the frequencies.

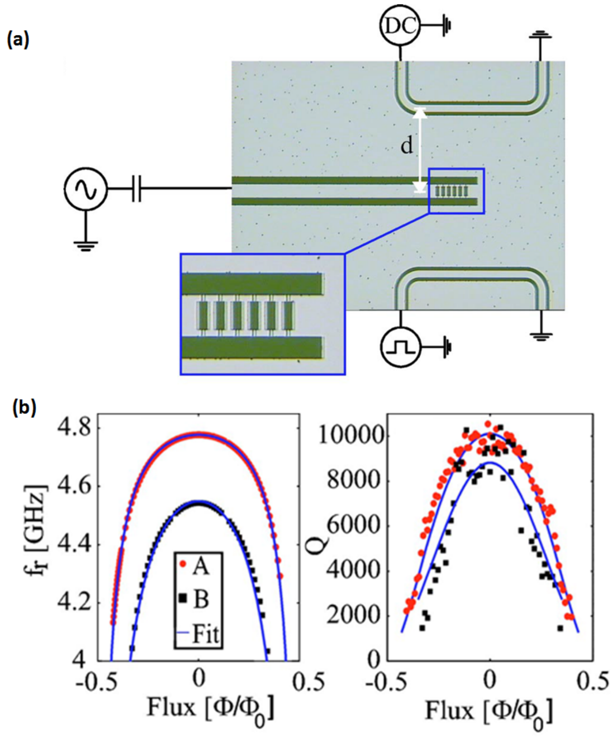

Figure 5.4: (a) A tunable, quarter wavelength coplanar resonator with an array of SQUIDs at its voltage node. (b) Detuning of the resonant frequency with the applied flux by coupling to a single as well an array of SQUIDs. The quality factor of the resonator is observed to degrade with an increase in the applied flux. This figure is taken from [10].

- All our low temperature measurements were made in a cryostat where the sample enclosure (copper cavity + copper PCB) is immersed in a liquid helium bath. Since the PZT actuator would be clamped to the base of the copper cavity, there is no need for more complex mechanical parts with concomitant heat sinking issues, thereby rendering it a feasible method to be implemented for our experiments.

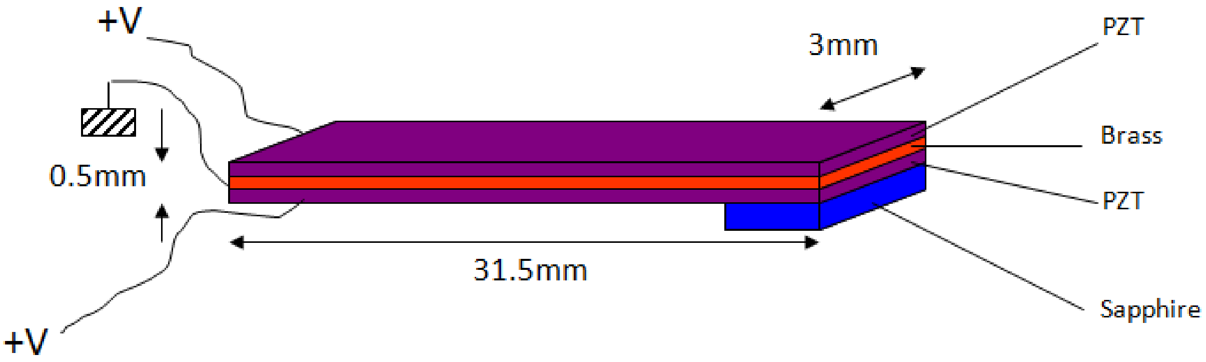

Figure 5.5: Schematic representation of a tuning probe comprising a sapphire substrate glued to a PZT bending actuator. The sapphire substrate could be raised and lowered over the resonator sample with a piezoelectric actuation stage. At room temperatures, the crystal moves a distance of 100 μm for a bias voltage of 1 V and has a maximum travel of 1 mm.

At low temperatures, a 1 V bias was expected to produce 10 μm ($\sim$ 10% of its range at 300 K) of movement in the actuator. The capacitance of the microwave resonator increases as the dielectric is lowered towards it, hence decreasing the resonant frequencies. Simulations in COMSOL [71] showed that a maximum lowering of 22 MHz in the resonant frequency could be obtained when the dielectric substrate was 30 μm above the resonator surface. However, due to the following disadvantages, it was not used in our experiments:

- Clamping the tuning probe to the sample enclosure required additional holes to be drilled on the PCB as well as the copper cavity, which might result in microwave radiation losses.
- Mechanical vibrations in the tuning probe as it approaches the resonator would lower its apparent quality factor [7].
- It is known that PZT actuators are typically a factor of ≈ 10 less sensitive at liquid helium temperatures. Therefore, if greater shifts in the resonant frequencies are required, then, a greater displacement of the PZT actuator over the resonator would be necessary. This implied that large voltages would have to be applied, thereby causing a significant danger of electrical breakdown and damage to expensive measurement electronics.

As an alternative method, the movement of the tuning probe could be controlled by an inchworm mechanism, but it is bulky and expensive to incorporate into our experimental set-up and was therefore not implemented.

Hence, it was proposed that a more suitable method for our system of coupled resonators would be a mechanical actuator that would control the movement of the tuning probe over the selected resonator. It will be explained and shown in the following sections that a wider tuning range could be achieved by using a superconducting instead of a dielectric substrate. Additional fabrication techniques will not be required by this method, and, the quality factor of the microwave resonator was expected to *not* degrade since a superconducting substrate would be lowered over the resonator.

5.3 Choice of tuning probe

The proposed method of tuning was to lower a tuning probe over the selected microwave resonator through the lid of the copper cavity in which the sample is enclosed. The vertical movement of the tuning probe would be controlled by a mechanical means. Therefore, a small hole was drilled on the lid of the copper cavity, through which the tuning probe could be lowered towards the resonator sample. The tuning probe would comprise a tuning disc machined from a niobium on silicon dioxide substrate attached to the end of a long, thin rod. Since the active face of the tuning disc would be a superconductor, lowering it over a superconducting resonator would decrease the resonator inductance and hence *increase* its resonant frequency. Simulations in COMSOL [71] show that the advantages of a superconducting layer over a dielectric layer as the active face of the tuning device are, a wider tuning range and a monotonic increase in the resonant frequency as shown in fig. 5.6.

Since it was necessary to maintain a low microwave background level within the copper cavity, the material of the tuning probe that penetrates into the cavity had to be chosen carefully, so that the tuning probe itself does not cause any unwanted background resonances or undesired damping of the quality factor of the resonator, within our operating frequency range of 5-6.5 GHz.

Therefore, microwave transmission measurements at room temperature were made by inserting a series of conducting and insulating tuning probes through the lid of the cavity to observe their effect on background resonances. From fig. 5.7 and 5.8, it was observed that, lowering a tuning probe made of conducting material (for example,brass) into the copper cavity caused shifts in the background microwave resonances into the frequency range of interest, and therefore, were not desirable; tuning probes machined from insulating materials such as nylon and macor did not have a significant effect on the background resonances and hence

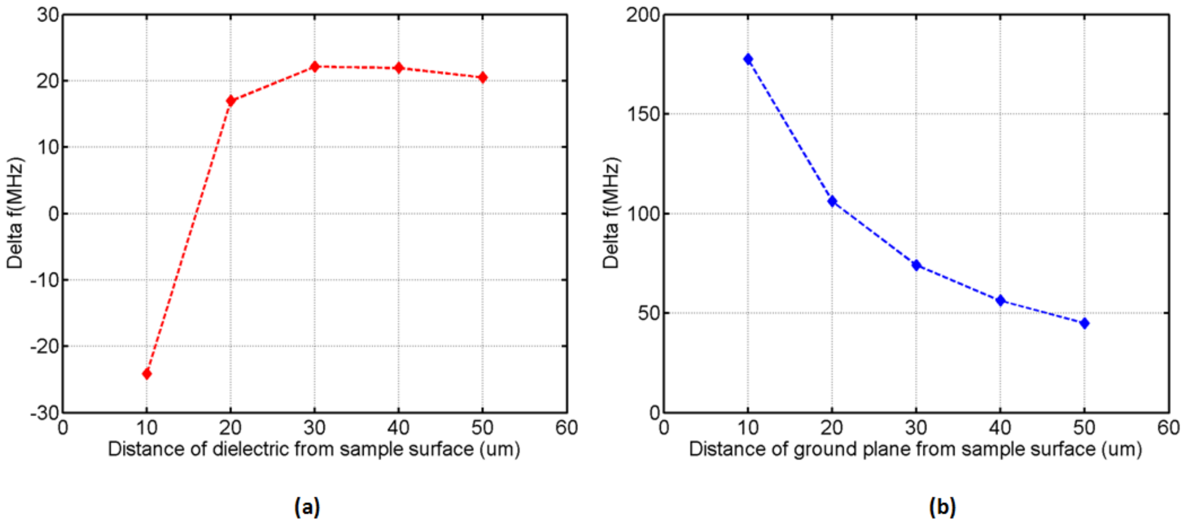

Figure 5.6: (a) and (b) show the shift in resonant frequency when a dielectric substrate ($\epsilon_r = 10$) and a superconducting layer (ground plane) as the active face of the tuning disc, respectively are lowered over the resonator sample.

could be used. Amongst the insulating materials, it was found that macor had the following advantages:

- it is rigid at low temperatures;
- easier to machine into a thin rod;
- smaller coefficient of differential contraction, and
- a small dielectric constant, and therefore would not significantly affect the capacitance of the microwave resonator over which it is being lowered, although the macor rod is expected to be largely screened by the niobium film.

Hence, it was decided that the tuning probe would comprise a macor rod with the tuning disc attached to its end and lowered towards the resonator on the chip as shown in fig. 5.9. The design details and the control mechanism for the vertical movement of the tuning probe are described in section 5.4.

5.4 Tuning Mechanism: Design and working principle

The tuning mechanism underwent a series of stages in its development in order to achieve a useful system and in this section, the final version that was implemented in the experiments is described. The basic operating principle is first outlined and then the important details of the design features are explained.

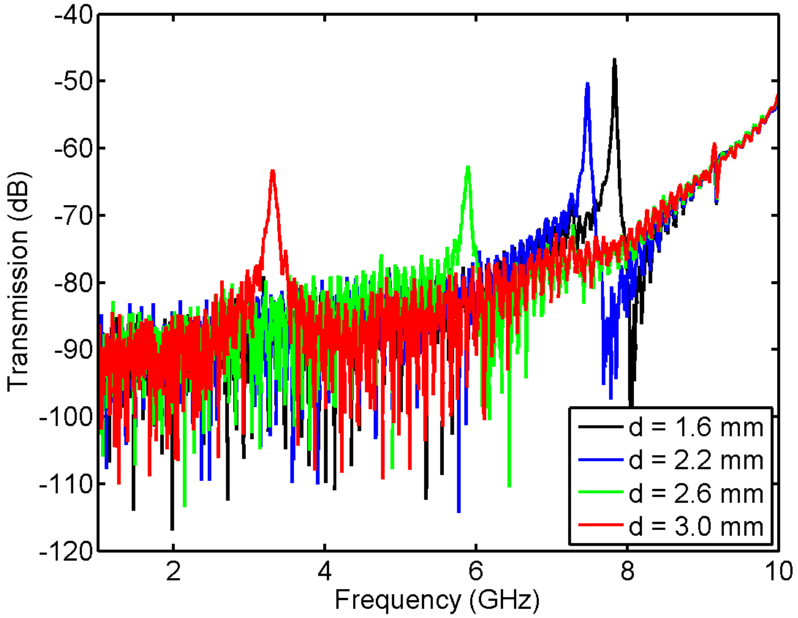

Figure 5.7: Movement of box modes as a conducting (brass) screw was lowered into the copper cavity. Here d is the length of the brass screw inside the copper cavity.

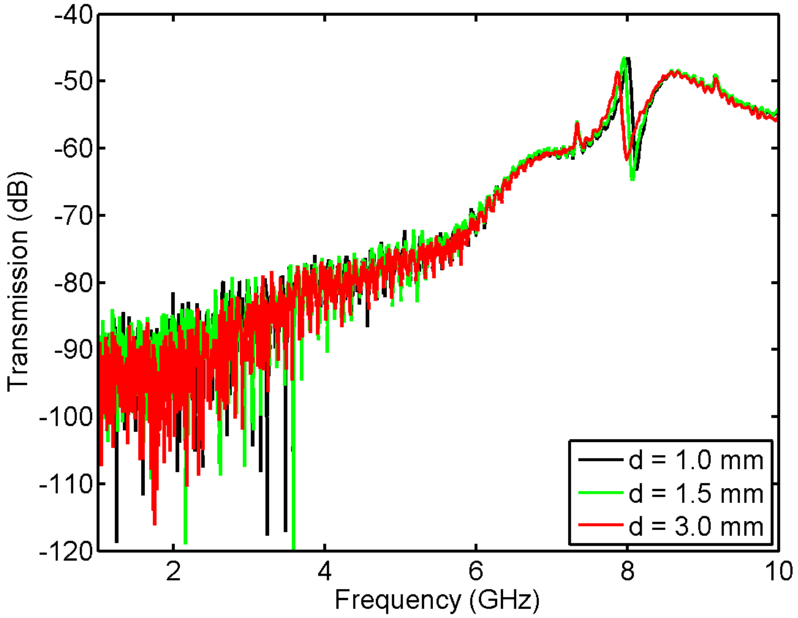

Figure 5.8: Movement of box modes as a non-conducting (nylon) screw was lowered into the copper cavity and d is the length of the nylon screw inside the copper cavity.

5.4.1 Basic operating principle

There are three basic elements:

1. the tuning probe shown in fig. 5.9,
2. the lever (see fig. 5.11), and
3. the tuning rod, illustrated in fig. 5.12.

The lever is held against the tapered end of the tuning rod at all times by spring C and the tuning probe is pressed down towards the resonator by spring B. The tuning rod passes through an o-ring seal at the top of the cryostat and can be rotated manually. As the tuning rod is rotated, the tapered end is moved up or down, i.e., in and out of the plane in fig. 5.11 causing the lever to rotate about the pivot point. This, in turn, raises or lowers the tuning probe against the force of spring B. The height of the tuning disc above the resonator is therefore controlled by the rotational position of the tuning rod.

5.4.2 Design details

Although the tuning disc, like the resonator chip was very flat, it was 1.8 mm in diameter and if it were at an angle of 1° to the resonator, one side of the disc would be $\approx 20\ \mu$m further from one part of the resonator than the other. It is seen in fig. 5.6b that this degree of tilt would seriously compromise the tuning process. There was also a concern that lowering a tilted tuning disc onto the resonator sample could cause mechanical damage. Gluing the tuning disc onto the macor rod and allowing the glue to dry while the tuning disc pressed against the sample was considered, but this method was rejected on the grounds that there might be uneven differential contraction of the tuning probe materials and that it would expose the carefully cleaned resonator to undesirable solvents. Therefore it was decided that silicon grease would be used as the *glue* as it has a very low vapour pressure and any differential contraction would be complete before the grease solidified.

The efficacy of silicon grease as a glue was checked by attaching a spare tuning disc to a macor rod and cooling it in liquid nitrogen. It was found that the grease froze and the tuning disc was held rigidly to the macor rod.

Therefore, the final assembly of the tuning probe was, to glue a ball bearing to the bottom of the macor rod and, after it was well set, attach the tuning disc to the ball bearing with a small spot of silicon grease. The tuning probe was carefully lowered through the hole in the lid of the copper cavity until it rested on the resonator. The ball bearing allowed the tuning disc to take up a position parallel to the resonator chip.

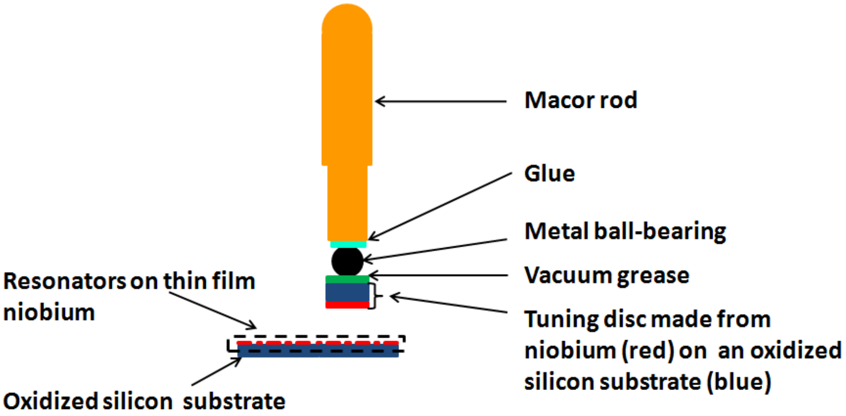

Figure 5.9: Schematic representation of the tuning probe above a coupled resonators sample. It comprises the macor rod, a ball bearing and the tuning disc. The total length of the macor rod is 22 mm. A step in its diameter from 2.4 mm to 1.8 mm was to prevent it from touching the sides of the copper cavity whilst being lowered through it. A recess in the bottom end of the macor rod enables a ball bearing of diameter 1.7 mm to be glued to it. A depression is made on the inactive face of the tuning disc to ensure its adhesion to the ball bearing. The tuning disc is 1.8 mm in diameter and 0.5 mm in thickness.

Fig. 5.11 shows the spring that was used to hold the tuning probe in place. Spring B presses on the head of the macor rod and prevents its lateral movement inside the cavity. The brass plate below spring B provided support to the macor rod and the springs.

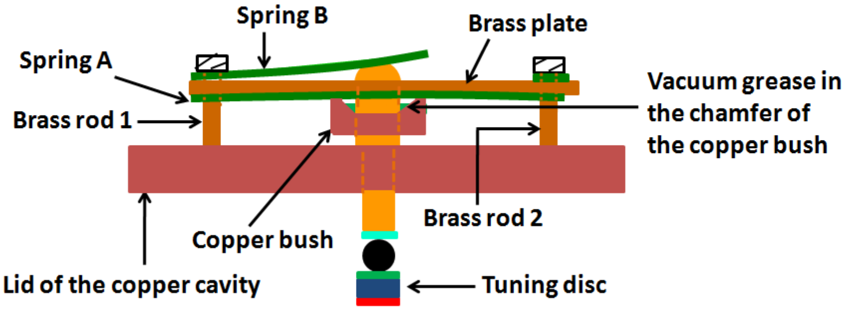

Figure 5.10: Schematic of a side view of the tuning mechanism: A support mechanism formed by leaf springs A and B, and a brass plate, that ensure perpendicular and rigid positioning of the tuning probe over the resonator sample. Spring A presses on the copper bush and ensures that it rests on the lever (as shown in fig. 5.11).

At low temperatures, the copper bush is the means by which the tuning rod is raised and lowered. The bush was initially clamped to the macor rod with a nylon screw and it worked well at room temperatures. On cooling, however, differential contraction was a problem, leading to situations where the tuning probe could not be raised/lowered through the required range. Hence, the clamping screw was rejected and a chamfer was made on the top inner diameter of the copper bush and carefully fitted with silicon grease. The procedure was to adjust the tuning rod to the middle of its rotational range at room temperature and then cool the cryostat. It was found that the silicon grease was a satisfactory clamp/glue and it resulted in a necessary range of movement when the cryostat was cold. As an additional guide, an LED indicator was used which turned on when the lever was in electrical contact with the copper bush and the tuning disc was about to be raised above the resonator chip.

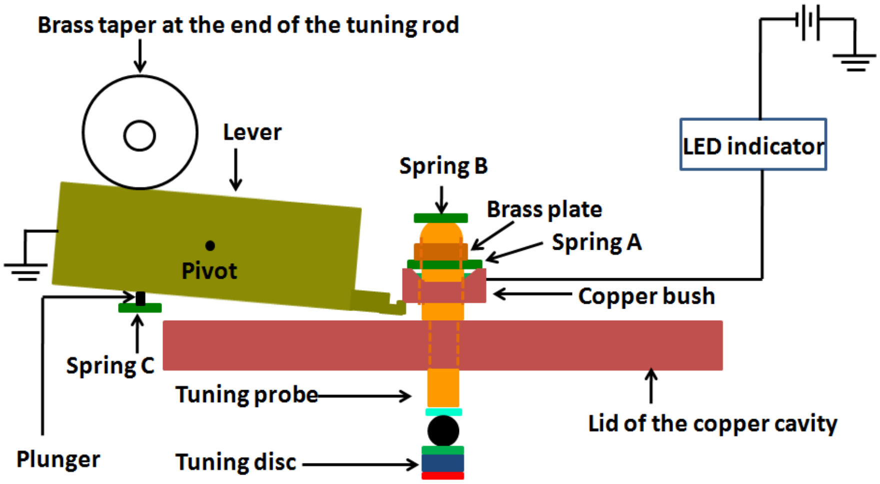

Figure 5.11: Schematic of a cross sectional view of the mechanism that controls the vertical movement of the tuning probe.

The mechanism worked well with ten turns of the tuning rod giving the required range of motion of 220 μm with 22 μm per turn. The resonator devices were successfully tuned by this method and thus, the inherent avoided crossing of the coupled resonator frequencies could be measured.

5.5 Experimental set-up for low temperature measurements

The resonator samples were fabricated by lithographic methods described in section 3.2 and wirebonded to the PCB as shown in fig. 4.7. The copper cavity in which the sample and PCB were enclosed, was clamped to the sample stage of the cryostat as shown in fig. 5.13. Microwave cables on the cryostat were connected to the input and output ports of the copper cavity via SMA connectors. The transmitted and reflected power from the resonators was measured on a network analyser, as described in section 3.3.2.

At room temperature, the tuning probe was lowered through the lid of the cavity until it rested on the sample surface. The copper bush was then fitted to the macor rod so that it rested on the lever. Silicon grease was used to hold the copper bush to the tuning probe, as the grease freezes at low temperatures, and thus enables the copper bush-tuning probe system to function as a single unit. At this stage, since the bush

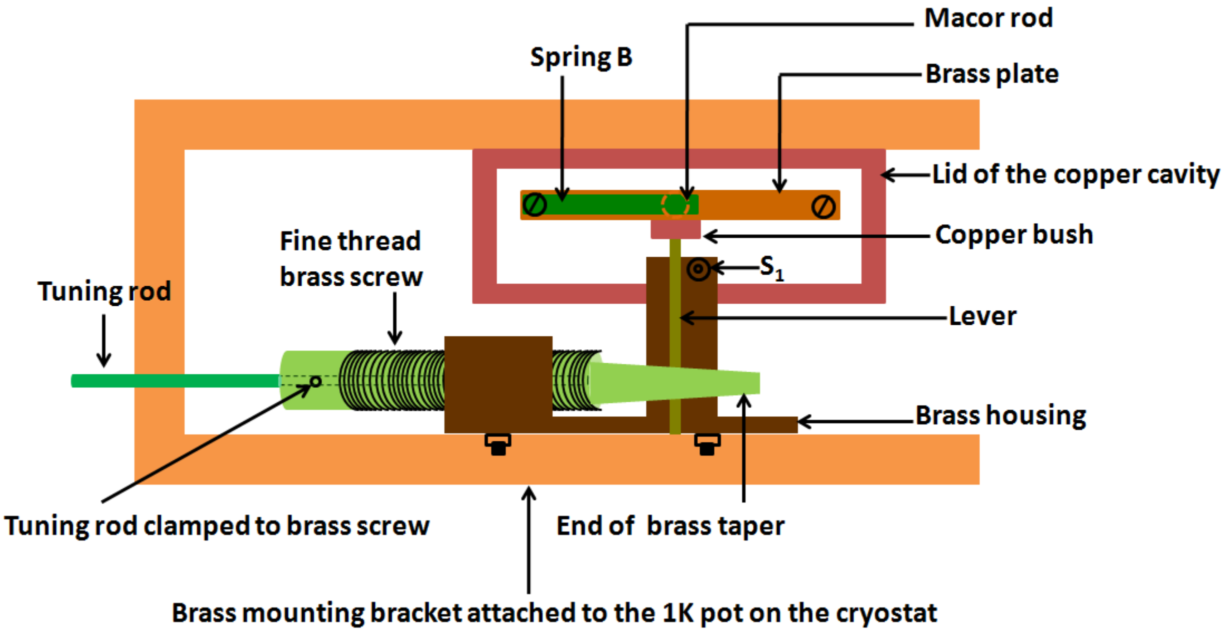

Figure 5.12: Schematic of a top view of the mechanical tuning arrangement which shows that the sliding of the brass taper over the lever enables vertical movement of the tuning probe.

makes contact with the lever, the light indicator is on. After the sample stage is cooled to the operating temperature of 1.3 K, the tuning probe is raised from the sample surface by clockwise turns of the tuning rod. At both room and low temperatures, it was found that the maximum lift of the tuning probe from the resonator surface could be obtained by 10 clockwise turns of the tuning rod. The tuning probe was gradually lowered over one of the resonators and the results from in-situ low temperature tuning experiments are discussed in the following section.

5.6 Results and discussion of tuning measurements

In this section, the tuning of microwave resonators on samples 6 and 8 at 1.3 K are discussed in detail (see table 4.1 for sample parameters). The circuit shown in fig. 4.2 was simulated in AIM Spice to predict the splitting in the coupled resonator frequencies at the avoided crossing, and a comparison between the theoretical and measured values is shown where appropriate.

The resonant frequencies on sample 6 were identified when the tuning probe was at the top of its range where it has negligible effect on the resonant frequencies. The measured splitting (Δf) in the frequencies was ≈ 9.3 MHz, bigger than the predicted splitting of 6.1 MHz. The large deviation of the measured Δf, as well as a difference of $\approx 2 \times 10^4$ in the quality factors of the resonators implied that the system was away

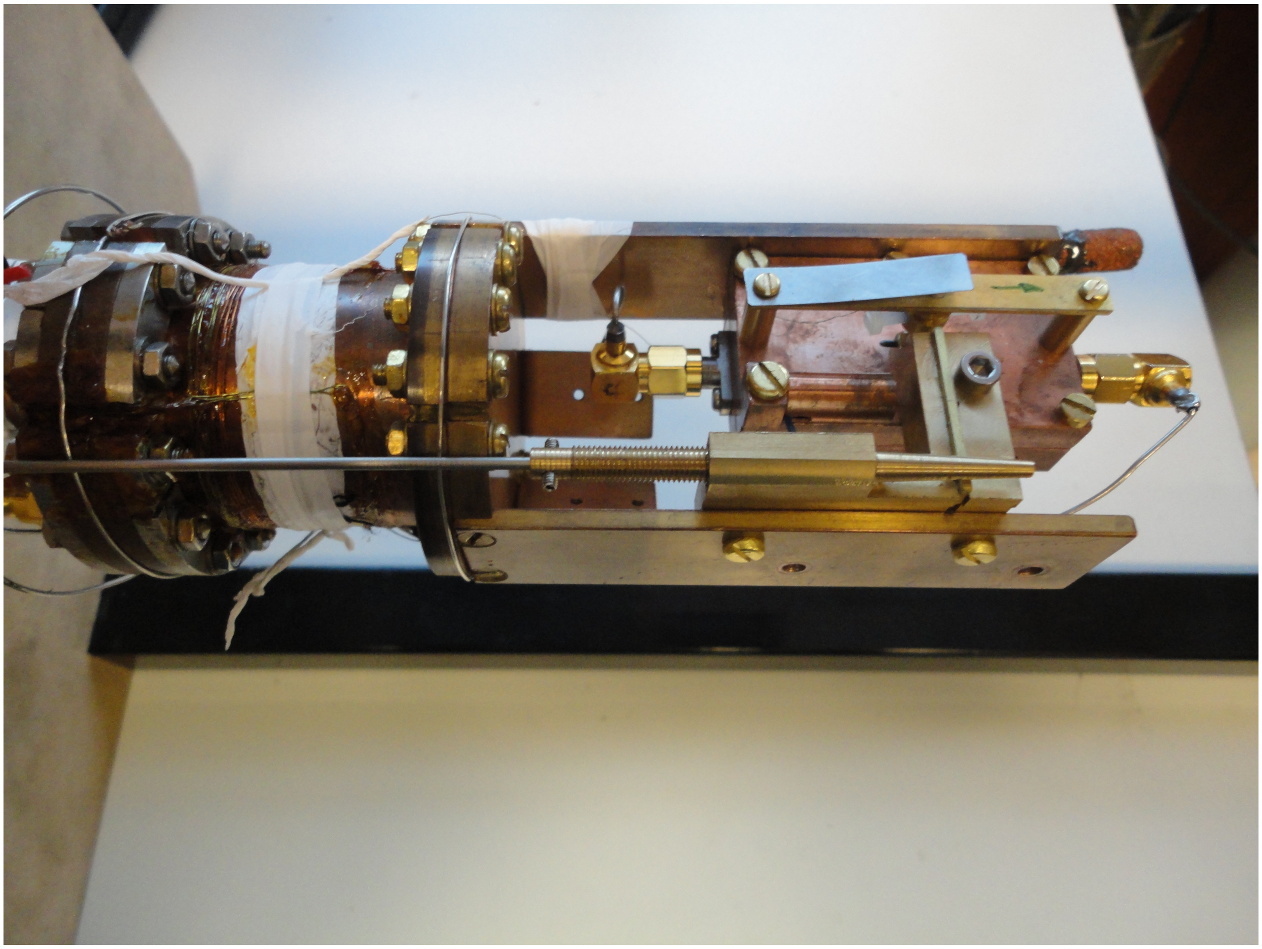

Figure 5.13: Experimental set-up of the tuning mechanism at the sample stage of the cryostat.

from the avoided crossing, and hence, one of the resonators on this sample needed to be tuned.

The tuning probe was then gradually lowered over one of the resonators and, Δf was observed to increase as it approached the sample surface. Since lowering the tuning probe towards a resonator *increases* its resonant frequency, this indicated that the resonator under the tuning probe had a *higher* resonant frequency. Hence, Δf did not go through a minimum during the process of tuning, and an avoided crossing of the frequencies could not be observed. It should be noted here that prior to measuring a sample at low temperatures, it was not possible to determine which of the two resonators required raising of its resonant frequency. Therefore, samples may have to be re-measured such that the resonator under the tuning probe had a lower resonant frequency. This can be easily achieved by detaching the base of the copper cavity from its lid, turning it around by 180° and clamping it back. The experiment on sample 6 was then repeated so that the tuning probe could be lowered over the lower frequency resonator.

The tuning probe was raised to its top most position above the sample, and transmission and reflection of the microwave signal from the resonators was measured. The splitting in the frequencies (Δf) was ≈ 9.7 MHz, as shown in fig. 5.14. The difference in quality factors of the two resonances as well as unequal magnitudes of the dips in the reflection (S11) data in fig. 5.15 showed that the resonators were non identical and hence one of them needed to be tuned to reach the avoided crossing.

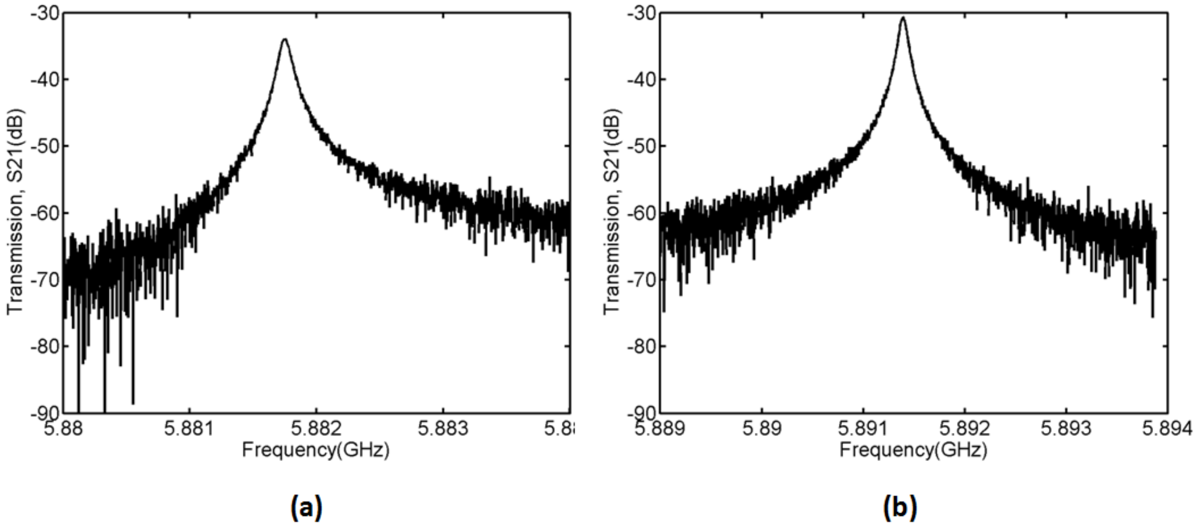

Figure 5.14: Two resonant peaks at $f_{lower} = 5.8817$ GHz in (a) and $f_{higher} = 5.8913$ GHz in (b) with a separation of ≈ 9.7 MHz when the tuning disc was at its furthest point away from the substrate in sample 6. The loaded quality factors of f_{lower} and f_{higher} were $\approx 5.7 \times 10^4$ and 6.7×10^4 respectively.

The tuning probe was then gradually lowered over one of the resonators and the raw experimental data

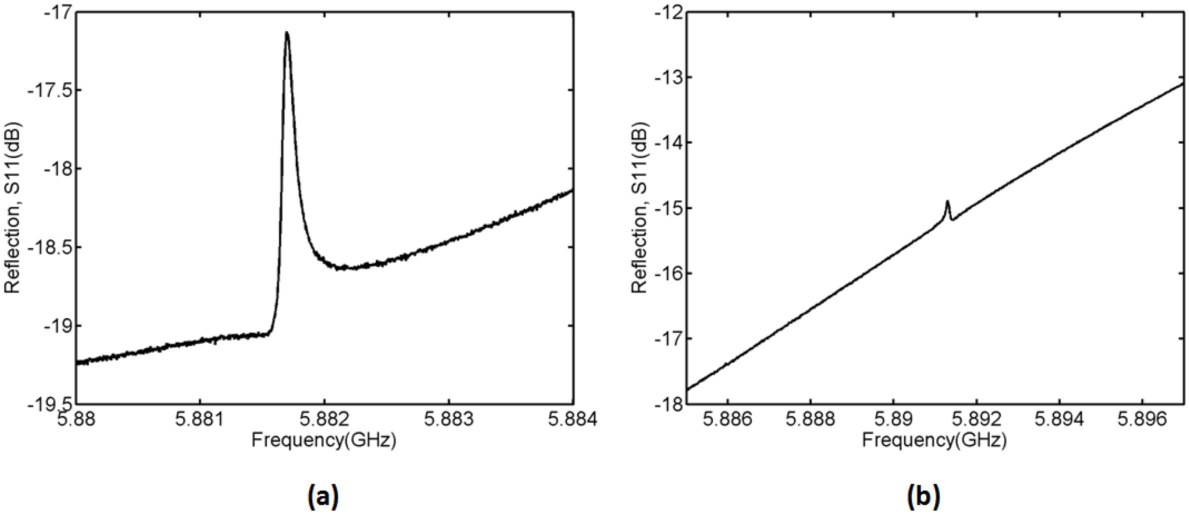

Figure 5.15: Reflection measurement on sample 6 showed unequal dips/peaks at f_{lower} in (a) and f_{higher} in (b), which indicated that the resonators were away from the avoided crossing.

obtained for the lower and higher frequencies is shown in fig. 5.16. All points at which the data crosses a horizontal line in fig. 5.16 correspond to the same distance of the tuning disc from the sample. Large variations in the frequencies were observed, which were periodic in the number of turns and, hence, resulted from a slight inaccuracy of the manufacturing process, to which the results were extremely sensitive. However, this *did not* affect the plots of splitting (Δf) versus the lower and higher frequencies in figs. 5.20, 5.21 and 5.23, where the variations were totally absent.

A minimum splitting in the frequencies was observed after 4 anti-clockwise turns of the tuning rod, and its value decreased from ≈ 9.7 MHz to ≈ 7.4 MHz. The transmission and reflection measurements on the resonators at the crossing position are shown in figs. 5.17 and 5.18. The deviation of the measured minimum splitting from the predicted value was pleasingly only $\sim 21\%$. This difference may reflect the accuracy of the COMSOL simulations to estimate the coupling capacitances or factors such as crosstalk, a tilt in the sample or a thin dielectric layer on the sample surface which affect the frequencies.

The circuit in fig. 4.2 was simulated in AIM Spice to estimate the shift in resonant frequencies as the inductance of the lower frequency resonator was decreased. The simulation parameters used at the avoided crossing are shown in table 5.1. The resonator lengths and the damping were adjusted to match with the measured values of frequencies and quality factors. The values of coupling capacitances were increased to match with the measured splitting and the peak/dip magnitudes.

The results of the simulation are shown in fig. 5.19. Although an independent determination of the change

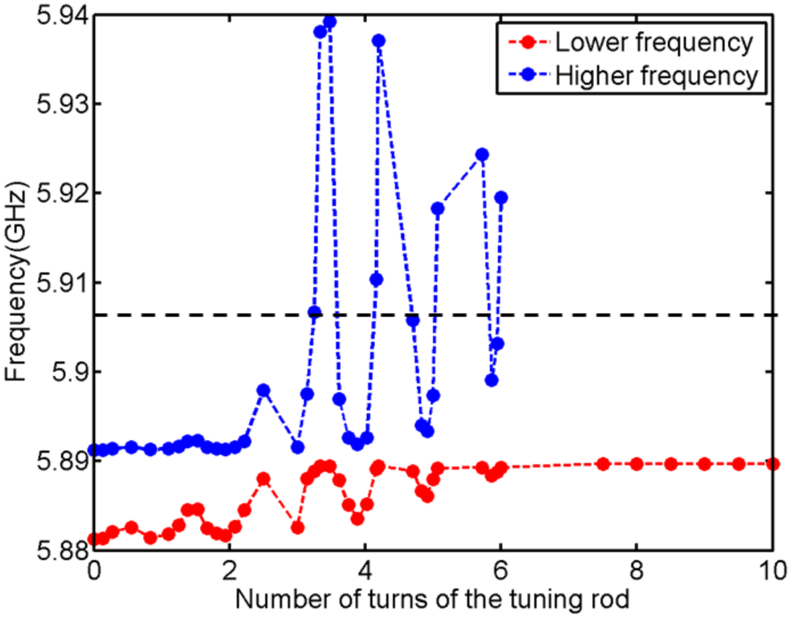

Figure 5.16: A shift in the resonant frequencies on sample 6 as the tuning probe approached the lower frequency resonator.

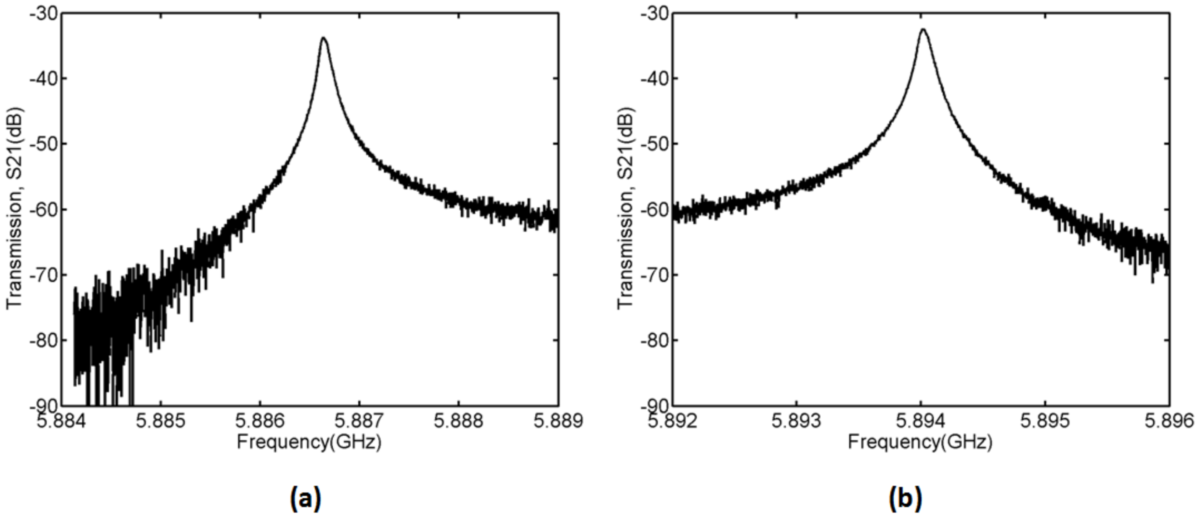

Figure 5.17: Two resonant peaks at f_{lower} = 5.8866 GHz in (a) and f_{higher} = 5.8940 GHz in (b) with a separation of ≈ 7.4 MHz at the avoided crossing in sample 6. The loaded quality factors of the resonances were 5.6×10^4 and 5.5×10^4 for f_{lower} and f_{higher} respectively.

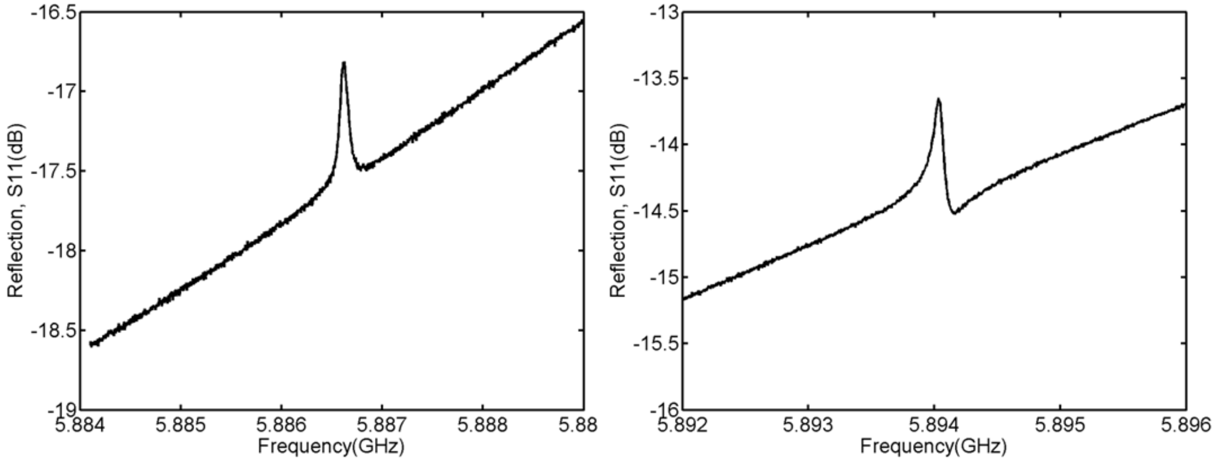

(a) **(b)**

Figure 5.18: Reflection data at the avoided crossing in sample 6, where the dips/peaks at f_{lower} in (a) and f_{higher} in (b) were ≈ equal in magnitude, confirming that the two resonators behaved as a single entity rather than two individual resonators.

Simulation Parameter	Fitted Value	Design Value
Length of resonator 1	1.0284×10^{-2} m	1×10^{-2} m
Length of resonator 2	1.0285×10^{-2} m	1×10^{-2} m
L/l of both resonators	Fixed parameter	4×10^{-7} H/m
C/l of both resonators	Fixed parameter	1.7×10^{-10} F/m
R/l of resonator 1	0.22 Ω/m	Variable parameter
R/l of resonator 2	0.16 Ω/m	Variable parameter
C_c	8.42×10^{-16} F	7.65×10^{-16} F
C_k	8.42×10^{-16} F	7.65×10^{-16} F

Table 5.1: Simulation parameters for sample 6 at the avoided crossing incorporated in AIM Spice.

in inductance could not be made, an equivalent comparison of the simulated and measured splitting in the frequencies showed good agreement as seen in figs. 5.20 and 5.21.

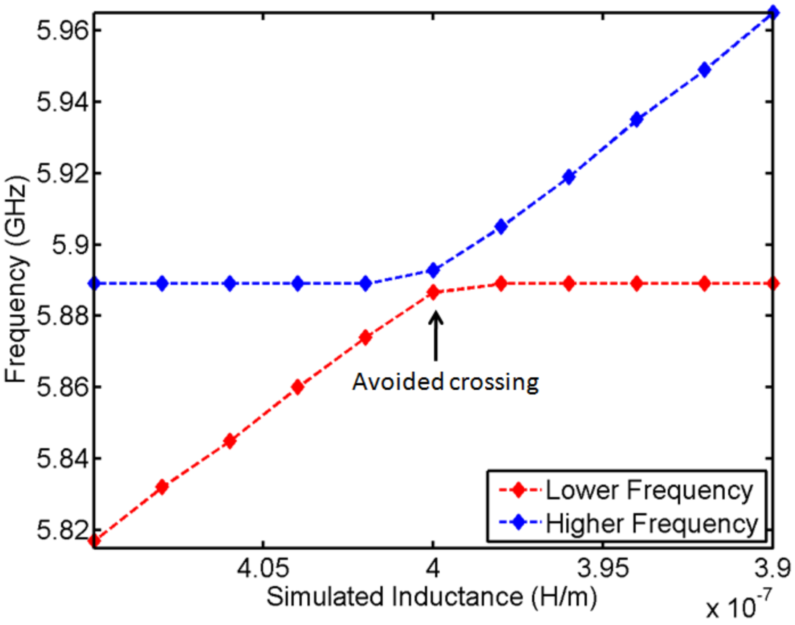

Figure 5.19: Simulated data for sample 6 showing a shift in the frequencies as the inductance per unit length of the lower frequency resonator was decreased from 4.10×10^{-7} H/m to 3.90×10^{-7} H/m. The splitting in the frequencies was a minimum of 6.1 MHz when both the resonators had identical resonator parameters.

The tuning of resonators through the avoided crossing was thus successfully achieved and could be implemented for other coupled resonator samples. The next sample (8, see table 4.1 for details) to be studied was one with a weaker coupling between the resonators, resulting in a smaller expected splitting in the frequencies. Initial transmission and reflection measurements on the sample showed that the tuning probe was above the lower frequency resonator, which was the desired way round. The splitting in the two frequencies when the tuning probe was raised as far as possible from the sample surface was $\approx$ 6.1 MHz, as shown in fig. 5.24. The minimum splitting predicted in AIM Spice for this sample was 1.1 MHz. The difference in the predicted and measured splitting indicated that the resonators were again away from the avoided crossing, and therefore tuning of the lower frequency resonator was required to measure the inherent minimum splitting in the frequencies.

The tuning probe was then gradually lowered and a minimum splitting of 2.5 MHz in the resonant frequencies as shown in fig. 5.26, was observed after 2 anti-clockwise turns of the tuning rod. Once again, there were large variations in the frequencies, but did not affect the plots of splitting versus the resonant

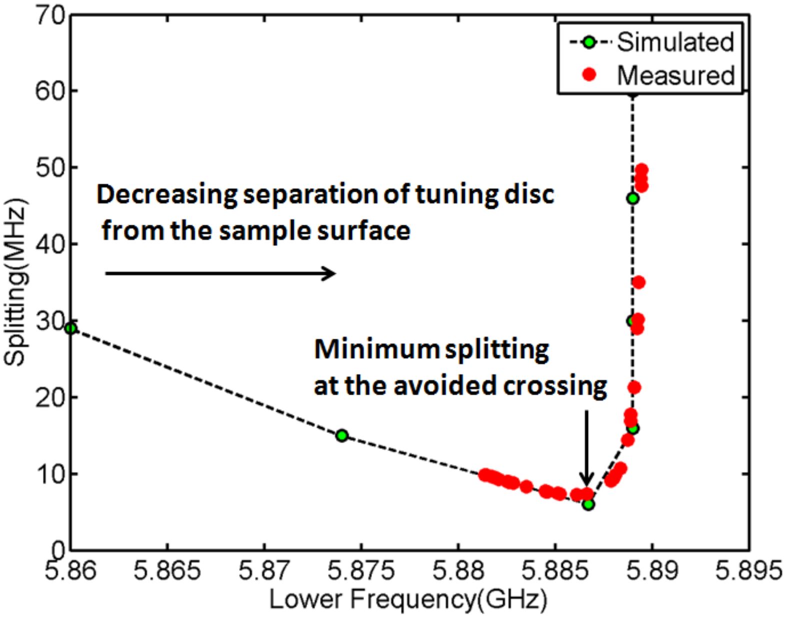

Figure 5.20: A comparison of the simulated and measured splitting versus the lower frequency in sample 6. The splitting in the frequencies was measured for a range of positions of the tuning probe as it approached the sample surface, i.e., as the lower frequency resonator was being tuned. The theoretical data was obtained from simulations in AIM Spice, as explained in the text. Clearly, there was a minimum in the splitting at the avoided crossing of the two frequencies where $\Delta f_{measured} \approx 7.4$ MHz and $\Delta f_{simulated} = 6.1$ MHz.

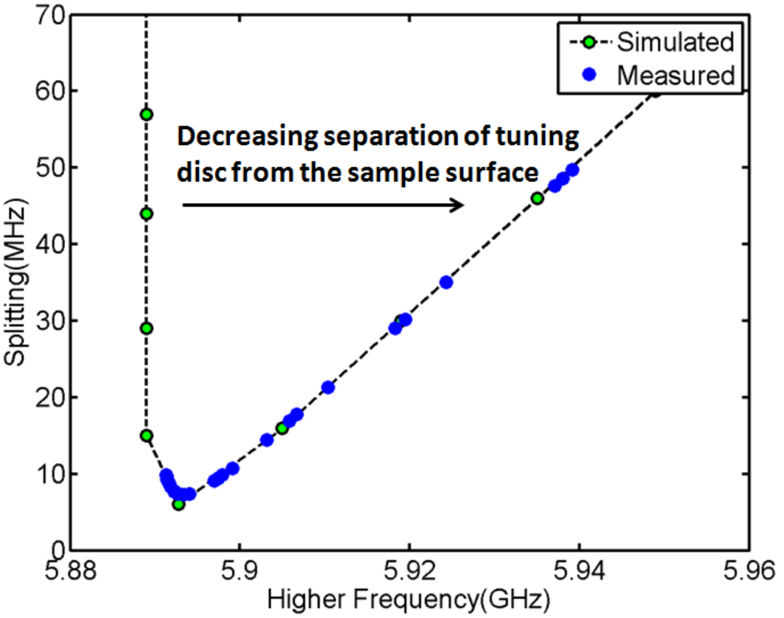

Figure 5.21: The simulated and measured splitting versus the higher frequency, as the lower frequency resonator was being tuned in sample 6. A minimum splitting at the avoided crossing was evident.

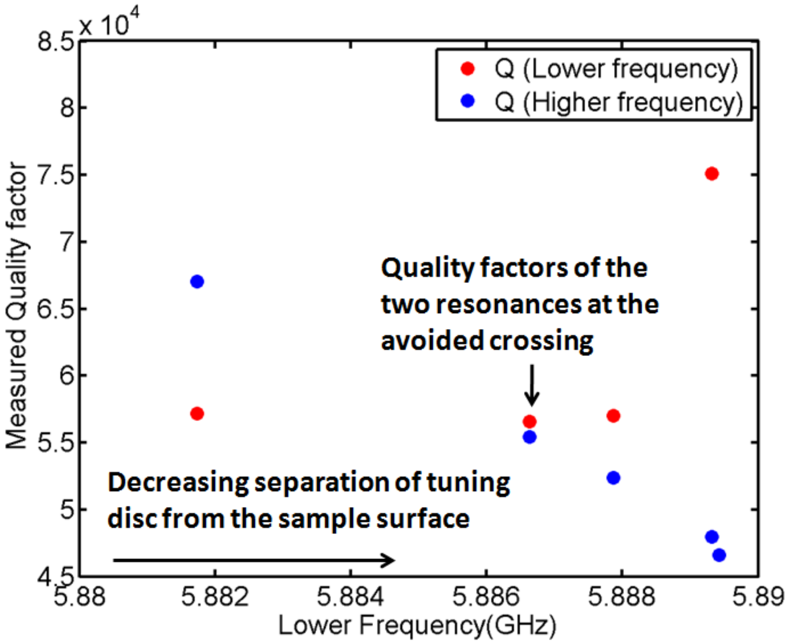

Figure 5.22: The variation of the measured quality factors as a function of the lower frequency in sample 6. The behaviour of the coupled resonators as a single entity is seen at the avoided crossing where the resonances have nearly the same quality factors.

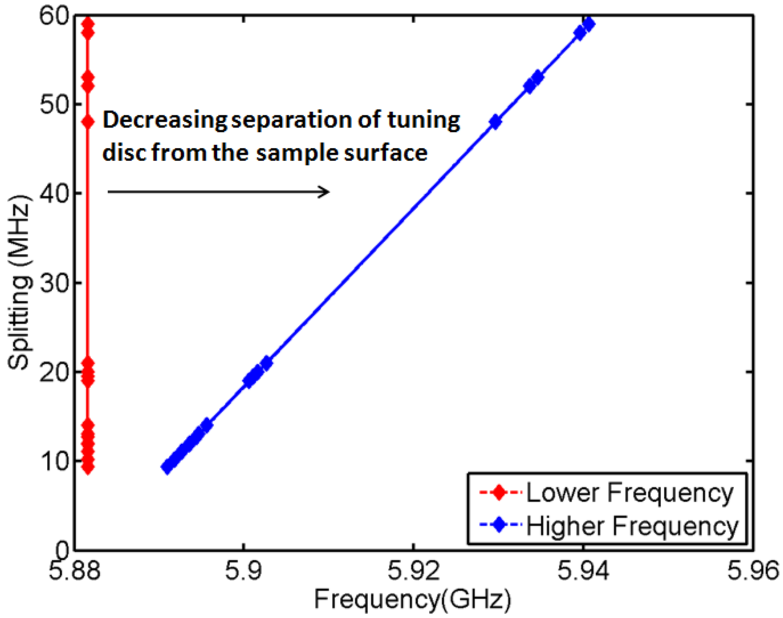

Figure 5.23: An increase in the splitting between the frequencies when the tuning probe was lowered over the *higher* frequency resonator on sample 6.

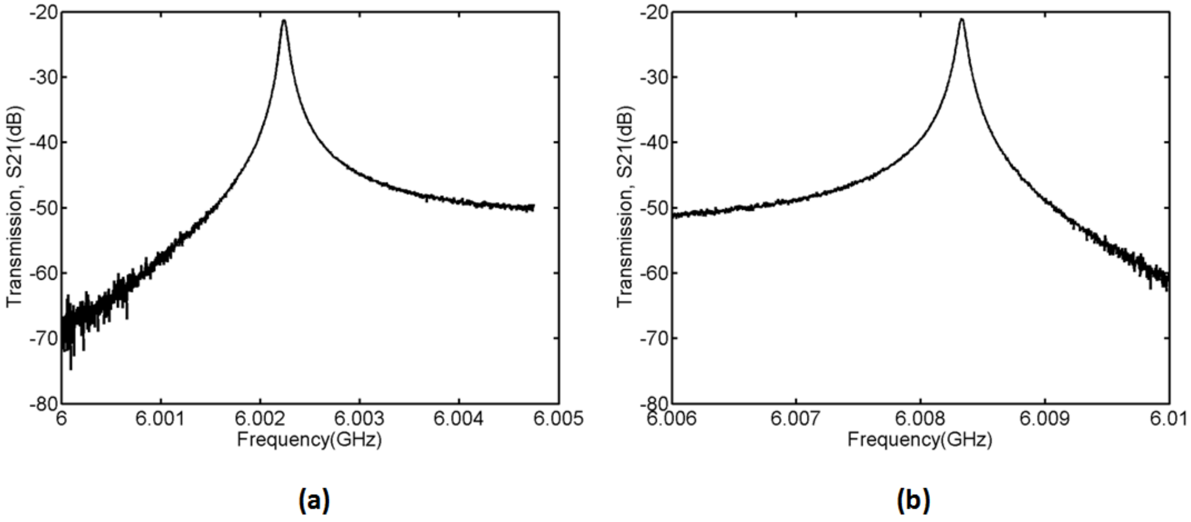

Figure 5.24: The resonant frequencies of coupled resonator sample 8 when the tuning probe was raised as far as possible from the sample surface were measured at $f_{lower} = 6.0022$ GHz in (a) and $f_{higher} = 6.0083$ GHz in (b). The loaded quality factors were $\approx 7.3 \times 10^4$ and 8.5×10^4 for f_{lower} and f_{higher} respectively and the splitting in the frequencies was measured as 6.1 MHz.

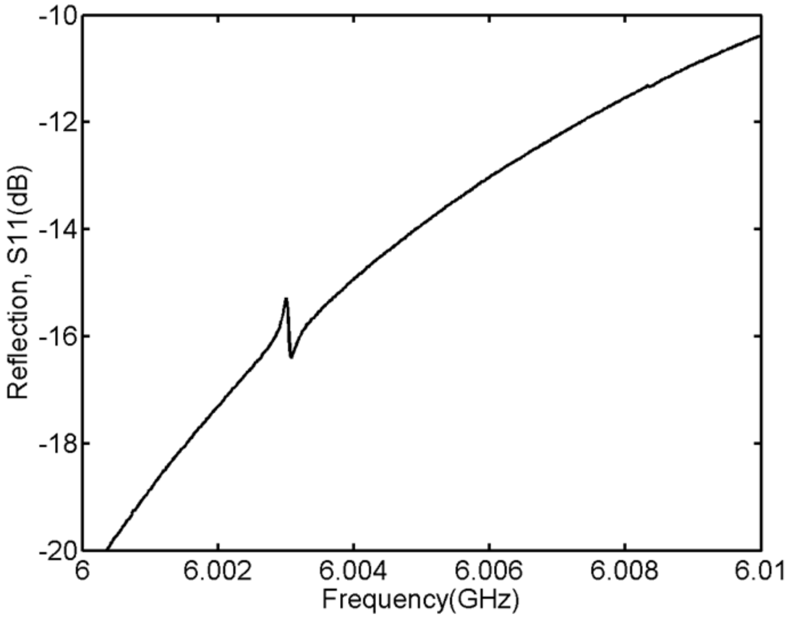

Figure 5.25: Reflection from the resonators in sample 8 when the tuning probe was raised to a maximum position above the sample. Due to being far from the avoided crossing where the coupling between the resonators was very weak, the absorption of microwave energy was greater in the resonator which was being driven.

frequencies as shown in figs. 5.28 and 5.29. The change in splitting with tuning of the lower frequency resonator was simulated using the circuit in fig. 4.2 and a comparison was made with the measured data in figs. 5.28 and 5.29. The parameters used for the simulation at the avoided crossing are listed in table 5.2. The resonator lengths, coupling capacitances, and the damping were adjusted to match with the measured frequencies, Δf, and the quality factors.

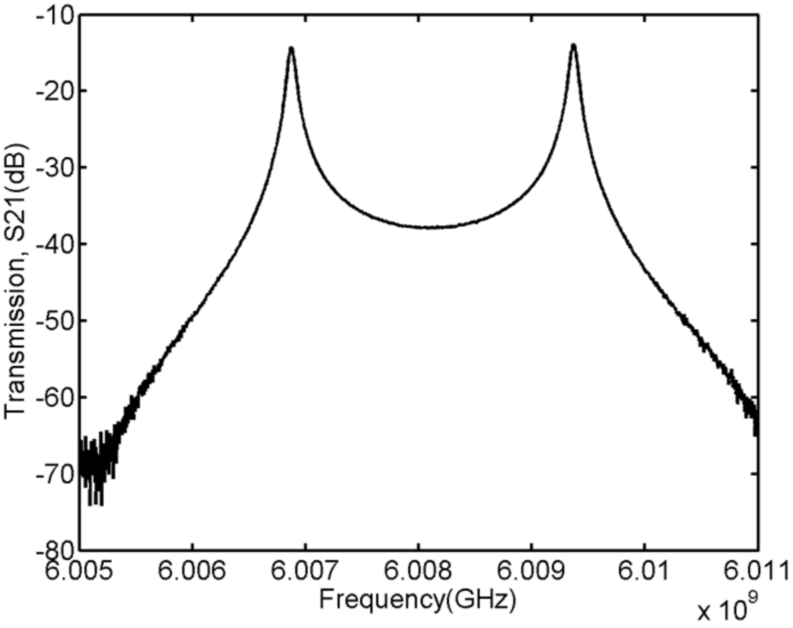

Figure 5.26: Measured transmission at the avoided crossing for sample 8, where $f_{lower} = 6.0068$ GHz and $f_{higher} = 6.0093$ GHz with loaded quality factors of $\approx 8.6 \times 10^4$ and 8.5×10^4 respectively and a splitting of ≈ 2.5 MHz.

Simulation Parameter	Fitted Value	Design Value
Length of resonator 1	1.00865×10^{-2} m	1×10^{-2} m
Length of resonator 2	1.00835×10^{-2} m	1×10^{-2} m
L/l of both resonators	Fixed parameter	4×10^{-7} H/m
C/l of both resonators	Fixed parameter	1.7×10^{-10} F/m
R/l of resonator 1	0.11 Ω/m	Variable parameter
R/l of resonator 2	0.12 Ω/m	Variable parameter
C_c	9.95×10^{-16} F	7.65×10^{-16} F
C_k	2.07×10^{-16} F	1.48×10^{-16} F

Table 5.2: Simulation parameters for sample 8 at the avoided crossing incorporated in AIM Spice.

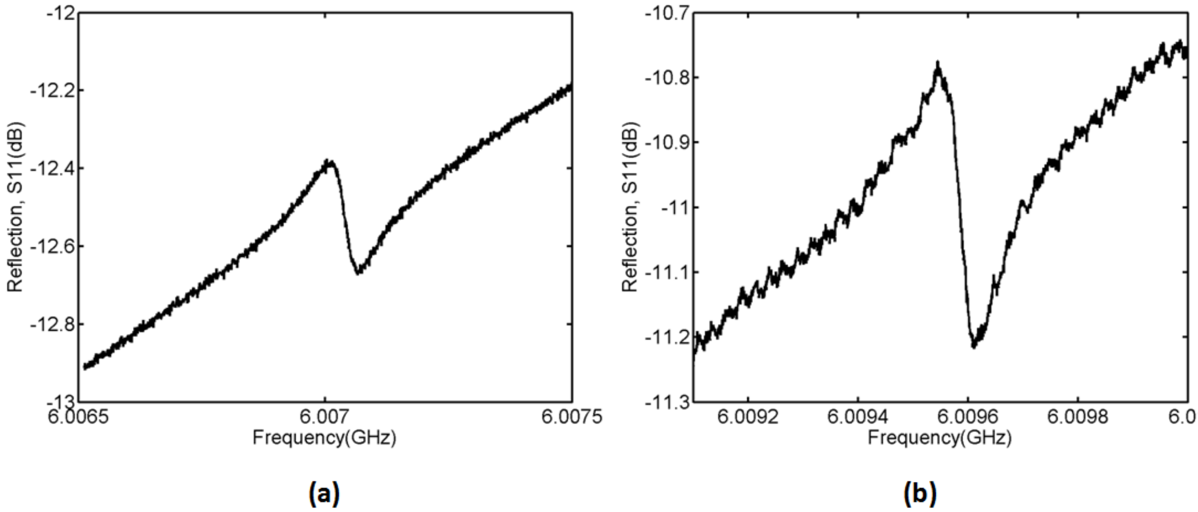

Figure 5.27: Measured reflection data from f_{lower} in (a) and f_{higher} in (b) measured at the crossing position in sample 8.

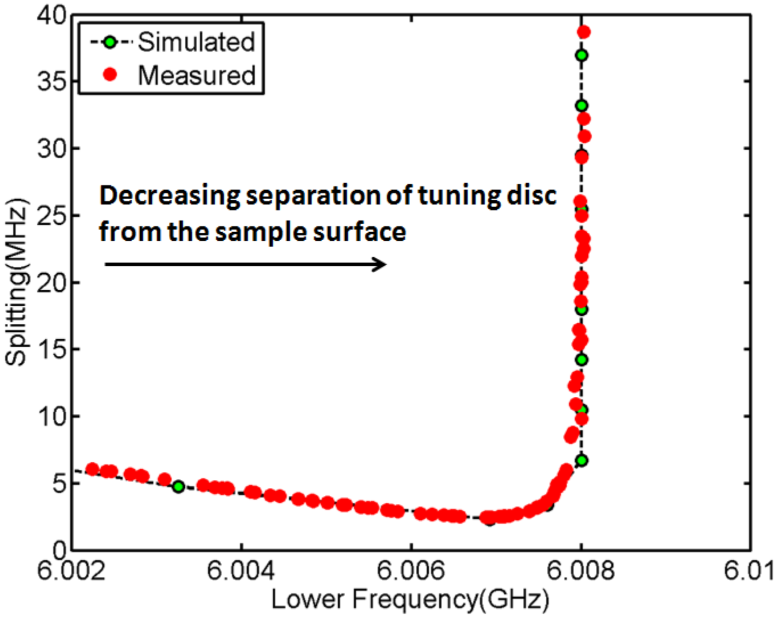

Figure 5.28: A comparison of the simulated and measured splitting versus the lower frequency in sample 8. The splitting in the frequencies was measured at several positions of the tuning probe as it approached the sample surface, i.e., as the lower frequency resonator was being tuned. The theoretical data was obtained from simulations in AIM Spice, as explained in the text. A minimum splitting at the avoided crossing of the two frequencies was seen where $\Delta f_{measured} = 2.5$ MHz and $\Delta f_{simulated} = 1.1$ MHz.

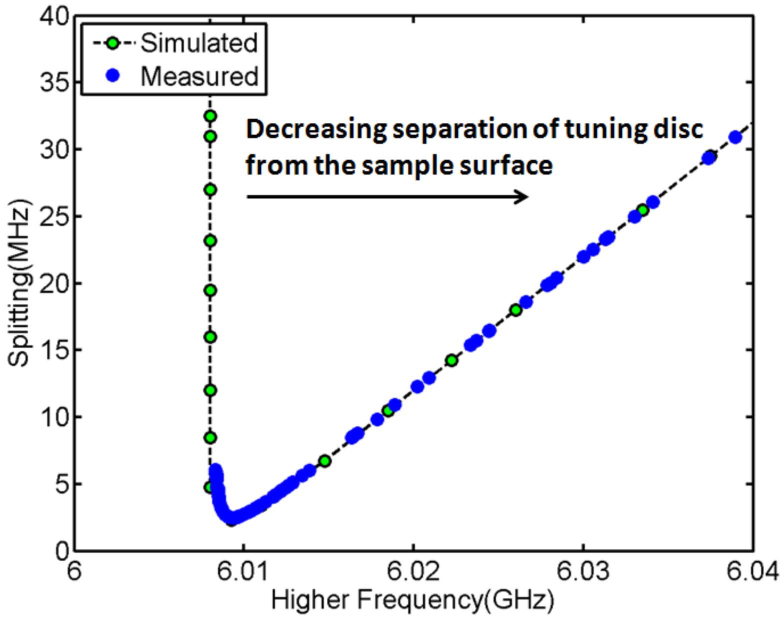

Figure 5.29: The simulated and measured splitting versus the higher frequency, as the lower frequency resonator was being tuned in sample 8. A minimum splitting at the avoided crossing was evident.

5.7 Conclusions

- The tuning of coupled resonator samples was very successful in that, the splitting as a function of the lower and higher frequencies showed clear evidence of an avoided crossing.
- The resonant frequency could be tuned by up to ≈ 50 MHz, which was more than sufficient for the proposed experiment to study electro-mechanical interactions.
- The measured quality factors and the reflection data at the avoided crossing showed that both the resonators on a sample behaved as a single entity, as expected.

CHAPTER 6

COUPLING OF MICROWAVE AND NANOMECHANICAL FREQUENCIES

The tuning of microwave resonators enabled the control and measurement of the inherent splitting in the coupled resonators at the avoided crossing. As shown in section 5.6, the splitting at the avoided crossing for a few samples was measured to be of the order of nanomechanical resonant frequencies (< 10 MHz). It was therefore possible, in principle, to study microwave-nanomechanical coupling in these samples, as suggested by the theoretical model in [4]. The initial sections of this chapter describe the proposed experiments and the measurement electronics required to investigate microwave-nanomechanical coupling. The theoretical analysis to guide the experimental observations is then provided. The results from preliminary experiments are presented and discussed in the final section of this chapter.

6.1 Proposed experiment with nanobars

The main purpose of working on a system of coupled microwave resonators was to study the effect of nanomechanical and microwave coupling at the avoided crossing in a more subtle way than for a single resonator as repeated in the literature [11], and observe its effect on the microwave resonant frequencies. The splitting at the avoided crossing for samples 6 and 8 was measured to be < 10 MHz, thereby enabling the coupling of a nanobar to one or both the resonators in these samples. It was proposed that initially, the effect of coupling a nanobar directly to only one of the resonators in the coupled resonator system as shown in fig. 6.1 would be studied. When the nanobar is driven, its oscillation changes the capacitance of the microwave resonator to which it is coupled, and hence the microwave resonant frequencies.

A measurement schematic in fig. 6.2 shows the electronics required to drive the resonators as well as to infer the effect of nanobar displacement on the microwave resonant frequencies. A high frequency signal

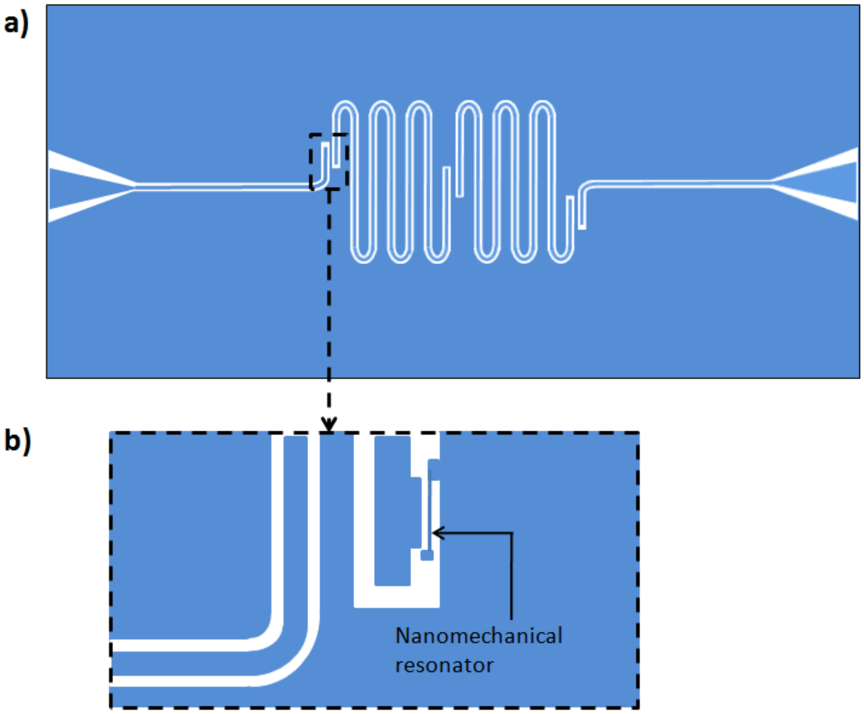

Figure 6.1: Schematic to show a nanobar coupled to one of the $\lambda/2$ microwave resonators. The width of the centre track of the microwave resonator is 10 μm and the distance from the adjacent ground planes is 5 μm. The proposed dimensions of the nanobar are 20 μm$\times$200 nm$\times$180 nm. To maximize coupling between the nanobar and the microwave resonator, it is fabricated close to a voltage anti-node of the microwave resonator.

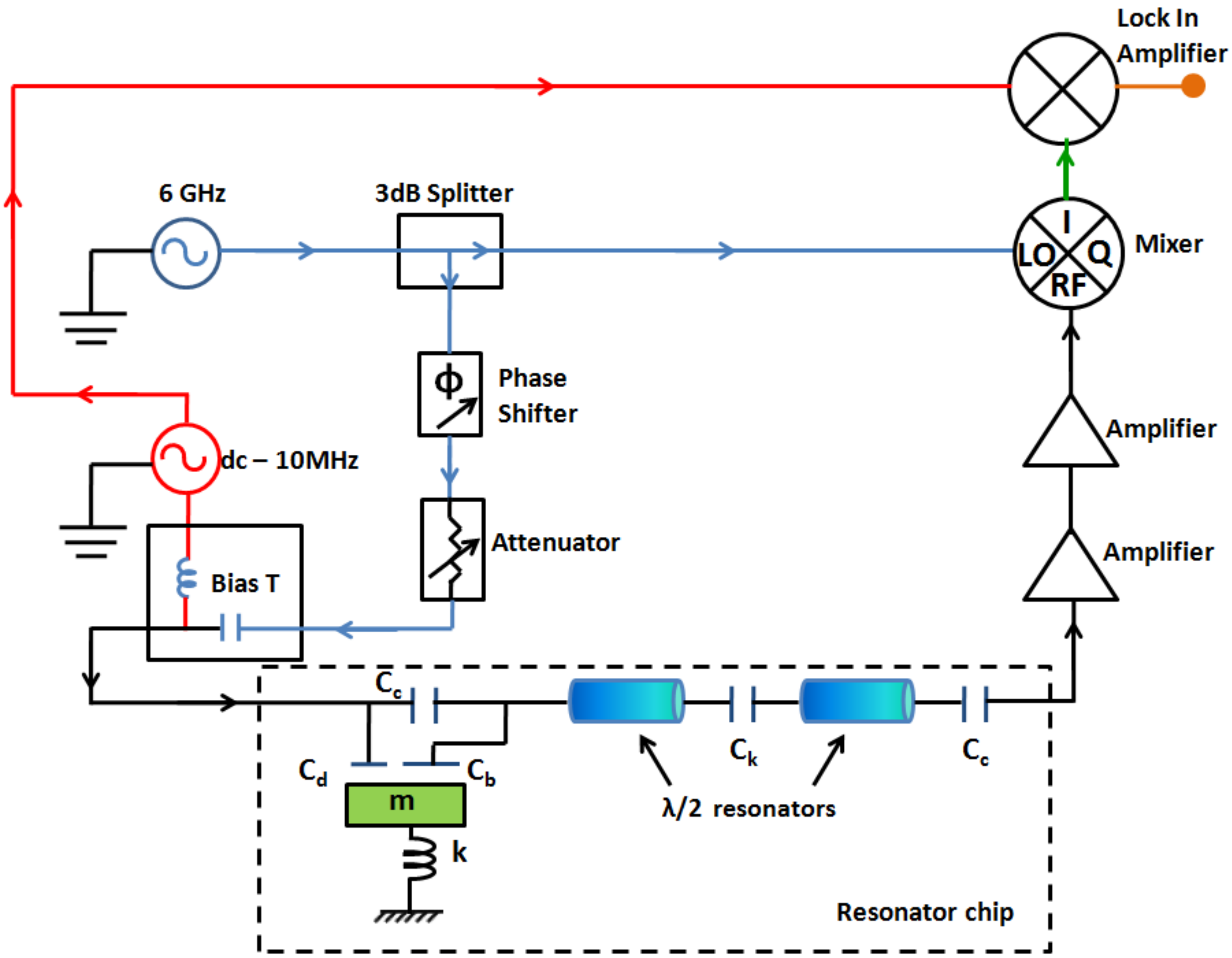

Figure 6.2: The measurement schematic to study microwave-nanobar interaction in a system of coupled microwave resonators. The design of the electronic circuit required for driving the resonators and measuring the transmitted signal was adapted from [11]. The coupling of a nanobar to one of the resonators is an approximate representation of a rather complex mechanism of capacitive coupling.

($\omega \approx 2\pi \times 6$ GHz) from a Rohde and Schwarz oscillator is coupled via C_c to the microwave resonators, and a low frequency signal ($\omega_1 \approx 2\pi \times dc - 10$ MHz) from a function generator is coupled to the nanobar through C_d. The transmitted signal from the resonators is amplified in multiple stages before it is measured.

Mechanical oscillations of the nanobar cause variations in the capacitance to ground C_b and hence, in addition to the response of the coupled resonators at frequency ω, the transmitted signal contains components at the following frequencies:

- $(\omega - \omega_1)$,(the lower sideband or LSB), and
- $(\omega + \omega_1)$, (the upper sideband or USB).

Further details on the additional components due to the perturbation (here, the oscillation of the nanobar) are discussed in section 6.3.

To demodulate and measure the dc levels proportional to the transmitted signal at frequencies ω, $\omega \pm \omega_1$ a mixer and a lock in amplifier (LIA) are incorporated in the measurement circuit in fig. 6.2. In the mixer, each component of the transmitted signal is multiplied by the high frequency reference signal ω and the output of the mixer therefore contains:

- a dc level obtained by multiplying two ac signals of the same frequency, ω,
- an ac signal at frequency ω_1, which is in-phase with the reference signal
- an ac signal at frequency ω_1, which is out of-phase with the reference signal
- higher frequency signals at $2\omega \pm \omega_1$, that are outside the frequency range of interest.

In order to obtain the dc level proportional to the in/out of-phase ac signals at frequency ω_1, the corresponding output signal from the mixer is fed to the input of a LIA, where it is multiplied by the low frequency reference signal (ω_1). The output of the LIA shows a dc level(V_{rms}) proportional to the corresponding in/out of-phase components of ω_1.

Thus the effect of varying the microwave frequencies by coupling to a nanobar could be measured. A more quantitative description of the transmitted signal from the resonators in the presence of a low frequency perturbation signal is provided in section 6.3.

The resonator samples with nanobars were to be provided by our collaborators but were not forthcoming due to difficulties in the final stages of the fabrication process. Therefore, it was decided that another experimental method, analogous to that proposed in this section could be performed to study the effect of varying the coupled resonator frequencies at their avoided crossing, as described in section 6.2.

6.2 Experiment with current-carrying coils

As an alternative to perturbing the resonator capacitance using a nanobar, the remaining section of this chapter describes an experiment to perturb the resonator inductance magnetically. Experimental work in the literature [9, 10, 58, 77, 79, 80, 83] has demonstrated that the kinetic inductance of superconducting coplanar microwave resonators is sensitive to an external magnetic field and can be used to tune their resonant frequencies. In our case, this could be achieved by placing a small current-carrying coil underneath the resonator. The theoretical model in [4] required that the perturbing frequency, (for example, the fundamental frequency of the nanobar or the frequency of the alternating magnetic field through the coils), be equal to the splitting frequency (Δf) of the coupled resonators. The advantages of using current carrying coils over nanobars for this purpose are:

- The frequency of the alternating magnetic field can be easily adjusted according to Δf in each of the coupled resonator samples, unlike the non-adjustable resonant frequency of a nanobar.
- Since the tuning of resonators through the avoided crossing is possible (as seen in section 5.6), the effect of the ac magnetic field on the coupled resonator frequencies can be explored across a wide range of Δf i.e., starting from a point where the frequencies are far apart, and further through the avoided crossing as shown in fig. 5.19.

6.2.1 Feasibility Study

In this subsection, it is briefly shown that the experiment with current carrying coils is indeed a feasible way to study the effect of perturbing the microwave resonant frequencies and to observe effects similar to the experiments with nanobars in [4]. It is explained in section 6.3 that in order to cause the fundamental resonant peaks to split, an ac magnetic field large enough to shift the peaks by a linewidth is sufficient. For example, a coil of radius 1 mm and 20 turns produces a field of ≈ 2 mT/A at a distance of 0.5 mm along its axis. In combination with a dc field, as shown in fig. 6.3, a shift in the resonant frequency of ≈ 1 MHz can be achieved by the small currents in the coil.

Bigger shifts in frequency could, in principle, be achieved by applying a larger magnitude of the field but this causes flux penetration into the resonators and hence non linearities in the resonant frequencies and a degradation of the quality factors [88, 89].

Due to a parabolic dependence of the frequency on a dc magnetic field, a total shift of $\approx (2 \times 1$ MHz/0.1 mT $) \times 2$ mT/A ≈ 40 MHz/A is expected due to the dc as well as the RF magnetic fields. If the loaded

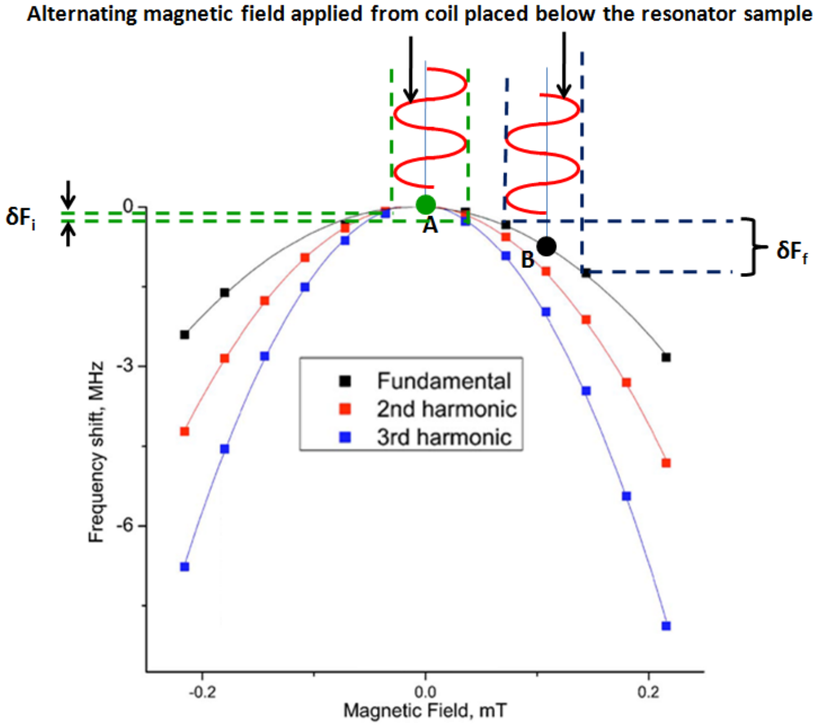

Figure 6.3: The magnetic field dependence of the resonant frequency of a coplanar resonator at 1.3 K is taken from [12]. The effect of a small ac field on the resonant frequency is enhanced by applying a uniform field to shift the working point to a point of greater slope on the parabolic curve.

quality factor of our 6 GHz resonator is, for example, $\approx 1 \times 10^5$, then its bandwidth is ≈ 60 kHz, and therefore a current of 10 mA through the small coil should be sufficient to produce a splitting in the peaks.

Prior to a discussion of the experimental set-up and results obtained from preliminary experiments with the coils, further insight is provided by a theoretical analysis of the system in the following section.

6.3 Theoretical predictions

Following many authors, a lumped element circuit is used to represent the coupled resonators system as shown in figs. 6.4a and 6.4b. As an aid to understanding, and to relate to the theory discussed in chapter 2, a mechanical analogue is used in the analysis and the direct correspondence to the components in the bulk electrical circuit is shown in fig. 6.4c and table 6.1.

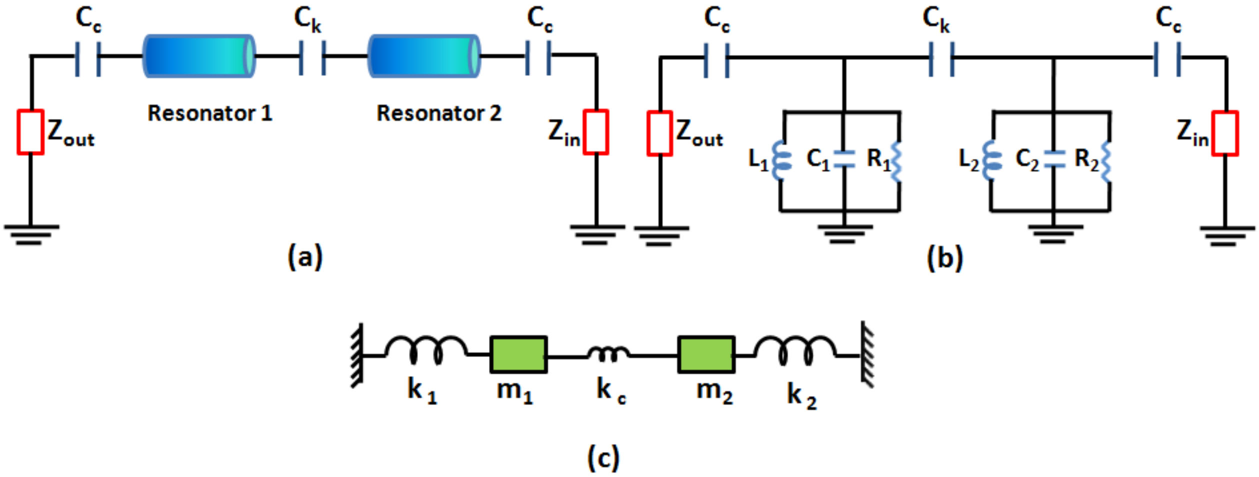

Figure 6.4: Coupled Oscillator Systems: (a) A system of identical, coupled, microwave resonators with the electrical parameters of inductance, capacitance and resistance distributed over their lengths. (b) A lumped element representation of the electrical circuit in (a). (c) A mechanical model analogous to the coupled resonators in (b).

Electrical		Mechanical
$1/L$	$\equiv$	m
C	$\equiv$	k
R	$\equiv$	$1/k_{damping}$

Table 6.1: Shows the equivalence of the bulk electrical and mechanical oscillator components. Here L, C, R correspond to the inductance, capacitance and resistance respectively of a bulk electrical oscillator and m, k, $1/k_{damping}$ are the mass, spring constant and the damping force constant of a mechanical oscillator.

Consider a system of coupled mechanical oscillators in which masses m_1 and m_2 are attached to springs of stiffnesses k_1 and k_2 respectively, as represented in fig. 6.4c. Let $m_1 = m_2$ and $k_1 = k_2 = k$ and the two masses be weakly coupled by a spring of stiffness $k_c \ll k$. Let mass, m_1 be driven by a force Fcos(ωt), so that displacements, x_1 and x_2 are observed in m_1 and m_2 respectively, in the presence of a damping force constant k_d. Then, the equation of motion for each mass is given by

$$m_1 x_1^{''} = F \cos \omega t - k x_1 - k_d x_1^{'} + (x_2 - x_1) k_c \tag{6.1}$$

and,

$$m_2 x_2^{''} = -k x_2 - k_d x_2^{'} + (x_1 - x_2) k_c \tag{6.2}$$

The details of the analysis and solutions to eqns. 6.1 and 6.2 are provided in appendix A.1.

The effect of varying the inductance of one of the coupled microwave resonators by applying an alternating magnetic field is then simulated. In the mechanical model, this is equivalent to varying the mass of one of the resonators in the following manner:

$$m_1 = m_{10} + b \cos \omega_1 t \tag{6.3}$$

where, b and ω_1 are the amplitude and frequency of the time varying perturbation signal and $\omega_1 \ll \omega$.

There are *two* limiting cases for the displacement $x_2(\omega, t)$ in the presence of a perturbation in mass m_1:

1. *low drive levels*, where a first order expansion for the drive and the output signals is possible, i.e.,

$$x_2(\omega, t) = x_{20}(\omega_0, t) + x_{21}(\omega_0, \omega_1, t) \tag{6.4}$$

   where $x_{20}(\omega_0, t)$ is the displacement in the absence of a perturbation in m$_1$ and x_{21} is the additional signal due to the perturbation and $x_{21} \ll x_{20}$.

2. *high drive levels*, where the solution is more complex and requires several approximations.

The expression for the displacement x_2 in eqn. 6.4 is analogous to a change in transmitted microwave power, S21 as a result of varying the inductance of the resonator that is driven by the microwave signal.

It is this latter case that is relevant to the predictions in [4], since we seek to observe a splitting in the two resonant peaks for high drive levels. This clearly cannot be done with a low drive level, which only results in additional peaks at frequencies $(\omega \pm \omega_1)$, also known as the sidebands. The low amplitude limit has not, however, been previously considered and therefore is of some interest. A description of the analysis is presented in the following text. The codes for the analysis in both limits were written in MATLAB [71] and where necessary, edited and modified by the author. The programs were then used to study the expected behaviour of the real experimental system in both the limits:

1. **Low amplitude perturbation**:

   When both the low frequency perturbation and the resulting change in the output are small, the expected output can be derived explicitly. Details of the analysis are provided in appendix A.1, but briefly, it is assumed in eqns. 6.3 and 6.4 that $b \ll m_{10}$ and $x_{21} \ll x_{20}$ at all drive frequencies of interest.

   Substitution into the equations of motion and cancellation of terms in m_{10} and x_{20} leave us with an equation of motion for x_{21} which contains only terms with frequencies $(\omega + \omega_1)$ and $(\omega - \omega_1)$, called the upper and lower sidebands (USB, LSB). The total output of the real experiment therefore is expected to contain:

   - the x_{20} term, which has peaks at the fundamental frequencies of the coupled resonators, i.e., at $\omega = (\omega_{0lower}, \omega_{0higher})$
   - the x_{21} term, which contains peaks due to the very small, LSB and USB terms.

   It is seen in fig. 6.2 that this total output signal is multiplied by the high frequency reference signal ω in the mixer. The output of the mixer therefore contains a dc component due to the fundamental at ω and an ac signal at frequency ω_1 due to the sidebands.

   The phase shifter is then used to obtain an output signal from the mixer which is in-phase with the reference signal, ω. Therefore, in the bad cavity limit ($\omega_1 \ll \frac{\omega}{Q}$), this gives maximal sensitivity to the drive at ω_1 and, in all cases, it minimizes the dc level due to the fundamental. Finally, the in-phase component of the output signal is demodulated by the LIA to provide a dc level proportional to the magnitude of the signal at ω_1.

   At the avoided crossing, the parameters used for the simulations are: $m_1 = m_2 = 1$ kg; $k = 1$ N/m and therefore $\omega_{0lower} = 1$ rad/s. To compare with the effects of a perturbation on a system of microwave resonators, realistic values of splitting in the frequencies and their damping were used: the coupling constant $k_c = 5 \times 10^{-4}$ N/m was used to obtain $\omega_{splitting} = 5 \times 10^{-4}$ rad/s (≈ 3 MHz at the microwave frequencies), and hence $\omega_{0higher} = 1.0005$ rad/s. The damping force constant in the resonators was set to $k_d = 1 \times 10^{-5}$ N-s/m to simulate a quality factor of 1×10^5 in the microwave resonators. In fig. 6.5, the expected output signals from the *mixer* in the presence of a perturbation $b\cos(\omega_1 t)$, for a fixed b, and ω_1 ranging from zero to the splitting frequency, are shown. It should be noted here that the plots in fig. 6.5 show the displacement term x_{21} as a function of the drive frequency, ω.

Comments on the simulated plots in fig. 6.5:

Mathematically, it is seen that each sideband component in x_{21} is proportional to the product of two terms: $\omega \times (\omega - \omega_1)$ (the USB term) and $\omega \times (\omega + \omega_1)$ (the LSB term). Hence for each value of the sweep frequency ω, the total signal in x_{21} is a sum of the LSB and USB terms, which results in peaks at the following frequencies:

- $\omega = \omega_{0lower}$,
- $\omega = \omega_{0lower} \pm \omega_1$,
- $\omega = \omega_{0higher}$,
- $\omega = \omega_{0higher} \pm \omega_1$.

The quality factors of the sideband peaks in x_{21} are the same as in the peaks at $\omega = (\omega_{0lower}, \omega_{0higher})$ in x_{20}. As ω_1 is increased, the amplitudes of the peaks at all the three frequencies decrease except for the case when $\omega_1 = \omega_{splitting}$ where the amplitudes of the peaks at $\omega = \omega_{0lower}, \omega_{0higher}$ rise due to an overlap of one of the sideband peaks.

- In fig. 6.5a, $\omega_1 = 1 \times 10^{-5} <$ a linewidth of the fundamental resonances, also known as the *bad cavity limit*. Here, the sidebands at $\omega = (\omega_{0lower} \pm \omega_1)$ and $\omega = (\omega_{0higher} \pm \omega_1)$ are present, but are not visible as they lie within the bandwidth of the peaks at ω_{0lower} and $\omega_{0higher}$ respectively.
- In figs. 6.5b and c, as the value of ω_1 is increased, the peaks at $(\omega_{0lower} \pm \omega_1)$ and $(\omega_{0higher} \pm \omega_1)$ move further away from the corresponding peaks at ω_{0lower} and $\omega_{0higher}$, into the *good cavity limit*, and there is a drop in their amplitudes.
- In fig. 6.5d, $\omega_1 = 2.5 \times 10^{-4} = \frac{\omega_{splitting}}{2}$. In this case, the USB of ω_{0lower} and the LSB of $\omega_{0higher}$ overlap, but are opposite in phase, hence get almost cancelled and only one of the sideband peaks of ω_{0lower} and $\omega_{0higher}$ are visible.
- In fig. 6.5e, $\omega_1 = \omega_{splitting}$, is a special case, where the USB of ω_{0lower} coincides with the peak at $\omega_{0higher}$ and the LSB of $\omega_{0higher}$ coincides with the peak at ω_{0lower}. Hence, the amplitudes of the peaks at ω_{0lower} and $\omega_{0higher}$ increase, but to only half the value of the peak height when $\omega_1 = 0$. The amplitude variation of ω_{0lower} in fig. 6.5 as a function of ω_1 is shown in fig. 6.6.

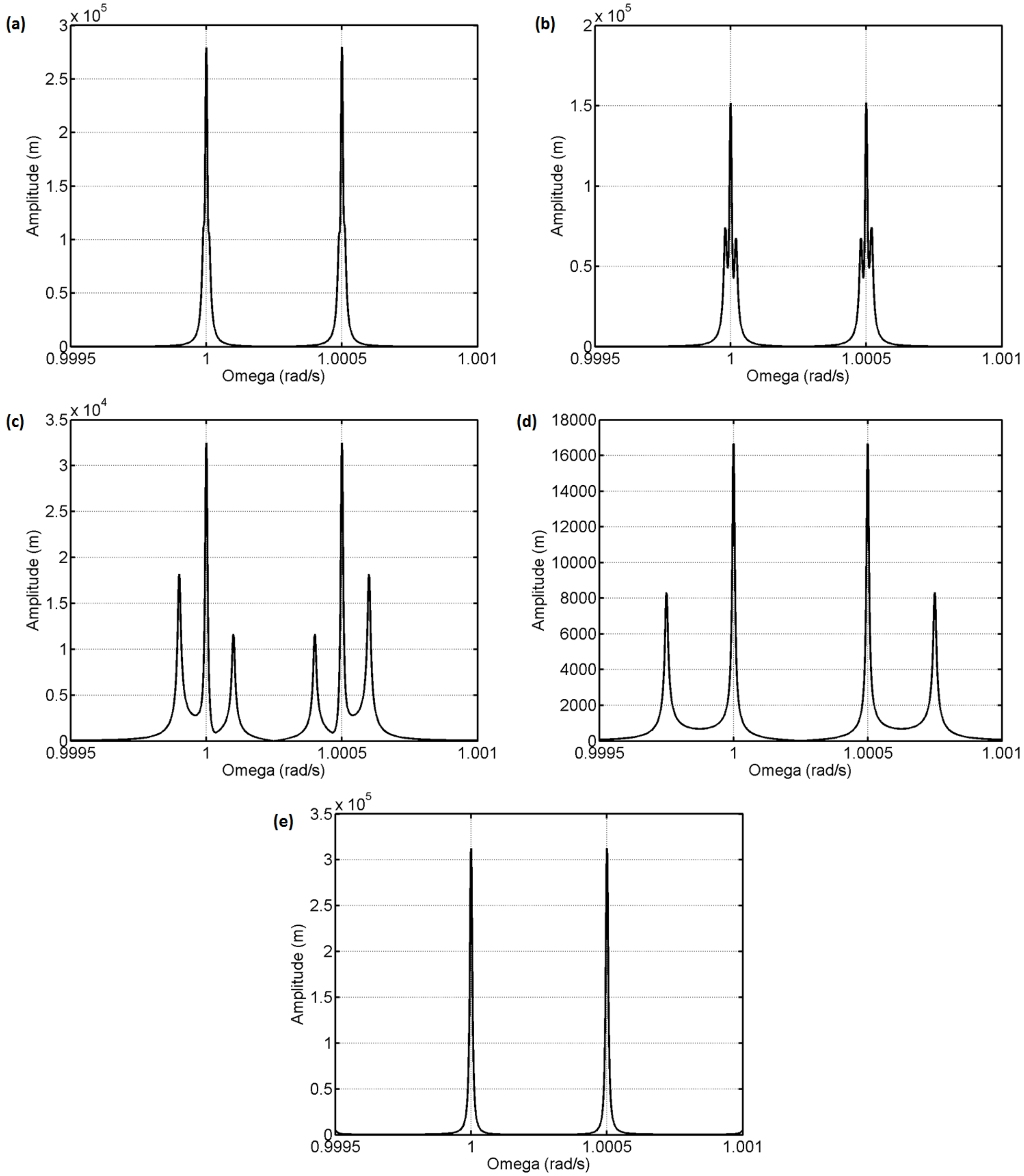

Figure 6.5: The displacement x_{21} as a function of the high frequency reference signal, ω. Here $\omega_{splitting} = 5\times10^{-4}$ and a fixed value of $b = 1$. (a) $\omega_1 = 1\times10^{-5}$, (b) $\omega_1 = 2\times10^{-5}$, (c) $\omega_1 = 1\times10^{-4}$, (d) $\omega_1 = 2.5\times10^{-4}$ (e) $\omega_1 = 5 \times 10^{-4} = \omega_{splitting}$.

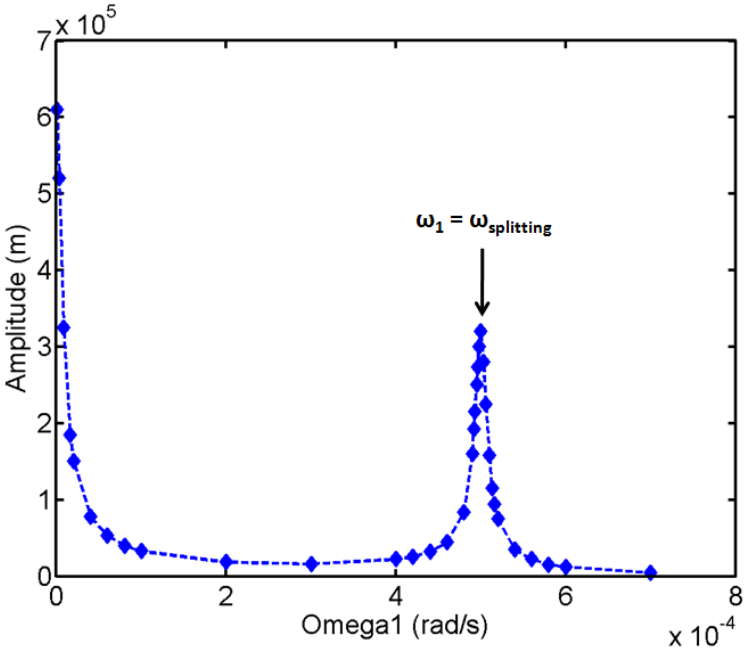

Figure 6.6: Variation of the peak amplitude at $\omega = \omega_{0lower}$ in x_{21} as a function of the perturbation signal frequency ω_1.

Thus, the coupled mechanical resonators system in the presence of a small amplitude of a perturbation signal $b\cos(\omega_1 t)$ was analysed to provide insight into the real experimental system with microwave resonators.

2. **Large amplitude perturbation:**

When the amplitude of the perturbation and the resulting output signals are large, there is no simple solution. It is in this limit that a splitting in the fundamental frequencies is expected to be observed when $\omega_1 = \omega_{splitting}$.

Therefore a different approach of analysing this case was taken. Again using the mechanical analogue, the displacement x_2 (equivalently, the output voltage) could be determined by a finite difference numerical integration method. The driving force on m_1 was set as Fcos(ωt) and t is increased in a series of small steps. At each step the acceleration of m_1 is calculated, and hence its new velocity v_1 and new position x_1. This in turn induced an acceleration in m_2 and therefore a new velocity and position. Simultaneously, the mass $m_1 = m_{10} + b\cos(\omega_1 t)$, is set, as with the low amplitude analysis. This process is repeated and it is found that, around ten increments per oscillation period of the drive frequency, ω is sufficient to produce a stable output. The simulation is then carried out for a sufficiently long time to be clear of the transient solution and the rms amplitude is averaged over a few thousand cycles to produce a dc signal.

In fig. 6.7, the simulated frequency response of the *total output signal* x_2 as a function of ω is plotted, unlike in fig. 6.5 where only the perturbed component x_{21} was plotted. Following are the parameters used in the simulations: $m_1 = m_2 = 1$ kg; $k = 1$ N/m ; $k_c = 0.05$ N/m , $k_{damping} = 1 \times 10^{-4}$ N-s/m. These parameters result in $\omega_{0lower} = 1$ rad/s , $\omega_{0higher} = 1.05$ rad/s, $\omega_{splitting} = 0.05$ rad/s and quality factor $\approx 10^3$. It should be noted here that no approximations are made to the output signal x_2 and the quality factors were limited to small values to decrease the time taken for the computation.

The following features are noted from the results of the theoretical analysis:

- In fig. 6.7b, $\omega_1 < \omega_{splitting}$, the sidebands of ω_0 are seen, as with the low amplitude perturbation case.
- In figs. 6.7c → f, $\omega_1 = \omega_{splitting}$ for increasing values of b. A comparison of the plots in figs. 6.7c and d shows that the amplitude of the perturbation $b = \frac{10}{Q}$kg to first observe a splitting of the fundamental peaks at ω_{0lower} and $\omega_{0higher}$. It is assumed that this is true for resonators with a large Q, such as the microwave resonators in our experiments.
- In figs. 6.7e and 6.7f, the splitting in the fundamental peaks increases with increase in the amplitude of the perturbation signal.

It should be noted that this case is different from the small amplitude perturbation limit where an increase in b does not cause the fundamental peaks to split, but only increases the amplitudes of the sideband peaks in direct proportion to b.

The theoretical analysis in this section provided a basic understanding of the effect of a low frequency perturbation signal on a system of coupled mechanical oscillators. A similar response from the coupled microwave resonators is expected to be observed when the inductance of one of the resonators is varied by an alternating magnetic field ($\omega_1 \approx dc - 5$ MHz), applied from a small coil placed below one of the resonators on the chip. In the following section, the experimental set-up with the coils and the measurement circuit to infer the effect of an ac magnetic field on the resonant frequencies are described.

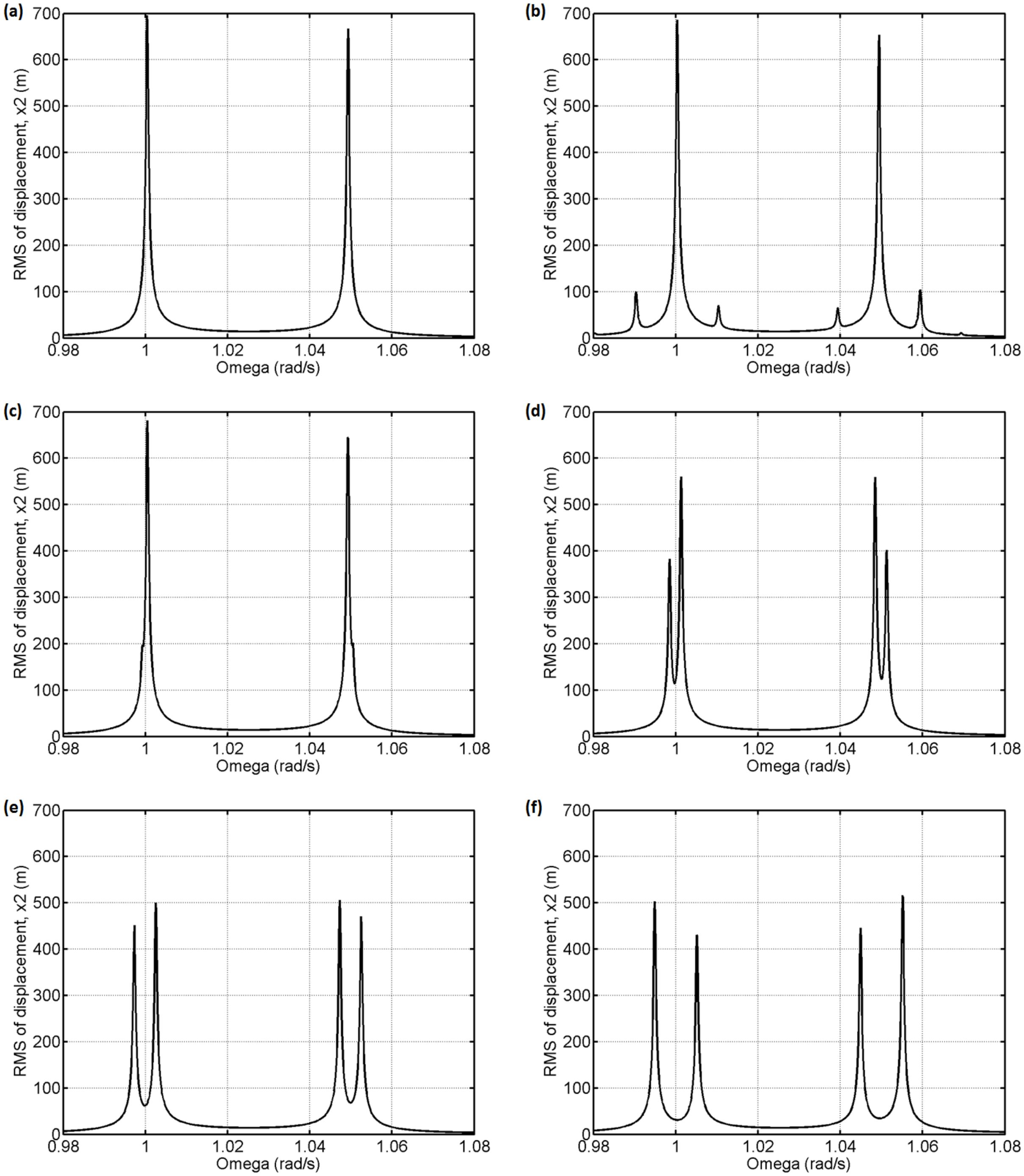

Figure 6.7: The displacement x_2 as a function of the driving frequency ω. Here $\omega_{splitting} = 0.05$ rad/s, and the quality factor of both the oscillators $\approx 10^3$. (a) The absence of a perturbation, i.e., $b = 0$; $\omega_1 = 0$, (b) $b = 0.01$; $\omega_1 = 0.01$. The plots in (c) → (f) are for $\omega_1 = \omega_{splitting} = 0.05$, but for increasing values of the perturbation amplitude, b, i.e., in (c) $b = 0.002$, (d) $b = 0.01$, (e) $b = 0.02$ and (f) $b = 0.04$.

6.4 Experimental set-up with the coils

A sample that enabled tuning of the resonators with a magnetic field was fabricated using lithographic methods described in section 3.2, and wirebonded to the copper PCB as shown in fig. 4.7. The copper cavity was fitted to the bottom of the cryostat as shown in fig. 5.13. Two current carrying coils were fitted to the base of the copper cavity as shown in fig. C.2 so that the effect of varying the inductance of either of the microwave resonators on the sample could be studied.

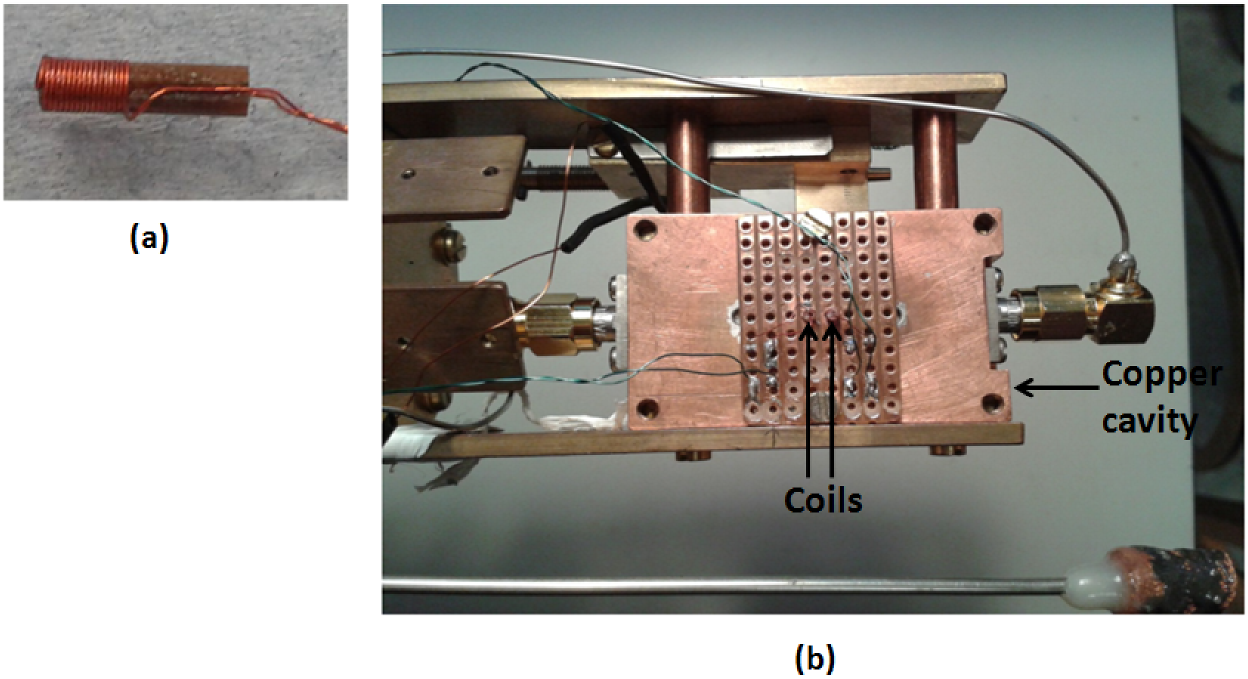

Figure 6.8: (a) Shows the coil used in the experiments to vary the inductance of the microwave resonators. (b) Shows two coils of diameter 1.45 mm fitted through the base of the copper cavity and the PCB so that they could be positioned below the resonators on sample.

The coils were made from copper wire wound on tufnol cores that were 3.5 mm long and 1.45 mm in diameter, and produced a field of ≈ 1.8 mT/A at a distance of 0.5 mm along their axes. Holes were drilled through the base of the copper cavity as well as the PCB so that the coils could be placed in contact with the back of the resonator chip. To maximize the effect of the ac field on the resonant frequencies, a uniform dc field was applied to the resonators from a pair of Helmholtz coils placed outside the cryostat. The role of the dc field was to bias the microwave resonant frequencies as shown in fig. 6.3, and increase the sensitivity to the smaller ac field.

However, due to the sample enclosure used in this experiment, a large frequency shift as reported in [9] was not expected when an external dc field was applied. This was because the PCB was soldered to the base of the copper cavity with indium-tin solder, which is superconducting at our operating temperature of 1.3 K and therefore reduces the effect of magnetic flux on the microwave resonant frequencies. But, even a small effect of the bias dc field on the resonators would aid a bigger response due to a quadratic dependence of the resonant frequencies on a uniform magnetic field.

A schematic of the measurement electronics to carry out the experiment with the coils is shown in fig. 6.9. It is largely similar to the measurement circuit for the proposed experiments with nanobars in fig. 6.2. A microwave signal ($\omega \approx 6$ GHz) is generated by a Rohde and Schwarz high frequency oscillator and is coupled to the microwave resonators by C_c. A low frequency alternating current ($\omega_1 \approx dc - 5$ MHz) from a function generator is passed through one of the coils to generate an alternating magnetic field. The transmitted signal from the resonators contains components at three frequencies: ω, $(\omega - \omega_1)$(LSB), and $(\omega + \omega_1)$ (USB). To demodulate and measure the amplitude of the transmitted signal at all the three frequencies, a mixer and a lock in amplifier (LIA) are included in the circuit. In the mixer, the transmitted signal is multiplied by the high frequency signal ω, resulting in dc levels due to the fundamentals, and ac signals at frequency ω_1, which are in/out-of phase with the the reference signal ω. To obtain a dc level proportional to the in/out-of phase components, the corresponding output signal from the mixer is fed to the input of a LIA, where it is multiplied by the low frequency signal ω_1. The output of the LIA shows the dc level (V_{rms}) proportional to the corresponding in/out-of phase ac signal of frequency ω_1. In the following section, the results obtained from experiments with the coils are presented and discussed.

6.5 Preliminary Results and Discussion

Low temperature measurements to observe the effect of perturbing a coupled microwave resonator system (on sample 9, see table 4.1 for resonator parameters) with an alternating magnetic field were made in a cryostat where the sample stage was enclosed in a vacuum can. The sample was wire bonded to a copper PCB, enclosed in a copper cavity and mounted on the cryostat. The tuning probe was assembled and lowered over the lower frequency resonator on the sample using the procedure described in section 5.5. The current-carrying coils were fitted through holes drilled in the base of the copper cavity and PCB, so that they were as close as possible to the resonator chip. The copper wires on the coils were soldered to coaxial cables on the cryostat thereby enabling an alternating current from an external source to be passed through the coils. The sample stage in the cryostat was cooled to 1.3 K by pumping on the 1 K pot enclosed within the vacuum can.

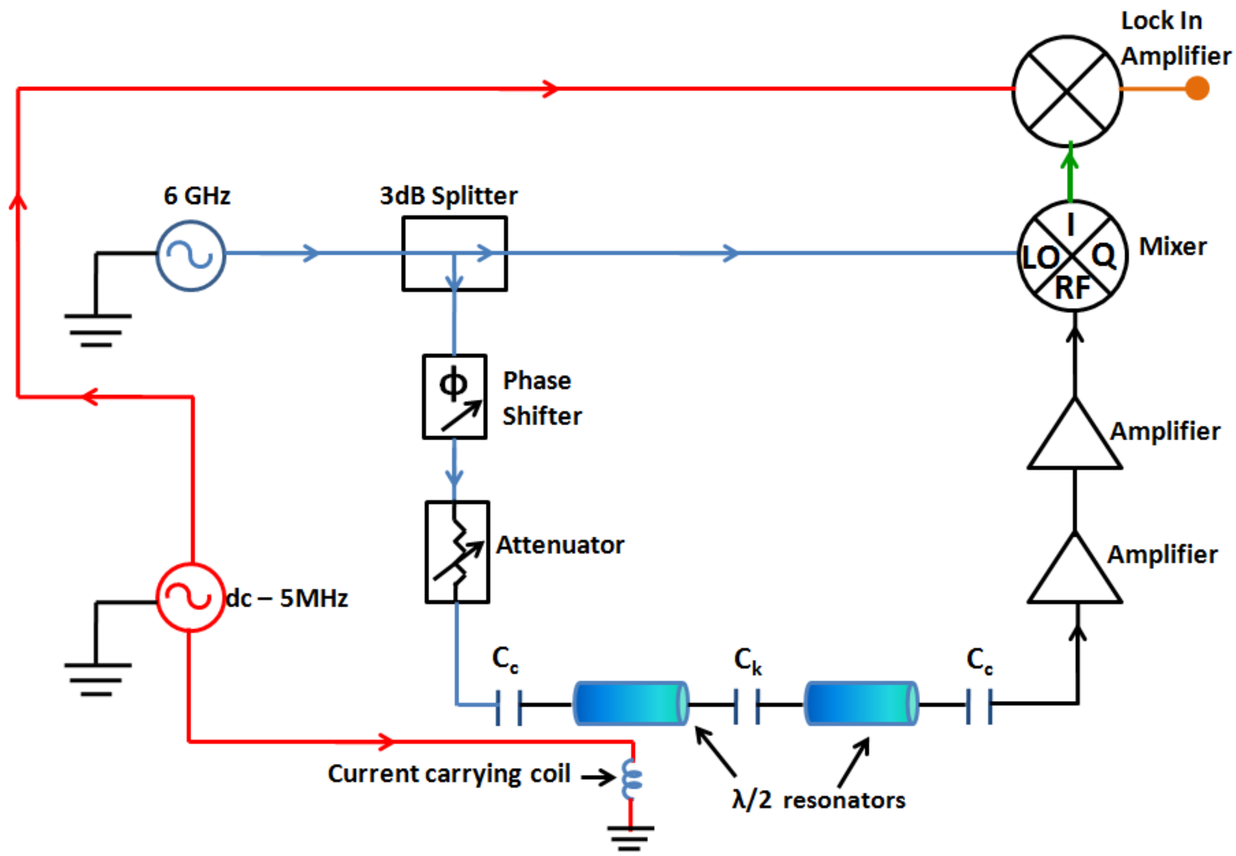

Figure 6.9: A schematic of the electronic circuit used for experiments to study the effect of varying the inductance of one of the microwave resonators with an alternating magnetic field.

Initial measurements on sample 9 enabled the identification of its two fundamental frequencies using a network analyser (NA). When the sample was measured, lowering the tuning disc indicated that the resonators were already at their optimal avoided crossing. Therefore, the tuning probe was left in the position where the distance between the tuning disc and the sample was a maximum. The transmission of microwave power from the two resonators was then recorded as shown in fig. 6.10.

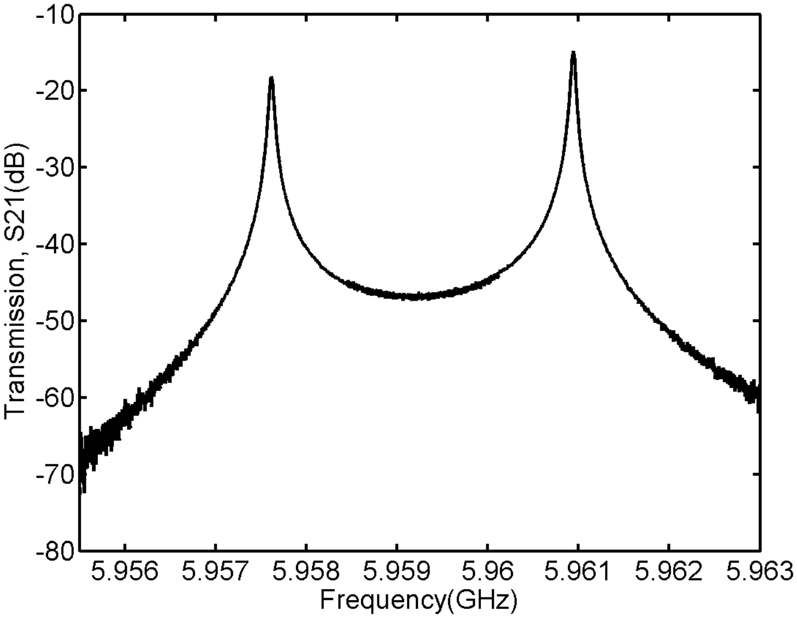

Figure 6.10: Measured fundamental frequencies of the coupled resonators in sample 9 using the NA. Here f_{lower} = 5.9575 GHz and f_{higher} = 5.9608 GHz with loaded quality factors of 1.15×10^5 and 1.25×10^5 respectively. The measured splitting in the frequencies, Δf $\approx$ 3 MHz.

To predict the splitting in the fundamental frequencies at the avoided crossing, the circuit in fig. 4.2 was simulated in AIM Spice by inserting the resonator parameters for sample 9 (details listed in table 4.1). The simulations showed that the minimum splitting in the fundamental frequencies for this sample would be 1.1 MHz, but the measured splitting was 2 MHz in the first run and 3 MHz in the second run, on the same sample. There is no certain explanation for the irreproducibility in the splitting, but the possible causes were discussed in section 5.6. However, this variation was not critical for further measurements on the sample as the frequency of the current through the small coils could always be adjusted to the splitting frequency.

After the two fundamental frequencies were identified, the circuit in fig. 6.9 was used to make further measurements on the sample. Initially, the frequencies were shifted with a uniform magnetic field as discussed in section 6.2.1. The observed lowering in the fundamental frequencies shown in fig. 6.11 were only $\approx$ 10% of the values reported in [12], owing to the shielding effect obtained from the superconducting face of the tuning disc above it. For an applied field of 0.5 mT from the Helmholtz coils, a shift of 186 kHz and 139 kHz in the lower and higher frequencies respectively, was observed. Although a greater lowering in the frequencies could be obtained for a field of ≈ 0.7 mT, the current required by the Helmholtz coils to generate this field caused heating of the coils after a while and could not be used throughout the experiment. Therefore, a uniform field of 0.5 mT was used for further measurements.

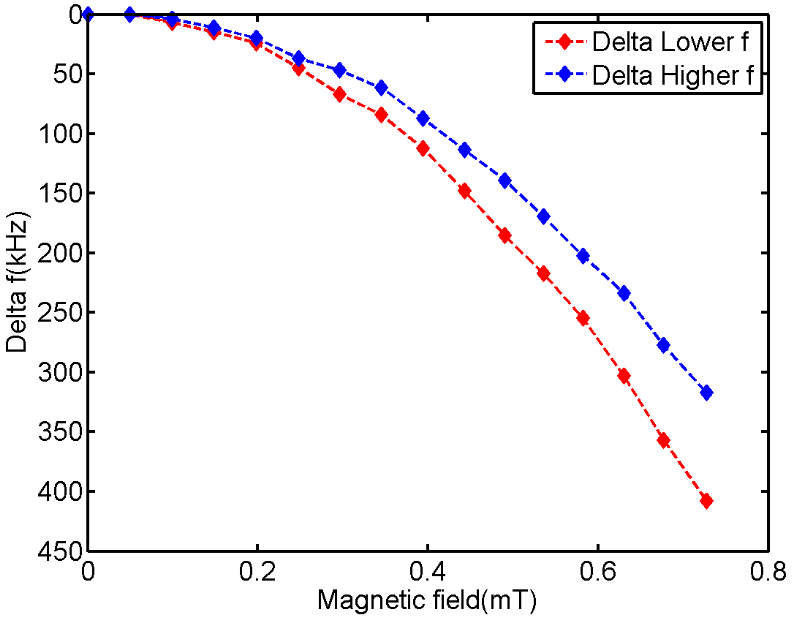

Figure 6.11: Shift in the lower and higher fundamental frequencies on applying a dc magnetic field perpendicular to the plane of the sample.

An alternating current with frequency $\omega_1 = 0 - 120$ kHz and $I_{peak} = 10$ mA was passed through one of the small coils under the resonator sample. This caused a variation in the inductance of the resonator and hence in the resonant frequencies as described in the low amplitude perturbation analysis in section 6.3. The output of the LIA provided a dc component proportional to the transmitted signal from the resonators for a range of ω_1 as shown in fig. 6.12. The theoretical values in the figure were obtained from simulations in MATLAB, and normalized to unity at frequency$(\frac{\omega_1}{2\pi}) \rightarrow 0$.

Comparison of the measured and the theoretical data in fig. 6.12: It was observed that the magnitude of the peak at the fundamental frequency (ω_{0lower}) decreased more rapidly than expected, as the low frequency signal ω_1 was increased by a few hundred Hz. One of the main causes for smaller shifts in the microwave resonant frequency due to the RF field is believed to be the electrical conductance of the

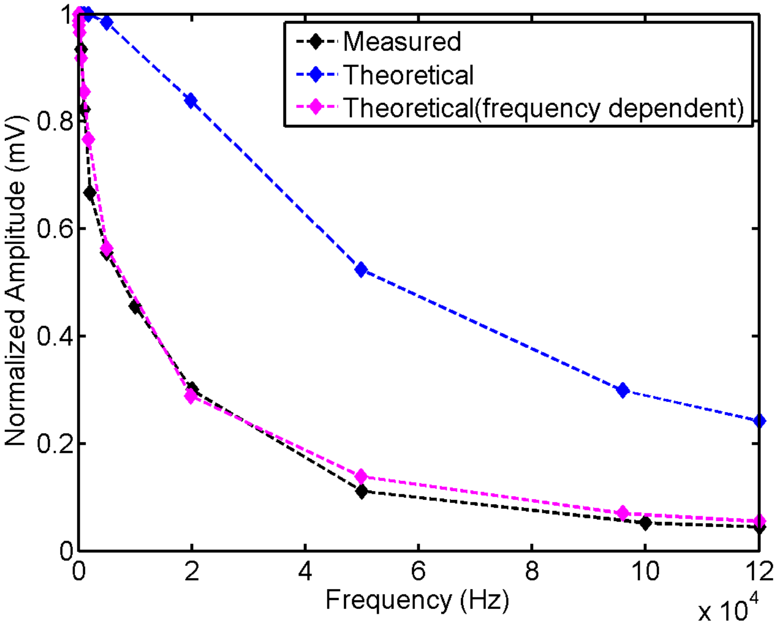

Figure 6.12: A dc level recorded on the output of the LIA that shows the amplitude of the peak at the fundamental frequency, ω_{0lower} as a function of the frequency ($\frac{\omega_1}{2\pi}$) of the alternating field from the small coil applied to the resonator.

wirebonds connecting the ground planes on the chip and PCB as explained below:

It can be seen from fig. 6.13a that the gap between the centre track and the ground plane is open at one end so that the magnetic field from both the external Helmholtz coil and the RF field from the small coil can change the kinetic inductance of the resonator. When a dc field is applied, the shielding currents flow not only along the centre tracks, but also back through the ground planes as shown in fig. 6.13a.

However, at the RF frequencies used, the inductive impedance of the slot (ωL_{slot}) becomes greater than the resistance of the wirebonds across the open end. This diverts the RF currents as illustrated schematically in fig. 6.13b, and reduces the change in kinetic inductance of the microwave resonator.

Simulations were performed in COMSOL [71] to estimate the ratio of the kinetic inductance (KI) of the resonator in two extreme cases of the inductive impedance of the slot, i.e.,

1. For an *open-end* slot, as in fig. 6.13a, and

2. for a *closed-end* slot, as in fig. 6.13b, which is shorted by a *superconducting* wirebond.

In the latter case, as ω_1 is increased, the inductive impedance of the slot can become greater than the resistance of the wirebonds, i.e., $\omega_1 L_{slot} > R_{wirebonds}$, and the current flowing along the centre tracks is diverted through the wirebonds to the PCB ground plane. The simulations showed that $(\frac{\mathrm{KI}_{\mathrm{closed-end}}}{\mathrm{KI}_{\mathrm{open-end}}}) \approx 0.2$

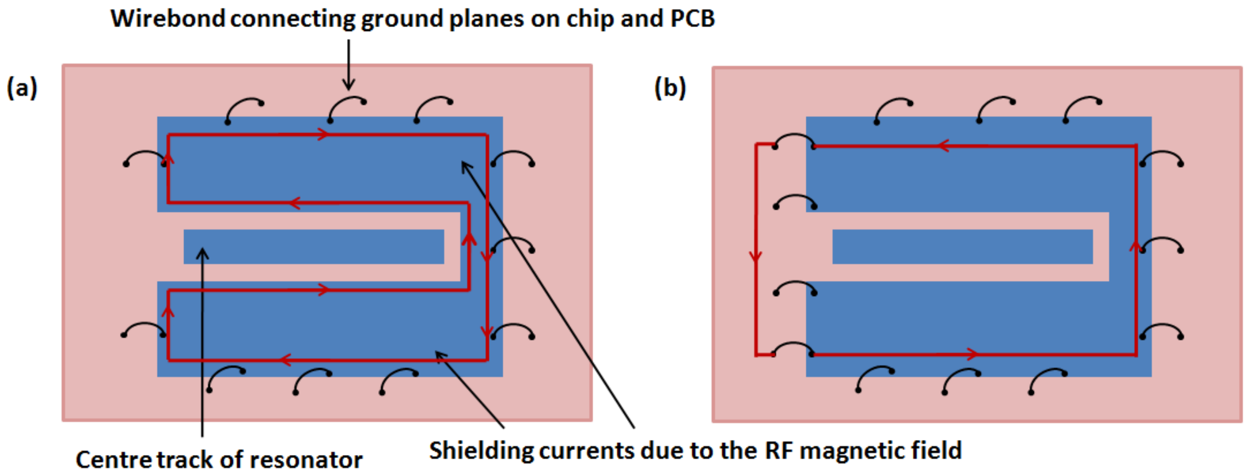

Figure 6.13: Schematic of the two cases of having an open and closed-end slots. (a) Open-end: For a dc field, the induced shielding currents flow in the ground planes on the chip. (b) Closed-end: For an RF field, the shielding currents flow through the wirebonds and the ground plane on the PCB.

and therefore, the frequency shift at higher RF fields is expected to be $\sim 20-25\%$ of its value at lower frequency fields.

Hence, this factor was incorporated into the theoretical voltage data obtained from simulations in MATLAB to calculate its frequency dependence of the form:

$$V(\omega_1) = 0.2V_{theoretical} + [V_{theoretical} - (0.2V_{theoretical})]\left[\frac{1}{(1+\omega_1\tau)}\right] \tag{6.5}$$

where 0.2 accounts for the drop in voltage by a factor of 5 due to the lower resistance of the wirebonds, and ω_1 is the frequency of the RF current flowing through one of the small coils. A decay time constant, $\tau = \frac{L}{R} = 2.3 \times 10^{-4}$ s was used in the fit, which resulted in a close agreement between the theoretical and the measured values shown in fig. 6.12.

The value of τ could be estimated from the following calculations: $\tau = \frac{2\pi}{\omega_1}$ s and $\omega_1 = (\frac{2R_{wirebond}}{L_{slot}})$ rad/s. The resistance of a single wirebond was determined from its length, $l = 500$ μm, diameter $= 25$ μm and the resistivity, $\rho_{1.3K} = \frac{\rho_{300K}}{30} = 9.4 \times 10^{-10}$ Ω.m.

The inductance of the slot was calculated using the formula, $L_{slot} = (1.25 \times \mu_0 \times l_{slot})$ [90], where the length of the slot was assumed to be approximately the length of the resonator (11 mm). The value of τ was then determined to be 5.4×10^{-5} s, about a quarter of the fitted value of $\tau = 2.3 \times 10^{-4}$ s. It should be noted that this calculation assumes the effect of only one wirebond. In practice, the other wirebonds will reduce the value of $\mathrm{R_{wirebond}}$ and increase the calculated τ, closer to the fitted value.

Simulations in MATLAB in fig. 6.6 showed that the amplitude of the peak at ω_{0lower} would gradually decrease as ω_1 was increased, and rise again when $\omega_1 = \omega_{splitting}$. But in the experiment, ω_1 was not increased up to $\omega_{splitting}$ and hence, only a decrease in the peak amplitude was observed as shown in fig. 6.12.

In conclusion, preliminary experiments to study electro-mechanical interaction using the small current-carrying coils were carried out in the low amplitude perturbation limit, where the inductance of only one of the microwave resonators was varied and good agreement was obtained with theoretical expectations. As a next step, the effect of the perturbation could be studied over a wider frequency range, i.e., until $\omega_1 = \omega_{splitting} = (2\pi \times 3\ \text{MHz})$ and compared to the theoretical predictions.

CHAPTER 7

CONCLUSIONS AND FUTURE WORK

The motivation of the work presented in this thesis is the significant interest in experiments based on the coupling of a nanobar to a superconducting microwave resonator to study electro-mechanical interaction. The advantage of coupling a nanobar to a system of coupled microwave resonators is that the splitting frequency can be chosen to be of the order of the fundamental frequency of the nanobar ($\approx 1 - 10$ MHz), and that coupling to the square of the nanobar displacement can be achieved. This is the regime in which the theoretical model proposed by G.Heinrich and F.Marquardt in [4] can be applied.

The first step towards measuring microwave-nanomechanical interaction was to gain an understanding of a basic system of coupled microwave resonators. Therefore, this system was thoroughly analysed by simulations in COMSOL [71] and AIM Spice. The simulations guided the design of a wide range of devices and the preliminary experiments were focussed on the study of the splitting frequency (Δf) as a function of coupling between the resonators (C_k).

Measurements on the first set of coupled resonator devices described in chapter 3 showed discrepancies in the absolute values of the resonant frequencies and their splitting from the values predicted in AIM Spice. Asymmetries in the resonant peaks and a high background level implied that there was significant crosstalk within the resonator chip, the PCB and the copper cavity. Simulations in COMSOL [71] showed that the capacitance between adjacent transmission lines on the PCB was an order of magnitude higher than the capacitance between the transmission lines and the resonators on the chip, and could not therefore, be ignored. This caused an undesirably high background level which distorted the peak shapes, and would inhibit the measurement of small changes to the resonant frequencies.

Therefore, as described in chapter 4, a second set of coupled resonator devices, a new PCB, and a new copper cavity were designed with modified geometries to minimize the effect of crosstalk. A substantial lowering in the background level (by ≈ 30 dB) was achieved by reducing the number of transmission lines and increasing the number of vias on the PCB, using smaller dimensions of the PCB and copper cavity, and soldering the PCB to the base of the copper cavity.

Investigation of the properties of the new resonator devices showed a good agreement of the absolute values of the resonant frequencies with the designed values. Also, the peak shapes were closer to the expected Lorentzian due to a lower background level. However, the deviation of the measured splitting from the predicted values, the difference in the quality factors of the resonators, and unequal dip magnitudes in the reflection measurements, implied that the two resonators were non identical and hence one of the resonators in each sample needed to be tuned to reach the avoided crossing.

A significant experimental achievement of this thesis was the design and test of a mechanism for performing large scale tuning of the coupled resonators through the avoided crossing, as described in chapter 5. A frequency tuning range of up to 50 MHz was successfully achieved, and in comparison to the work reported in the literature, it is for the first time that a tuning mechanism has not caused a degradation of the resonator quality factors over the entire frequency tuning range. An excellent agreement was obtained with the theoretical expectations (in AIM Spice) for the resonator properties as one of the resonators was tuned through the avoided crossing, i.e., the quality factors of both the resonators were nearly identical and the two dips in the reflection data were of closely equal magnitude, confirming the behaviour of the resonators as a single entity. The measured splitting at the avoided crossing in two of the samples were 7.4 MHz and 2.5 MHz, of the order of the expected nanobar resonant frequencies, which would enable the study of microwave-nanomechanical coupling in these samples.

In the absence of nanobars, another experiment was devised wherein the inductance of one of the microwave resonators was varied, rather than its capacitance. A feasibility study showed that in the presence of a uniform bias field generated from external Helmholtz coils, and a low RF field applied from a small coil placed underneath the resonator chip, a frequency shift of ≈ 40 MHz/A could be obtained. The advantage of using the coils was that, the frequency of the ac current and hence of the magnetic field could be adjusted to the splitting frequency in different samples, unlike with nanobars which have fixed resonant frequencies. Also, with the help of the tuning mechanism, it is possible to study electro-mechanical interaction across a wide range of the splitting frequencies as the RF current through the coil can be adjusted to match with the splitting.

Prior to carrying out the experiments, the system was analysed theoretically using a mechanical analogue of the lumped element model of the microwave resonators. The analysis was based on a system of two identical, coupled spring-mass oscillators and, to simulate the effect of varying the inductance of one of the resonators by the RF field, the mass of one of the oscillators was perturbed. The effect of the perturbation was analysed in the two limiting cases of *small* and *large* amplitudes using the MATLAB codes adapted from [71]. The expressions for the expected output displacement signals in the *small* amplitude perturbation limit showed that, apart from the peaks at the fundamental frequencies of the coupled resonators, additional peaks at ω_{0lower}, $\omega_{0higher}$, and side-bands at $(\omega_{0lower} \pm \omega_1)$ and $(\omega_{0higher} \pm \omega_1)$ were present. As ω_1 was increased, the side-bands moved further away from the corresponding perturbation peaks at ω_{0lower} and $\omega_{0higher}$, and also the amplitude of all the perturbation peaks decreased, except for the special case of $\omega_1 = \omega_{splitting}$, where the simulations predicted a rise in the peak amplitudes at ω_{0lower} and $\omega_{0higher}$, to a value which was half of that at $\omega_1 = 0$.

However, the case more relevant to the theoretical model in [4] was that of the *large* amplitude perturbation signal, which predicted a splitting of the fundamental peaks themselves for a sufficiently large amplitude, b and, when $\omega_1 = \omega_{splitting}$. This case was analysed numerically for a system of two identical, coupled spring-mass oscillators. When the amplitude of the perturbation was large, i.e., when $b \approx \frac{10}{Q}$, where Q is the quality factor of the resonators, a *splitting* of the individual fundamental peaks was obtained, unlike the appearance of the side-bands in the small amplitude perturbation limit. Thus, the theoretical analysis provided an insight to a system of identical, coupled mechanical oscillators with one of the masses being varied by a perturbation.

Since the physics in a system of microwave resonators is closely analogous to the mechanical model, the analysis guided the experimental measurements on a system of coupled microwave resonators with the inductance of one of the resonators being varied with an RF field generated by a small coil placed underneath the resonator sample. A uniform external field of 0.5 mT, which lowered the fundamental frequencies at ω_{0lower} and $\omega_{0higher}$ by 139 kHz and 186 kHz respectively, was used to obtain greater sensitivity of the frequencies to the low RF field. A measurement circuit adapted from [11] was designed to demodulate and measure the dc component proportional to the ac signal at relevant frequencies such as ω_{0lower}, $\omega_{0higher}$.

As described in chapter 6, the preliminary experiments to study electro-mechanical interaction were successfully conducted in the *small* amplitude perturbation limit, where the inductance of only one of the resonators was varied. A direct comparison of the measured and theoretical amplitude variation of the signal at ω_{0lower} for a range of $\omega_1 = 2\pi \times (0 - 120)$ kHz showed a large deviation. Simulations in COMSOL [71] indicated that the screening currents flowing in the ground plane between the chip and the PCB were capable of reducing the effect of the magnetic field by a factor of $\approx 4 - 5$. Hence, the frequency dependence of the screening currents was taken into account and incorporated into the theoretical values and a comparison with the measured values showed a very good agreement, confirming the influence of the wirebonds on the screening currents.

7.1 Future Work

The experiments on the perturbation of the resonator inductance could be completed in both the limits with the following modifications to the apparatus:

- A higher magnitude of the bias field could be applied with a large permanent magnet so as to lower the frequencies by ≈ 1 MHz, as compared to a shift of 186 kHz from the Helmholtz coils. This would increase the sensitivity of the frequencies to the alternating field from the small coils, which has already been tried successfully.
- All the low temperature measurements described in chapters 5 and 6 were carried out with the sample stage enclosed in a vacuum can, which was essential for the proposed experiments with nanobars. The experiments with the coils could be performed by pumping directly on the helium bath in the cryostat so that the sample is immersed in superfluid helium.
- The copper wire forming the coils could be replaced with superconducting (niobium) wire, and hence a greater magnitude of current could be passed through the coils, which would result in a higher response of the relevant peak amplitudes.
- A lower noise amplifier could be used in the first stage of the amplifier chain so that the measurements could be carried out at smaller RF amplitudes and at higher frequencies.
- The proposed model in [4] could be implemented by driving the coils under both the resonators with anti-phase RF fields.

Thus, the investigation of the electro-mechanical interaction and a comparison with the simulations could be carried out in both the low amplitude limit, which has not been previously considered and the high amplitude limit, to obtain a comparison with the theoretical model.

When the samples with nanobars are available, the proposed experiments of studying the microwave-nanomechanical interaction in [4] could be conducted by using the techniques developed in this thesis.

APPENDIX A

A.1 Coupled spring-mass oscillators

The equation of motion of mass m_1 is given by:

$$m_1 x_1^{''} = F\cos(\omega t) - kx_1 - k_d x_1^{'} + (x_2 - x_1)k_c \tag{A.1}$$

Therefore,

$$m_1 x_1^{''} + k_d x_1^{'} + (k + k_c)x_1 - k_c x_2 = F\cos(\omega t) \tag{A.2}$$

The equation of motion of mass m_2 is written as:

$$m_2 x_2^{''} = -kx_2 - k_d x_2^{'} + (x_1 - x_2)k_c \tag{A.3}$$

Hence,

$$m_2 x_2^{''} + (k + k_c)x_2 + k_d x_2^{'} = k_c x_1 \tag{A.4}$$

$\Rightarrow$

$$x_1 = \frac{1}{k_c}\left[m_2 x_2^{''} + (k + k_c)x_2 + k_d x_2^{'}\right] \tag{A.5}$$

Substituting eqn A.5 in eqn A.2 results in a fourth order differential equation in x_2 of the form:

$$Ax_2^{''''} + Bx_2^{'''} + Cx_2^{''} + Dx_2^{'} + Ex_2 = F\cos(\omega t) \tag{A.6}$$

Further substitutions can be made to obtain a similar fourth order differential equation in x_1. The general solutions for x_1 and x_2 are assumed to be of the form:

$$x_1 = G\cos\omega t + H\sin\omega t \tag{A.7}$$

and

$$x_2 = P\cos\omega t + Q\sin\omega t \tag{A.8}$$

where

$$G = \frac{1}{k_c}[-m_1\omega^2 P + k_d Q + (k+k_c)P]$$

$$H = \frac{1}{k_c}[-m_1\omega^2 Q + k_d P + (k+k_c)Q]$$

$$P = \frac{F(A\omega^4 - C\omega^2 + E)}{(A\omega^4 - C\omega^2 + E)^2 + (\omega D - \omega^3 B)^2}$$

$$Q = \frac{F(\omega D - \omega^3 B)^2)}{(A\omega^4 - C\omega^2 + E)^2 + (\omega D - \omega^3 B)^2}$$

The constants A, B, C, D and E are defined as $A = \frac{(m_1 m_2)}{k_c}$, $B = \frac{(m_1+m_2)k_d}{k_c}$, $C = \frac{-(m_1+m_2)(k+k_c)+k_d^2}{k_c}$, $D = \frac{2(k+k_c)k_d}{k_c}$ and $E = \frac{(k^2+2kk_c)}{k_c}$.

To simulate the effect of varying the inductance of one of the microwave resonators by applying an alternating magnetic field, the mass of one of the mechanical oscillators was varied in the following manner:

$$m_1 = m_1 + b\cos\omega_1 t \tag{A.9}$$

where, b and ω_1 are the amplitude and frequency of the time varying perturbation signal applied to mass m_1. Here, it is assumed that $b\cos\omega_1 t \ll m_1$. The total displacement x_2, due to a perturbation in m_1 is now given by

$$x_2 = x_{20} + x_{21} \tag{A.10}$$

where x_{20} and x_{21} are the displacements in the absence and presence respectively, of a perturbation in m_1;

and in the analysis presented here, $x_{21} \ll x_{20}$, i.e., the *small amplitude* perturbation limit.

On further substitution and simplification, the equation of motion for x_{21} can be written as:

$$\begin{aligned} Ax_{21}^{''''} + Bx_{21}^{'''} + Cx_{21}^{''} + Dx_{21}^{'} + Ex_{21} = &-\frac{b}{2}[W\cos(\omega+\omega_1)t + Y\sin(\omega+\omega_1)t] \\ &- \frac{b}{2}[W\cos(\omega-\omega_1)t + Y\sin(\omega-\omega_1)t] \end{aligned} \tag{A.11}$$

where,

$$W = \frac{1}{k_c}[m_2\omega^4 P - k_d\omega^3 Q - (k+k_c)\omega^2 P]$$

and,

$$Y = \frac{1}{k_c}[m_2\omega^4 Q - k_d\omega^3 P - (k+k_c)\omega^2 Q]$$

The solution for x_{21} is assumed to be of the form:

$$x_{21} = P_+\cos(\omega+\omega_1)t + Q_+\sin(\omega+\omega_1)t + P_-\cos(\omega-\omega_1)t + Q_-\sin(\omega-\omega_1)t \tag{A.12}$$

where,

$$P_+ = \frac{[A(\omega+\omega_1)^4 - C(\omega+\omega_1)^2 + E]}{[A(\omega+\omega_1)^4 - C(\omega+\omega_1)^2 + E]^2 + [D(\omega+\omega_1) - (\omega+\omega_1)^3 B]^2}$$

$$Q_+ = \frac{[D(\omega+\omega_1) - (\omega+\omega_1)^3 B]^2}{[A(\omega+\omega_1)^4 - C(\omega+\omega_1)^2 + E]^2 + [D(\omega+\omega_1) - (\omega+\omega_1)^3 B]^2}$$

$$P_- = \frac{[A(\omega-\omega_1)^4 - C(\omega-\omega_1)^2 + E]}{[A(\omega-\omega_1)^4 - C(\omega-\omega_1)^2 + E]^2 + [D(\omega-\omega_1) - (\omega-\omega_1)^3 B]^2}$$

and

$$Q_- = \frac{[D(\omega-\omega_1) - (\omega-\omega_1)^3 B]^2}{[A(\omega-\omega_1)^4 - C(\omega-\omega_1)^2 + E]^2 + [D(\omega-\omega_1) - (\omega-\omega_1)^3 B]^2}$$

Therefore, the total solution for x_{21} is given by:

$$\begin{aligned} x_{21} = &-\frac{b}{2}P_+W\cos(\omega+\omega_1)t - \frac{b}{2}Q_+W\sin(\omega+\omega_1)t \\ &- \frac{b}{2}P_-W\cos(\omega-\omega_1)t - \frac{b}{2}Q_-W\sin(\omega-\omega_1)t \\ &+ \frac{b}{2}Q_+Y\cos(\omega+\omega_1)t - \frac{b}{2}P_+Y\sin(\omega+\omega_1)t \\ &+ \frac{b}{2}Q_-Y\cos(\omega-\omega_1)t - \frac{b}{2}P_-Y\sin(\omega-\omega_1)t \end{aligned} \tag{A.13}$$

The above equation can be simplified and written as:

$$\begin{aligned} x_{21} = {} & \frac{b}{2}(Q_+Y - P_+W)\cos(\omega+\omega_1)t - \frac{b}{2}(P_+Y + Q_+W)\sin(\omega+\omega_1)t \\ & + \frac{b}{2}(Q_-Y - P_-W)\cos(\omega-\omega_1)t - \frac{b}{2}(P_-Y + Q_-W)\sin(\omega-\omega_1)t \end{aligned} \tag{A.14}$$

or

$$x_{21} = G\cos(\omega+\omega_1)t + H\sin(\omega+\omega_1)t + J\cos(\omega-\omega_1)t + L\sin(\omega-\omega_1)t \tag{A.15}$$

where

$$G = \frac{b}{2}(Q_+Y - P_+W)\cos(\omega+\omega_1)t$$

$$H = -\frac{b}{2}(P_+Y + Q_+W)\sin(\omega+\omega_1)t$$

$$J = \frac{b}{2}(Q_-Y - P_-W)\cos(\omega-\omega_1)t$$

and

$$L = -\frac{b}{2}(P_-Y + Q_-W)\sin(\omega-\omega_1)t$$

Therefore it can be seen from equations A.8, A.10 and A.15, that the total displacement x_2 in the presence of a perturbation signal is a function of the frequencies ω, $(\omega+\omega_1)$ and $(\omega-\omega_1)$. To demodulate x_{21}, it is combined with a reference signal. For example, when x_{21} is combined with a reference signal of the form $\cos\omega$t, equation A.15 is modified to

$$x_{21} = \frac{(G+J)}{2}\cos\omega_1 t + \frac{(H-L)}{2}\sin\omega_1 t \tag{A.16}$$

where, $\frac{(G+J)}{2}$ and $\frac{(H-L)}{2}$ are the amplitudes of the displacement which are in and out of phase respectively, with the reference signal.

APPENDIX B

B.1 Fitting the resonance curve to a theoretical model

In this section, the method that was used to fit the resonance curve to a theoretical model is explained.

A single coplanar resonator can be represented as a lumped element, parallel LCR circuit. If the circuit is driven by a current of amplitude, I and frequency, ω then the voltage at the output end is given by:

$$V = \frac{\omega^2 I}{C\tau[(\omega_0^2 - \omega^2)^2 + \frac{\omega^2}{\tau^2}]} + i\frac{I\omega(\omega_0^2 - \omega^2)}{C[(\omega_0^2 - \omega^2)^2 + \frac{\omega^2}{\tau^2}]} \tag{B.1}$$

Hence,

$$|V| = \frac{\omega I}{C\sqrt{[(\omega_0^2 - \omega^2)^2 + \frac{\omega^2}{\tau^2}]}} \tag{B.2}$$

The expression for V assumes that no additional signal is present at the detector. But, it was seen from the measurements that there is a breakthrough signal, which in general has components that are in and out of phase with the drive signal I$e^{i\omega t}$. Let the in-phase component be $(A \times I)$ and the out-of phase component be $(B \times I)$. The theoretical complex voltage is then given by

$$V = \left[\frac{\omega^2 I}{C\tau[(\omega_0^2 - \omega^2)^2 + \frac{\omega^2}{\tau^2}]} + \left(A \times \frac{I}{C}\right)\right] + i\left[\frac{I\omega(\omega_0^2 - \omega^2)}{C[(\omega_0^2 - \omega^2)^2 + \frac{\omega^2}{\tau^2}]} + \left(B \times \frac{I}{C}\right)\right] \tag{B.3}$$

Therefore,

$$|V| = \sqrt{\left[\frac{\omega^2 I}{C\tau[(\omega_0^2 - \omega^2)^2 + \frac{\omega^2}{\tau^2}]} + \left(A \times \frac{I}{C}\right)\right]^2 + \left[\frac{I\omega(\omega_0^2 - \omega^2)}{C[(\omega_0^2 - \omega^2)^2 + \frac{\omega^2}{\tau^2}]} + \left(B \times \frac{I}{C}\right)\right]^2} \tag{B.4}$$

The measured asymmetric resonance was fitted to the expression for $|V|$ in eq. B.4, where, ω_0 is the resonant frequency, τ is the inverse of the bandwidth, and I/C is the amplitude of the peak. The quality factor of the resonance is determined from

$$Q = \omega_0 \times \tau \tag{B.5}$$

In fig. B.1, the measured and fitted resonance curves are shown.

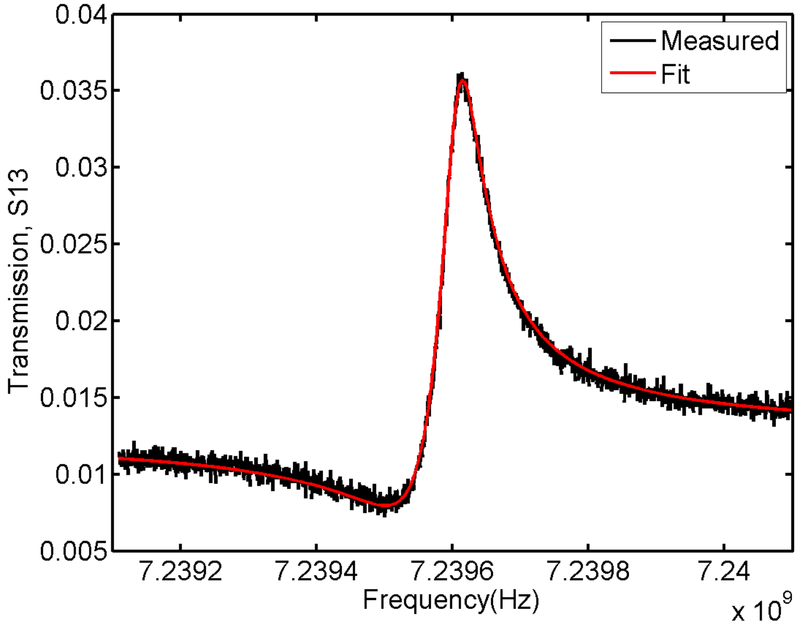

Figure B.1: The lower frequency resonance in sample 1 was fitted to the complex Lorentzian function in eq. B.4. The initial and fitted parameters are listed in table B.1.

Parameter	Initial value	Fitted value
I/C	1×10^2	1.7×10^3
τ	5.6×10^{-4}	1.6×10^{-5}
ω_0	7.2396×10^9	7.239606×10^9
A	1	2.7×10^{-6}
B	-20	-6.93×10^{-6}

Table B.1: The initial and fitted parameters to estimate the resonant frequency and quality factor (Q_L) of the lower frequency resonance in sample 1 using the least-squares curve fitting routine in MATLAB. Q_L was calculated to be 1.1×10^5.

APPENDIX C

C.1 Additional information on experimental methods

The lithographic methods used for fabricating the samples described in this work are detailed in chapter 3. In this section additional information such as settings on the argon ion beam miller and the wire-bonder machine are provided.

Settings on the Oxford IM150 Argon Ion Beam miller:

Pressure before argon inlet	8.5×10^{-7} mbar
Pressure after argon inlet	2×10^{-4} mbar

Table C.1: Pressure readings

Load	RF	OM	Tune
24	OK	3.10	23

Table C.2: Settings on the Auto Tune Controller when the RF generator power is 150 W.

Screen Voltage	498 V
Screen Current	58.8 mA
Accelerator Voltage	202 V
Accelerator Current	1.4 mA
Neutralizer current	5.5 A

Table C.3: Settings on the RF 50 Controller

The parameters used for making the the wirebonds are given in table C.4:

F_1	T_1	P_1	F_2	T_2	P_2
2.8	2.5	3	3	3	2.1

Table C.4: The parameters used in forming the bonds are the force F, time T and power P.

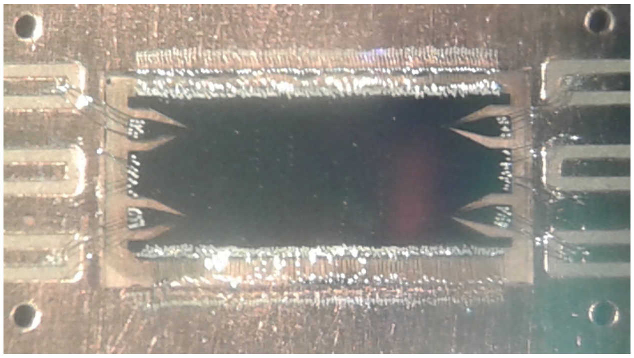

Figure C.1: A close-up view of a resonator sample wirebonded to a copper PCB.

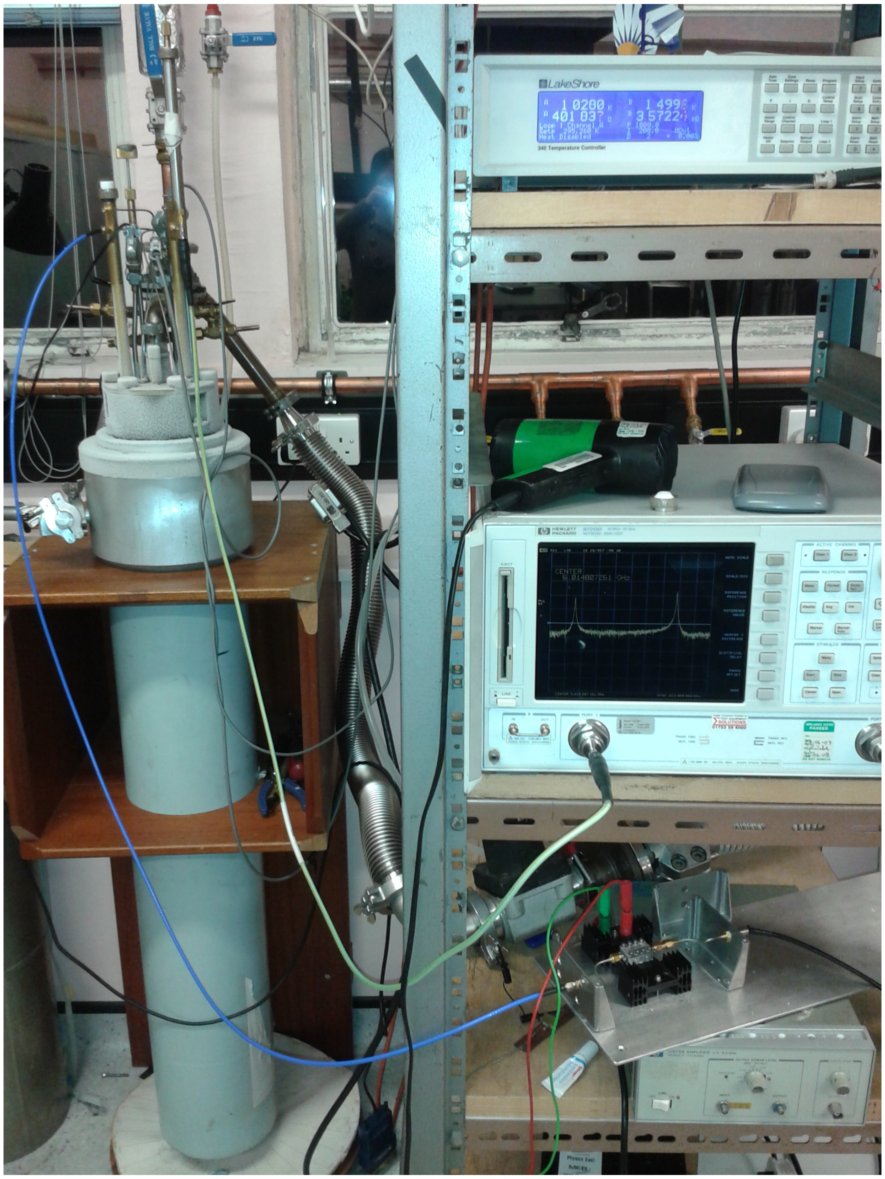

Figure C.2: A photograph of the low temperature experimental set-up used for measuring the samples.

LIST OF REFERENCES

[1] Florian Marquardt and Steven M. Girvin. Optomechanics. *Physics*, 2:40, May 2009.

[2] JD Teufel, CA Regal, and KW Lehnert. Prospects for cooling nanomechanical motion by coupling to a superconducting microwave resonator. *New Journal of Physics*, 10(9):095002, 2008.

[3] JD Teufel, Tobias Donner, Dale Li, JW Harlow, MS Allman, K Cicak, AJ Sirois, JD Whittaker, KW Lehnert, and RW Simmonds. Sideband cooling of micromechanical motion to the quantum ground state. *Nature*, 475(7356):359–363, 2011.

[4] Georg Heinrich and Florian Marquardt. Coupled multimode optomechanics in the microwave regime. *EPL (Europhysics Letters)*, 93(1):18003, 2011.

[5] P Townsend and J Sutton. Investigation by electron tunneling of the superconducting energy gaps in nb, ta, sn, and pb. *Physical Review*, 128(2):591, 1962.

[6] David M. Pozar. *Microwave Engineering*. John Wiley and Sons, Inc, 2005.

[7] Z Kim, CP Vlahacos, JE Hoffman, JA Grover, KD Voigt, BK Cooper, CJ Ballard, BS Palmer, M Hafezi, JM Taylor, et al. Thin-film superconducting resonator tunable to the ground-state hyperfine splitting of ^{87}rb. *arXiv preprint arXiv:1109.5205*, 2011.

[8] Y Wang, Martin J Prest, and MJ Lancaster. Cryogenic performance of micromachined silicon rocking actuator for tuning a superconducting resonator. *Electronics Letters*, 46(23):1569–1571, 2010.

[9] J. E. Healey, T. Lindstrm, M. S. Colclough, C. M. Muirhead, and A. Ya. Tzalenchuk. Magnetic field tuning of coplanar waveguide resonators. *Applied Physics Letters*, 93(4):–, 2008.

[10] Martin Sandberg, CM Wilson, Fredrik Persson, Thilo Bauch, Göran Johansson, Vitaly Shumeiko, Tim Duty, and Per Delsing. Tuning the field in a microwave resonator faster than the photon lifetime. *Applied Physics Letters*, 92(20):203501, 2008.

[11] CA Regal, JD Teufel, and KW Lehnert. Measuring nanomechanical motion with a microwave cavity interferometer. *Nature Physics*, 4(7):555–560, 2008.

[12] Joanne E Healey. Experiments to develop high q and tunable superconducting coplanar resonators applicable for quantum bit technology. December 2010.

[13] Florian Marquardt, AA Clerk, and SM Girvin. Quantum theory of optomechanical cooling. *arXiv:0803.1164v1 [quant-ph]*, 2008.

[14] Tobias J Kippenberg and Kerry J Vahala. Cavity optomechanics: back-action at the mesoscale. *science*, 321(5893):1172–1176, 2008.

[15] V.B. Braginsky and V.N. Rudenko. Gravitational waves and the detection of gravitational radiation. *Physics Reports*, 46(5):165 – 200, 1978.

[16] B Abbott, R Abbott, R Adhikari, A Ageev, Bruce Allen, R Amin, SB Anderson, WG Anderson, M Araya, H Armandula, et al. Detector description and performance for the first coincidence observations between ligo and geo. *Nuclear Instruments and Methods in Physics Research Section A: Accelerators, Spectrometers, Detectors and Associated Equipment*, 517(1):154–179, 2004.

[17] Dustin Kleckner and Dirk Bouwmeester. Sub-kelvin optical cooling of a micromechanical resonator. *Nature*, 444(7115):75–78, 2006.

[18] C. Monroe, D. M. Meekhof, B. E. King, S. R. Jefferts, W. M. Itano, D. J. Wineland, and P. Gould. Resolved-sideband raman cooling of a bound atom to the 3d zero-point energy. *Phys. Rev. Lett.*, 75:4011–4014, Nov 1995.

[19] O. Arcizet, P.-F. Cohadon, T. Briant, M. Pinard, and A. Heidmann. Radiation-pressure cooling and optomechanical instability of a micromirror. *Nature*, 444:71–74, 2006.

[20] H. R. Bohm, M. Paternostro, F. Blaser, G. Langer, J. B. Hertzberg, K. C. Schwab, D. Bauerle, M. Aspelmeyer, and A. Zeilinger. Self-cooling of a micromirror by radiation pressure. *Nature*, 444:67 – 70, 2006.

[21] A. Schliesser, P. Del'Haye, N. Nooshi, K. J. Vahala, and T. J. Kippenberg. Radiation pressure cooling of a micromechanical oscillator using dynamical backaction. *Phys. Rev. Lett.*, 97:243905, Dec 2006.

[22] JD Thompson, BM Zwickl, AM Jayich, Florian Marquardt, SM Girvin, and JGE Harris. Strong dispersive coupling of a high-finesse cavity to a micromechanical membrane. *Nature*, 452(7183):72–75, 2008.

[23] Simon Gröblacher, Jared B Hertzberg, Michael R Vanner, Garrett D Cole, Sylvain Gigan, KC Schwab, and Markus Aspelmeyer. Demonstration of an ultracold micro-optomechanical oscillator in a cryogenic cavity. *Nature Physics*, 5(7):485–488, 2009.

[24] Thomas Corbitt, Yanbei Chen, Edith Innerhofer, Helge Müller-Ebhardt, David Ottaway, Henning Rehbein, Daniel Sigg, Stanley Whitcomb, Christopher Wipf, and Nergis Mavalvala. An all-optical trap for a gram-scale mirror. *Phys. Rev. Lett.*, 98:150802, Apr 2007.

[25] Pierre-François Cohadon, Antoine Heidmann, and Michel Pinard. Cooling of a mirror by radiation pressure. *Physical Review Letters*, 83(16):3174, 1999.

[26] B Abbott, R Abbott, R Adhikari, P Ajith, B Allen, G Allen, R Amin, SB Anderson, WG Anderson, MA Arain, et al. Observation of a kilogram-scale oscillator near its quantum ground state. *New Journal of Physics*, 11(7):073032, 2009.

[27] Jasper Chan, TP Mayer Alegre, Amir H Safavi-Naeini, Jeff T Hill, Alex Krause, Simon Gröblacher, Markus Aspelmeyer, and Oskar Painter. Laser cooling of a nanomechanical oscillator into its quantum ground state. *Nature*, 478(7367):89–92, 2011.

[28] JD Teufel, JW Harlow, CA Regal, and KW Lehnert. Dynamical backaction of microwave fields on a nanomechanical oscillator. *Physical review letters*, 101(19):197203, 2008.

[29] A Naik, O Buu, MD LaHaye, AD Armour, AA Clerk, MP Blencowe, and KC Schwab. Cooling a nanomechanical resonator with quantum back-action. *Nature*, 443(7108):193–196, 2006.

[30] T Rocheleau, T Ndukum, C Macklin, JB Hertzberg, AA Clerk, and KC Schwab. Preparation and detection of a mechanical resonator near the ground state of motion. *Nature*, 463(7277):72–75, 2009.

[31] J-M Pirkkalainen, SU Cho, Jian Li, GS Paraoanu, PJ Hakonen, and MA Sillanpää. Hybrid circuit cavity quantum electrodynamics with a micromechanical resonator. *Nature*, 494(7436):211–215, 2013.

[32] Peter Weber, Johannes Güttinger, Ioannis Tsioutsios, Darrick Chang, and Adrian Bachtold. Coupling graphene mechanical resonators to superconducting microwave cavities. *Nano letters*, 2014.

[33] F Massel, TT Heikkilä, J-M Pirkkalainen, SU Cho, H Saloniemi, PJ Hakonen, and MA Sillanpää. Microwave amplification with nanomechanical resonators. *Nature*, 480(7377):351–354, 2011.

[34] Jared Barney Hertzberg. *Back-action evading measurements of nanomechanical motion approaching quantum limits.* UNIVERSITY OF MARYLAND, COLLEGE PARK, 2009.

[35] Juha-Matti Pirkkalainen et al. Mechanical resonators coupled to superconducting circuits. 2014.

[36] J.W. Harlow. *Microwave Electromechanics: Measuring and Manipulating the Quantum State of a Macroscopic Mechanical Oscillator.* PhD thesis, University of Colorado, 2011.

[37] Aaron D OConnell, M Hofheinz, M Ansmann, Radoslaw C Bialczak, M Lenander, Erik Lucero, M Neeley, D Sank, H Wang, M Weides, et al. Quantum ground state and single-phonon control of a mechanical resonator. *Nature*, 464(7289):697–703, 2010.

[38] CA Regal and KW Lehnert. From cavity electromechanics to cavity optomechanics. In *Journal of Physics: Conference Series*, volume 264, page 012025. IOP Publishing, 2011.

[39] Markus Aspelmeyer, Tobias J Kippenberg, and Florian Marquardt. Cavity optomechanics. *arXiv preprint arXiv:1303.0733*, 2013.

[40] Markus Arndt, Markus Aspelmeyer, and Anton Zeilinger. How to extend quantum experiments. *Fortschritte der Physik*, 57(11-12):1153–1162, 2009.

[41] Jonathan R Friedman, Vijay Patel, Wei Chen, SK Tolpygo, and James E Lukens. Quantum superposition of distinct macroscopic states. *nature*, 406(6791):43–46, 2000.

[42] H Kamerlingh Onnes and K Hof. Leiden comm, 1911.

[43] W Meissner and R Ochsenfeld. A new effect in penetration of superconductors. *Die Naturwissenschaften*, 21:787–788, 1933.

[44] Fritz London and Heinz London. The electromagnetic equations of the supraconductor. *Proceedings of the Royal Society of London. Series A-Mathematical and Physical Sciences*, 149(866):71–88, 1935.

[45] C Jo Gorter and H Casimir. On supraconductivity i. In *Archives du Musée Teyler*, pages 1–15. Springer, 1935.

[46] H Fröhlich. Theory of the superconducting state. i. the ground state at the absolute zero of temperature. *Physical Review*, 79(5):845–856, 1950.

[47] John Bardeen, Leon N Cooper, and J Robert Schrieffer. Theory of superconductivity. *Physical Review*, 108(5):1175, 1957.

[48] RE Glover III and Ms Tinkham. Conductivity of superconducting films for photon energies between 0.3 and 4 0 k t c. *Physical Review*, 108(2):243, 1957.

[49] Lev Davidovich Landau and VL Ginzburg. On the theory of superconductivity. *Zh. Eksp. Teor. Fiz.*, 20:1064, 1950.

[50] Michael Tinkham. Introduction to superconductivity, 1996. *McCraw-Hill, New York.*

[51] DC Mattis and John Bardeen. Theory of the anomalous skin effect in normal and superconducting metals. *Physical Review*, 111(2):412, 1958.

[52] Adrian Porch, Phil Mauskopf, Simon Doyle, and Chris Dunscombe. Calculation of the characteristics of coplanar resonators for kinetic inductance detectors. *Applied Superconductivity, IEEE Transactions on*, 15(2):552–555, 2005.

[53] J Baselmans, SJC Yates, R Barends, YJY Lankwarden, JR Gao, H Hoevers, and TM Klapwijk. Noise and sensitivity of aluminum kinetic inductance detectors for sub-mm astronomy. *Journal of Low Temperature Physics*, 151(1-2):524–529, 2008.

[54] Peter K Day, Henry G LeDuc, Benjamin A Mazin, Anastasios Vayonakis, and Jonas Zmuidzinas. A broadband superconducting detector suitable for use in large arrays. *Nature*, 425(6960):817–821, 2003.

[55] Rainee N Simons. *Coplanar waveguide circuits, components, and systems*, volume 165. John Wiley & Sons, 2004.

[56] KC Gupta, R Garg, I Bahl, and P Bhartia. Microstrip lines and slotlines. 1996. *Arthech House.*

[57] G Hammer, S Wuensch, M Roesch, K Ilin, E Crocoll, and M Siegel. Superconducting coplanar waveguide resonators for detector applications. *Superconductor Science and Technology*, 20(11):S408, 2007.

[58] Luigi Frunzio, Andreas Wallraff, David Schuster, Johannes Majer, and Robert Schoelkopf. Fabrication and characterization of superconducting circuit qed devices for quantum computation. *IEEE Transactions on Applied Superconductivity*, 15(2):860–863, 2005.

[59] CE Gough, A Porch, MJ Lancaster, JR Powell, B Avenhaus, JJ Wingfield, D Hung, and RG Humphreys. High tc coplanar resonators for microwave applications and scientific studies. *Physica C: Superconductivity*, 282:395–398, 1997.

[60] T. Lindström, J. E. Healey, M. S. Colclough, C. M. Muirhead, and A. Ya. Tzalenchuk. Properties of high-quality coplanar waveguide resonators for qip and detector applications. *Journal of Physics:Conference Series*, 150, 2009.

[61] Dr.F.Huang. University of birmingham, private communication, 2010.

[62] T. Lindström, J. E. Healey, M. S. Colclough, C. M. Muirhead, and A. Ya. Tzalenchuk. Properties of superconducting planar resonators at millikelvin temperatures. *Phys. Rev. B*, 80:132501, Oct 2009.

[63] AB Pippard. Field variation of the superconducting penetration depth. *Proceedings of the Royal Society of London. Series A. Mathematical and Physical Sciences*, 203(1073):210–223, 1950.

[64] John Bardeen. Critical fields and currents in superconductors. *Reviews of Modern Physics*, 34(4):667, 1962.

[65] Theodore Karman and Maurice A Biot. *Mathematical methods in engineering.* McGraw-Hill Book Company, 1940.

[66] AN Cleland and ML Roukes. Noise processes in nanomechanical resonators. *Journal of Applied Physics*, 92(5):2758–2769, 2002.

[67] K. Lulla. *Dissipation and Non linear effects in Nanomechanical resonators at low temperatures.* PhD thesis, University of Nottingham, March 2011.

[68] http://www.cm.ph.bham.ac.uk/software/kicdist/. Kic, July 2002.

[69] http://www.photomask.com/about us/executives. Toppan, 1995-2014.

[70] http://www.aimspice.com/. Aim spice, 2013.

[71] Dr.C.M.Muirhead. University of birmingham, private communication, 2014.

[72] M. Gppl, A. Fragner, M. Baur, R. Bianchetti, S. Filipp, J. M. Fink, P. J. Leek, G. Puebla, L. Steffen, and A. Wallraff. Coplanar waveguide resonators for circuit quantum electrodynamics. *Journal of Applied Physics*, 104(11):–, 2008.

[73] Dominic Christoph Walliman. Fabrication and measurement of superconducting nanowires. December 2010.

[74] J.M. Hornibrook, E.E. Mitchell, and D.J. Reilly. Suppressing dissipative paths in superconducting coplanar waveguide resonators. *Applied Superconductivity, IEEE Transactions on*, 23(3):1501604–1501604, June 2013.

[75] J Wenner, M Neeley, Radoslaw C Bialczak, M Lenander, Erik Lucero, AD OConnell, D Sank, H Wang, M Weides, AN Cleland, et al. Wirebond crosstalk and cavity modes in large chip mounts for superconducting qubits. *Superconductor Science and Technology*, 24(6):065001, 2011.

[76] M. S. Khalil, M. J. A. Stoutimore, F. C. Wellstood, and K. D. Osborn. An analysis method for asymmetric resonator transmission applied to superconducting devices. *Journal of Applied Physics*, 111(5):–, 2012.

[77] J.M. Hornibrook, E.E. Mitchell, C.J. Lewis, and D.J. Reilly. Parasitic losses in nb superconducting resonators. *Physics Procedia*, 36(0):187 – 192, 2012.

[78] Na Zhao, Jian-She Liu, Hao Li, Tie-Fu Li, and Wei Chen. Single and double superconducting coplanar waveguide resonators. *Chinese Physics Letters*, 29(8):088401, 2012.

[79] G.M. Klemencic. *Microwave and Superconducting Techniques for Measurements on Unconventional Josephson Junctions*. PhD thesis, University of Birmingham, June 2013.

[80] Daniel E. Oates and Gerald F. Dionne. Magnetically tunable superconducting resonators and filters. *IEEE Transactions on Applied Superconductivity*, 9(2):4170–4175, 1999.

[81] I.Wooldridge, C.W. Turner, and P.A. Warburton. Electrical tuning og passive hts microwave devices using single crystal strontium titanate. *IEEE Transactions on Applied Superconductivity*, 9(2):3220–3223, 1999.

[82] M J Prest, Y Wang, F Huang, and M J Lancaster. Silicon comb-drive actuators for low-temperature tuning of superconducting microwave circuits. *Journal of Micromechanics and Microengineering*, 18(12):125003, 2008.

[83] D. Bothner, T. Gaber, M. Kemmler, D. Koelle, R. Kleiner, S. Wünsch, and M. Siegel. Magnetic hysteresis effects in superconducting coplanar microwave resonators. *Phys. Rev. B*, 86:014517, Jul 2012.

[84] A. Palacios-Laloy, F. Nguyen, F. Mallet, P. Bertet, D. Vion, and D. Esteve. Tunable resonators for quantum circuits. *Journal of Low Temperature Physics*, 151(3-4):1034–1042, 2008.

[85] M. A. Castellanos-Beltran and K. W. Lehnert. Widely tunable parametric amplifier based on a superconducting quantum interference device array resonator. *Applied Physics Letters*, 91(8):–, 2007.

[86] T. Yamamoto, K. Inomata, M. Watanabe, K. Matsuba, T. Miyazaki, W. D. Oliver, Y. Nakamura, and J. S. Tsai. Flux-driven josephson parametric amplifier. *Applied Physics Letters*, 93(4):–, 2008.

[87] Z. L. Wang, Y. P. Zhong, L. J. He, H. Wang, John M. Martinis, A. N. Cleland, and Q. W. Xie. Quantum state characterization of a fast tunable superconducting resonator. *Applied Physics Letters*, 102(16):–, 2013.

[88] Daniel Bothner, Tobias Gaber, Matthias Kemmler, Dieter Koelle, Reinhold Kleiner, Stefan Wünsch, and Michael Siegel. Magnetic hysteresis effects in superconducting coplanar microwave resonators. *Physical Review B*, 86(1):014517, 2012.

[89] C Song, MP DeFeo, K Yu, and BLT Plourde. Reducing microwave loss in superconducting resonators due to trapped vortices. *Applied Physics Letters*, 95(23):232501, 2009.

[90] JM Jaycox and MB Ketchen. Planar coupling scheme for ultra low noise dc squids. *Magnetics, IEEE Transactions on*, 17(1):400–403, 1981.